數位電視廣播接收機之高速環境下同步問題之設計

學生: 王來輝　　　　　　　　　　　　指導教授: 紀翔峰 博士

國立交通大學電信工程學系碩士班

摘　　要

近年來，正交分頻多工系統(OFDM)在寬頻通訊應用上愈來愈普及。然而，相較於單載波系統，OFDM 系統對於同步問題相當敏感。由於傳送端與接收端振盪器的不完全相同，因此會有取樣頻率偏移的現象，進而導致 ICI 與 ISI 的問題。此外，若考慮無線傳輸中，接收端與傳輸端的相對速度不為零，此時會產生都卜勒效應，而使得同步的維持更為困難。本論文中，我們主要探討 OFDM 系統同步的問題，並以數位電視廣播系統(DVB-T)為討論的平台。DVB-T 同步問題的解決方法，已在很多文獻中提出過。然而，大部份都是針對無相對速度或低相對速度下的同步的解決方法。在本篇論文中，為了克服在高速移動下，都卜勒效應所帶來的問題，我們提出了一個新的同步問題的解決方法。之後，我們也將藉由電腦模擬，證明我們提出的方法在高速移動下，仍有很好的效能。

The Design of Synchronization Algorithms for High-mobility Digital Video Broadcast Receivers

Student: Lai-Huei Wang   Advisor: Dr. Hsiang-Feng Chi

Department of Communication Engineering
National Chiao Tung University

ABSTRACT

In recent years, OFDM becomes popular for broadband communications. However, compared to single carrier systems, OFDM system is very sensitive to the synchronization problem. The mismatch of crystal oscillators between the transmitter and the receiver circuitry causes the sampling clock frequency offset and will introduce ICI and ISI. Furthermore, if the mobile wireless transmission is considered, the synchronization maintenance will become more difficult because of the Doppler effect. The main topic of this thesis is to discuss the synchronization problems of OFDM systems. DVB-T is selected as the system platform for discuss here. Many synchronization algorithms had been proposed and are applied successfully in DVB-T demodulators. However, most of them can operate properly for stationary wireless and low-mobility receiving. To combat the severe Doppler effect in high-mobility environment, effective synchronization algorithms are necessary. Therefore, the synchronization algorithm in high-mobility environment is mainly concerned in this thesis. We propose an innovative synchronization algorithm, which is shown almost not to be affected by the effect caused by high mobility.

Contents

List of Figures

x

List of Tables

Chapter 1
Introduction

In recent years, orthogonal frequency division multiplexing (OFDM) becomes popular for broadband communications. OFDM originates from multicarrier modulation (MCM), which is the technique of transmitting data by dividing them into several data streams and modulating each of these data streams onto individual subcarriers. Different from the traditional MCM, OFDM allows the spectra of the subcarriers to be overlapped as long as they are mutually orthogonal. With this characteristic, the use of bandwidth in OFDM is more efficient than that in the traditional MCM.

Although OFDM is proposed in the mid 60s [1], it is not popular due to the enormous hardware complexity at that time. Until 1971, Weinstein and Ebert [2] proposed the idea of using the discrete Fourier Transform (DFT) and inverse discrete Fourier Transform (IDFT) to perform baseband modulation and demodulation. Thereafter, OFDM had been paid much attention again. In the modern OFDM systems, the efficient Fast Fourier Transform (FFT) and Inverse Fast Fourier Transform are utilized to perform modulation and demodulation.

In 1980, Peled and Ruiz [3] suggest the ways of using Cyclic Prefix (CP) to solve the problem of Inter Symbol Interference (ISI) caused by multipath channels. Nowadays, OFDM is used in many standards. In wire-line transmission systems,

OFDM is adopted in Asymmetric Digital Subscriber Loop (ADSL) and Very High Bit-rate Digital Subscriber Loop (VDSL). In wireless transmission systems, OFDM is used in Digital Audio Broadcasting (DAB) [4], Digital Video Broadcasting (DVB) [5], IEEE 802.11a [6], and 802.16a [7].

- **Research Motivation**

Compared to single carrier systems, OFDM system is very sensitive to the synchronization problem [8]. At the OFDM transmitter, a block of signals are modulated by the use of IDFT to form an OFDM symbol. At the receiver, the symbol boundary should be determined to ensure that the correct OFDM symbol is demodulated by IDFT.   Otherwise, it leads to a symbol synchronization problem. In addition, the mismatch of crystal oscillators between the transmitter and the receiver circuitry causes the sampling clock frequency offset. Having the above synchronization problems, the OFDM system will introduce Inter Carrier Interference (ICI) and ISI. Without properly solving these problems, the system performance will decay significantly. Furthermore, if the mobile wireless transmission is considered, the synchronization maintenance will become more difficult than fixed wireless transmission because of the Doppler effect.

The main topic of this thesis is to discuss the synchronization problems of OFDM systems. DVB-T is selected as the system platform for discuss in the thesis. Many clock and carrier synchronization algorithms had been proposed and are applied successfully in DVB-T demodulators. However, most of them can operate properly for stationary wireless and low-mobility receiving. To combat the severe Doppler effect in high-mobility environment, effective synchronization algorithms are necessary. Therefore, the synchronization algorithm in high-mobility environment is

mainly concerned in this thesis. We propose an innovative synchronization algorithm, which is shown almost not to be affected by the effect caused by high mobility.

● **Organization of this thesis**

The thesis is organized as follows:

Chapter 1, "Introduction", introduces the origin of OFDM, the applications using OFDM presently and the organization of this thesis.

Chapter 2, "Introduction to OFDM", introduces the modulation theory of OFDM.

Chapter 3, "Signal and Channel Model", states the models of OFDM signal, the signal with synchronization problem, and channel.

Chapter 4, "DVB-T Receiver", provides the overview of DVB-T specification overview and the architecture of DVB-T receiver.

Chapter 5, "Sampling Clock Synchronization", discusses how to estimate the sampling clock error and recovery the correct sampling clock.

Chapter 6, "Other Components of Inner Receiver", is dedicated to the algorithms of symbol synchronization, carrier frequency synchronization, and channel estimation.

Chapter 7, "Inner Receiver Evaluation", presents a processing flow and an performance analysis of inner receiver.

Chapter 8, "Conclusion and Future Work", gives a conclusion and the work that is still needed to be discussed.

Chapter 2
OFDM and DVB-T Overview

In this chapter, we present an introduction of OFDM theory. First, we state the principle of OFDM transmission and the block diagram of an OFDM system. Then, we introduce the cyclic property of guard interval in an OFDM symbol. After that, in this chapter, we also give an overview of a DVB-T system which adopts the OFDM transmission. We will make a description of DVB-T standard, including the system block diagram, frame structure, and reference data. Then, we will show the digital receiver structure for DVB-T system and explain the work that needs be handled in a DVB-T digital receiver.

2.1 OFDM Overview

2.1.1　Principle of OFDM Transmission

OFDM originates form multicarrier modulation (MCM) which is a technique of transmitting data by dividing the stream into several lower bit streams and by using these streams to modulate several subcarriers. The transmit duration of every subcarrier is several times to original data and the symbol duration of every subcarrier

increases which results in robustness to ISI introduced by multipath delay spread.

The difference between OFDM and traditional MCM is overlapping of subcarriers. In traditional MCM, there is no overlapping in the subcarrier spectra. In OFDM, on the contrary, every overlapping subcarrier is orthogonal to each other so there is no interference between subcarriers. With the property of orthogonality, OFDM system has better bandwidth efficiency than traditional MCM [9] as showed in Figure 2-1.

(b) Traditional MCM

(a) OFDM
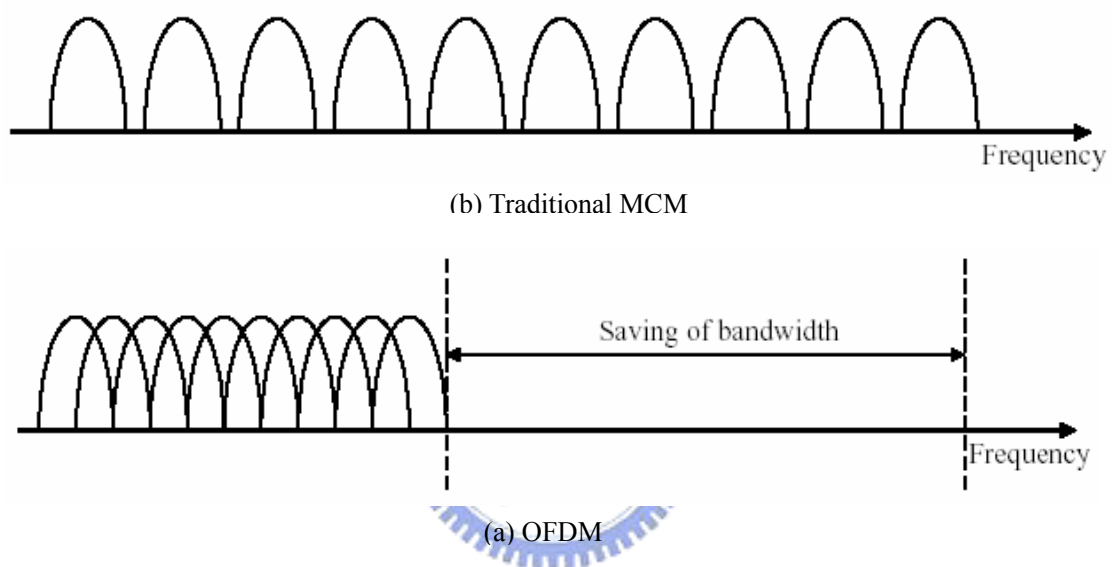
Figure 2-1 bandwidth diagrams for multicarrier modulation

In OFDM system, the input QAM (Quadrature-Amplitude Modulation) or PSK (Phase-Shift Keying) series data is rearranged into a parallel data sequence and modulated by subcarriers. OFDM signal is then obtained by summation of data modulated by all subcarriers. The analog modulator block diagram is modeled in Figure 2-2.
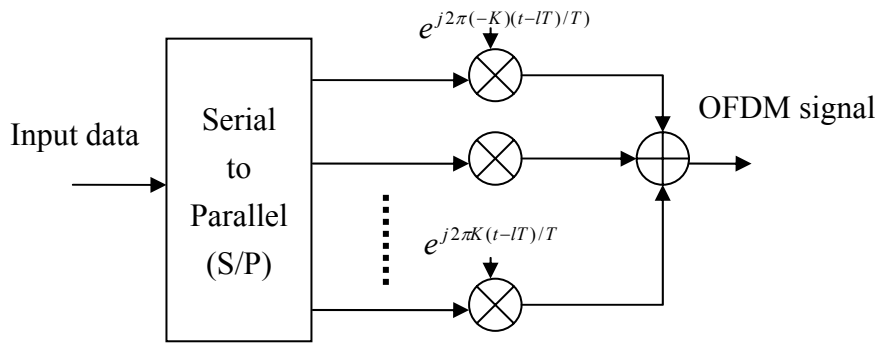
Figure 2-2 OFDM analog modulator

The lth OFDM complex baseband signal can be written as :

$$s_l(t) = \begin{cases} \sum_{k=0}^{N-1} X_{l,k} e^{j2\pi k(t-lT)/T}, & t_l < t < t_l + T \\ 0, & otherwise \end{cases} \quad (2.1)$$

where   N: subcarrier number

X$_{l,k}$: kth subcarrier symbol of lth OFDM symbol

T: OFDM symbol duration

t$_l$: lth OFDM symbol start time

Figure 2-3 shows the spectra of OFDM signal and we can see that at the peak value of each subcarrier, the contribution of other subcarriers are zero so that there is no interference for subcarriers to each other.
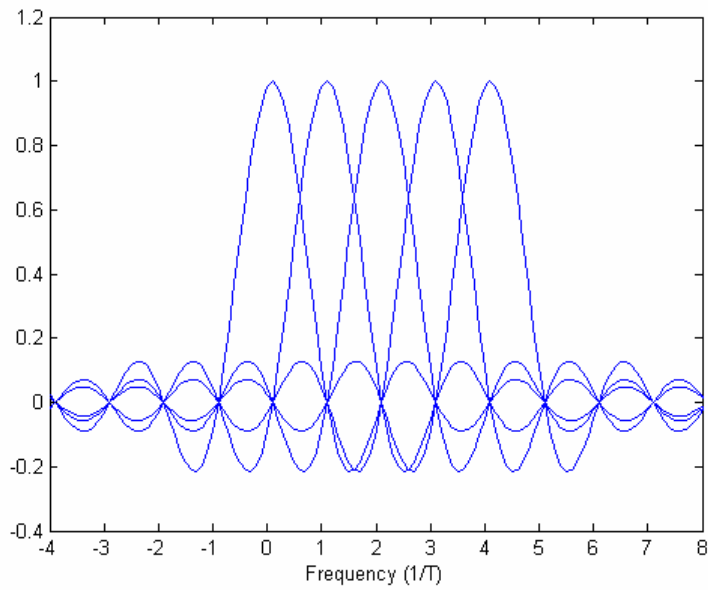
Figure 2-3 OFDM signal spectra

To sample the lth OFDM signal at $t = t_l + n \cdot T_s$, where $T_s = T/N$ is sampling period, we get digital samples as:

$$s_l(n) = \sum_{k=0}^{N-1} X_{l,k} e^{\frac{j2\pi kn}{N}}, \quad n = 0,1,...,N-1 \qquad (2.2)$$

we can find that the result of modulator happens to be the result of IDFT operation. Because the analog modulator needs too many oscillators to realize, currently we use digital IFFT to replace the analog modulation. As a result, a digital modulator is formed by using IDFT as shown by Figure 2-4.
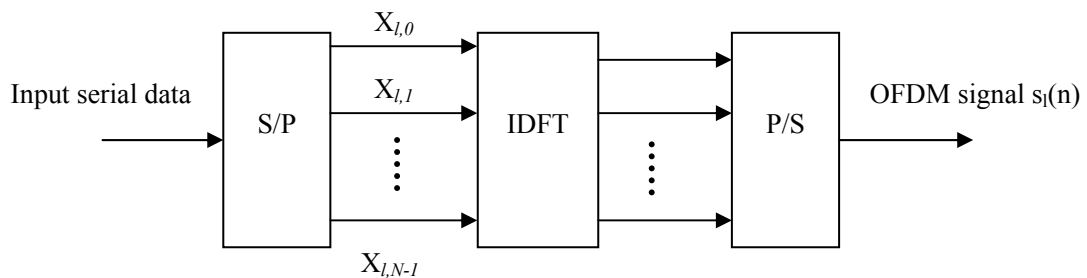
Figure 2-4 an OFDM digital modulator

At receiver, analog demodulation is done by multiplying the received lth OFDM signal by $exp(j2\pi k(t-lT)/T)$ and integration with one OFDM symbol duration. Figure 2-5 models the analog demodulator.

$$e^{j2\pi(-K)(t-lT)/T}$$

$$e^{j2\pi K(t-lT)/T}$$
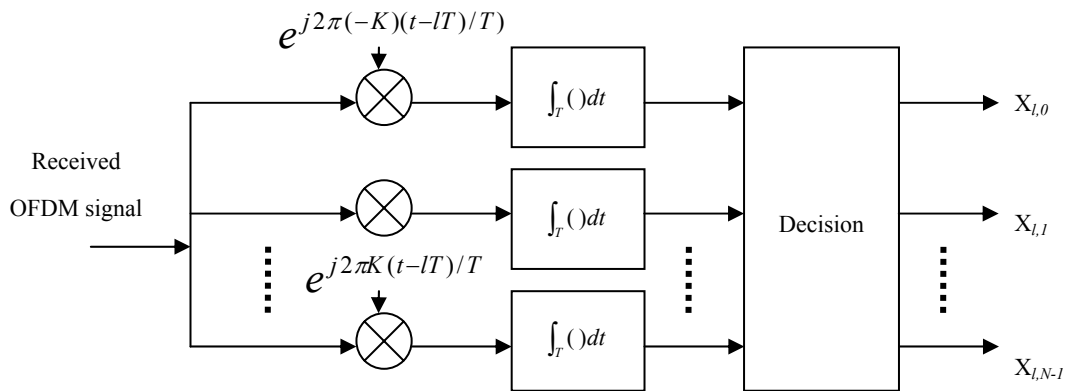
Figure 2-5 an OFDM analog demodulator

For implement, however, demodulator is also difficult to realize as the same with modulator. At present, digital demodulator using DFT is used to replace analog demodulator. Figure 2-6 shows the block diagram of digital demodulator.
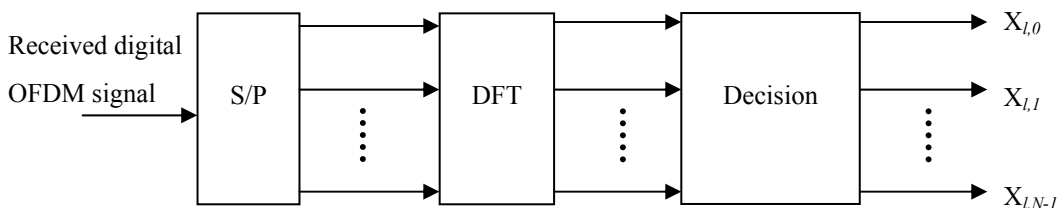
Figure 2-6 an OFDM digital demodulator

2.1.2 Guard Time and Cyclic Prefix (CP)

For a broadband wireless system, ISI which results from multipath propagation is one main constrain to performance. In traditional system, general method for ISI

problem is to use an equalizer in time domain but the equalizer needs very complexity implement. Nowadays, OFDM is a popular solution for it. However, there is still ISI in the head of an OFDM symbol. The concept of ISI in OFDM symbols is illustrated in Figure 2-7 (a). In order to eliminate ISI, an additional time interval named guard time is introduced to every OFDM symbol as shown in Figure 2-7 (b).
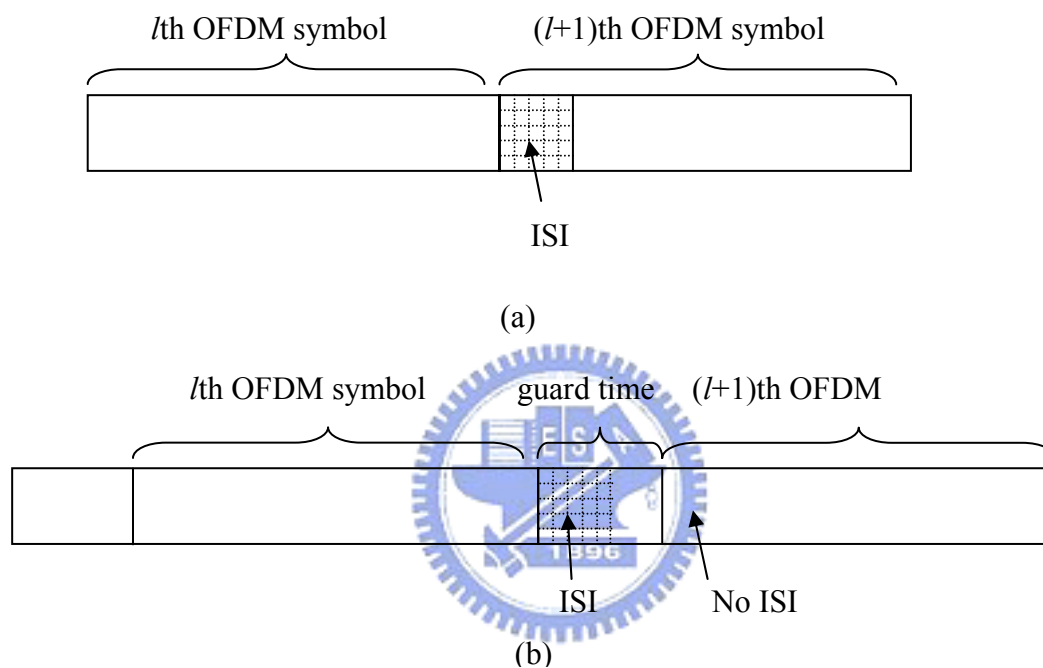
Figure 2-7 ISI problem in OFDM (a) without guard time (b) with guard time

We choose guard time length larger than channel delay spread so that the OFDM symbol is not interfered by the adjacent symbol. However, if there is no signal in guard time, intercarrier interference (ICI) will be caused because the orthogonality is lost. Figure 2-8 illustrates this problem. In this case, the subcarrier 1 and delayed subcarrier 2 are not orthogonal anymore because of the blank guard time so that ICI is introduced.
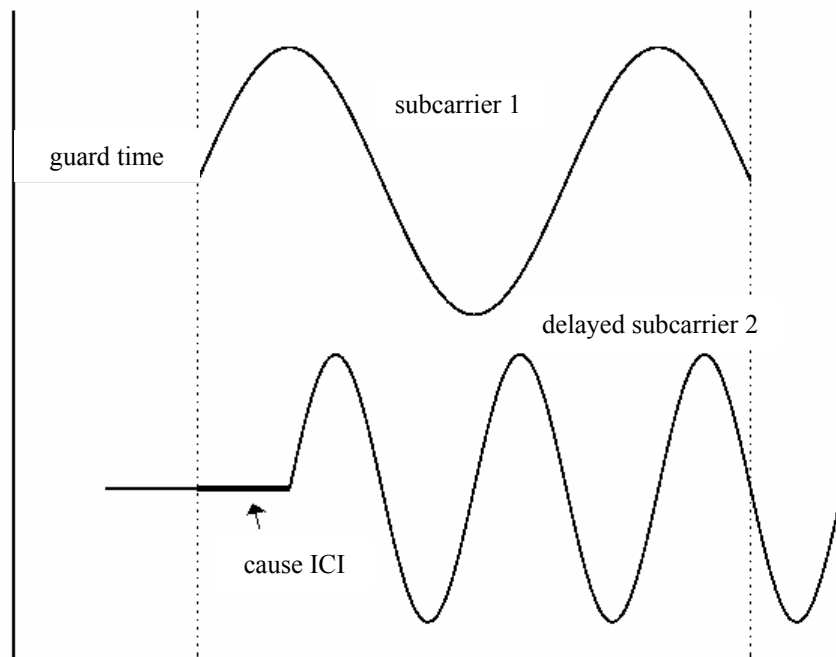
Figure 2-8 ICI problem caused by a blank guard time

To solve this problem, rather than using a blank guard time, cyclic extension is chosen. The OFDM symbol is cyclically extended in the guard time as showed in Figure 2-9. consequently, guard interval is also called CP (Cyclic Prefix). With the addition of CP, ICI problem in Figure 2-8 is removed. The orthogonality of signal is maintained as Figure 2-10 displays

.
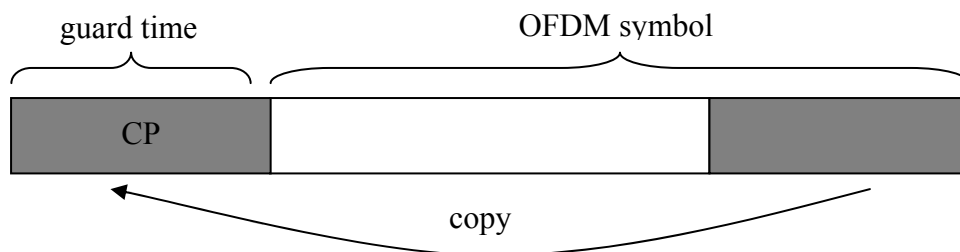
Figure 2-9 cyclic extension in guard time

subcarrier 1

delayed subcarrier 2

no ICI
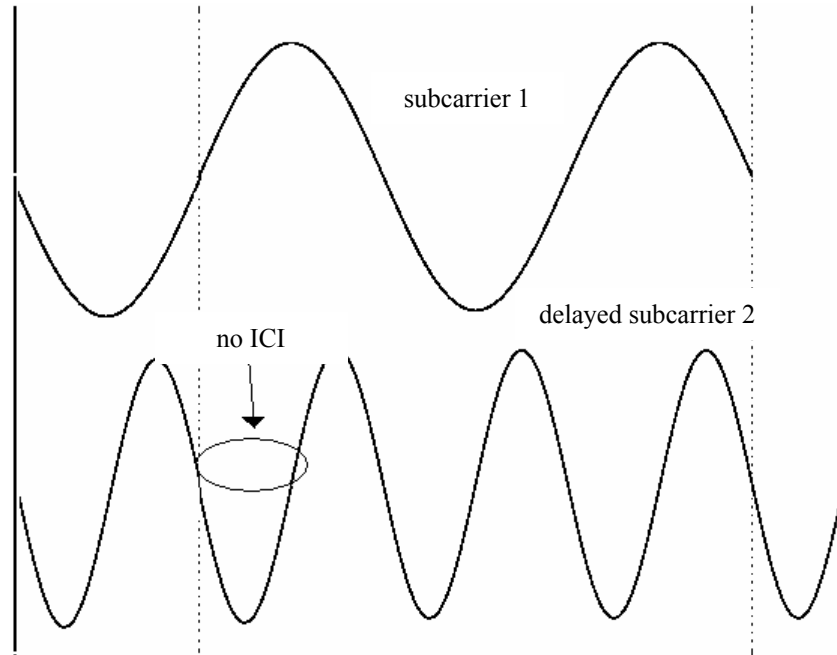
Figure 2-10 ICI elimination by cyclic extension in guard time

2.2 DVB-T Overview

DVB-T is a digital video broadcasting standard based on COFDM (Coded OFDM) and it is set up by the European DVB consortium in 1996. The main competitors are ATSC (Advanced Television Systems Committee) adopted by U.S. and Canada and ISDB (Integrated Services Digital Broadcasting) introduced by Japan. DVB-T standard, however, adopts by most countries including Taiwan.

In this thesis, our simulation is handled on a DVB-T system hence we first introduce the DVB-T system and give an overview of inner receiver in the following sections.

2.2.1   System Overview

In DVB-T, the following processes shall be applied to the data stream:

- Transport multiplex adaptation and randomization for energy dispersal;

- Outer coding (i.e. Reed-Solomon code);

- Outer interleaving (i.e. convolutional interleaving);

- Inner coding (i.e. punctured convolutional code);

- Inner interleaving;

- Mapping and modulation;

- OFDM transmission

Figure 2-11 shows the system block diagram of DVB-T [5]. After source coding and transport multiplexing, original video, audio and data streams are translated to packets. For each packet, it has length of 188 bytes which contain one sync-word byte (47_{HEX}) and 187 data bytes. Every eight packets form a group and the parts of data are multiplied by a Pseudo Random Binary Sequence (PRBS) which is reset for each group. To prevent the condition of serious zeros or ones, the sync-word byte of first packet of each group is translated from 47_{HEX} to $B8_{HEX}$. The operation is called MUX Adaptation, Energy Dispersal.
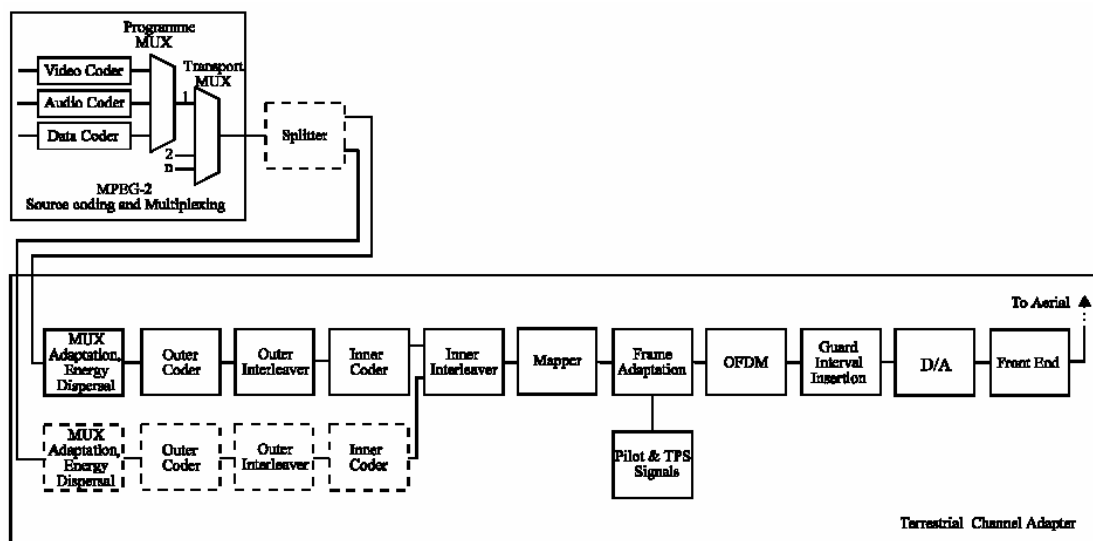
Figure 2-11 DVB-T system block diagram

When transmitting data with priority, Hierarchical Transmission is used. First, use a splitter to separate the data streams into high priority and low priority part. These two parts of data can have individual channel coding and modulation level. We can demodulate the high priority by the receiver's quadrant in constellation and then demodulate the low priority by the position of the signal in constellation. For example, Figure 2-12 (a) and (b) [5] shows hierarchical 16-QAM mappings with α= 1 and α= 2 respectively, where α is the minimum distance separating two constellation points, $y_{0,q'}$ and $y_{1,q'}$ are bits with high priority, and $y_{2,q'}$ and $y_{3,q'}$ are bits with low priority. From the figure we can see that high priority data is more error-free with larger α because the distance between zero and data point is larger and α can have three values 1, 2 and 4.
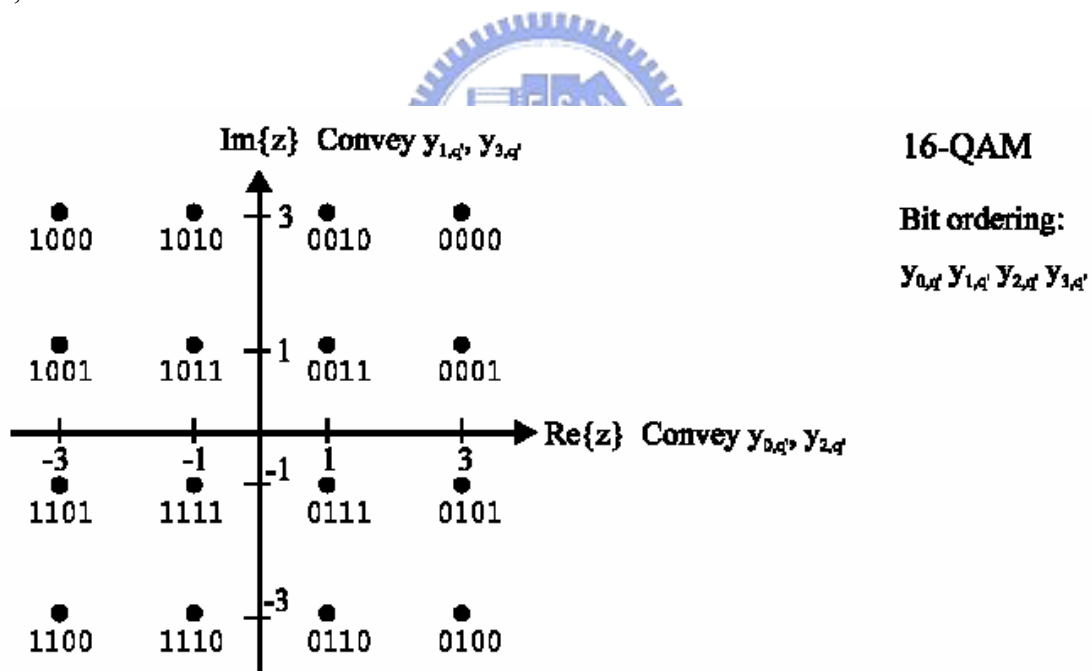
Figure 2-12 (a) hierarchical 16-QAM mappings with $\alpha = 1$
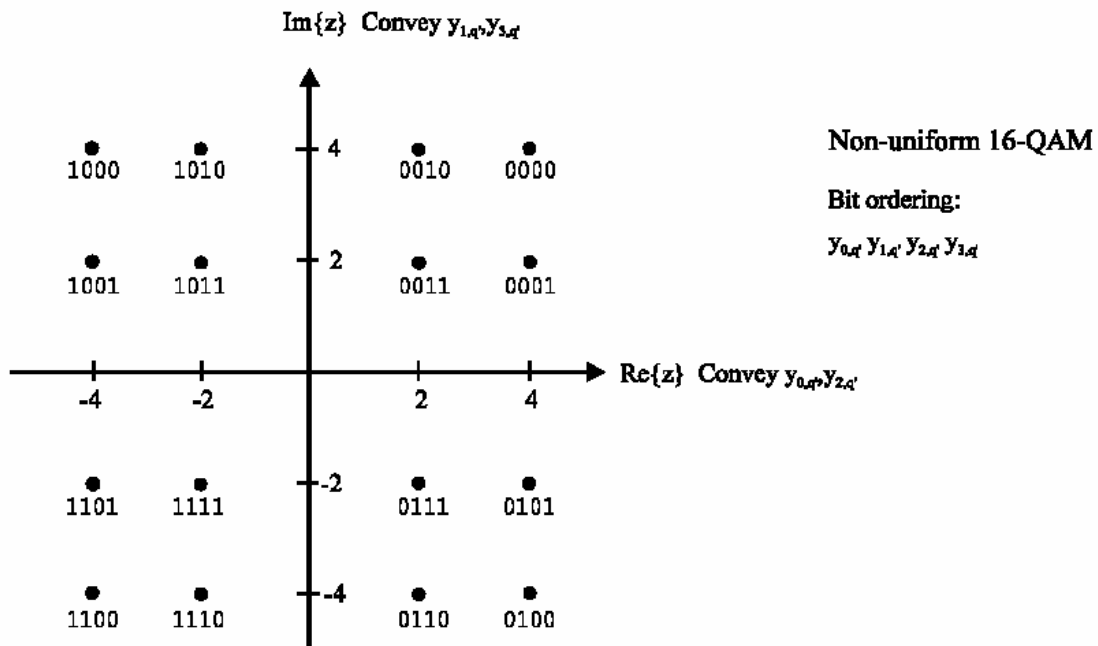
Figure 2-12 (b) hierarchical 16-QAM mappings with $\alpha = 2$

After channel coding and interleaving, all data carriers are modulated using either QPSK, 16-QAM, 64-QAM, non-uniform 16-QAM or non-uniform 64-QAM constellations where "non-uniform" means α is not equal to one.

Except for subcarriers carrying data, there are some subcarriers which carry reference signal known by receivers and we will introduce them later. After reference data adaptation, the signal is handled by IFFT. There are two transmission modes in DVB-T: 2K mode and 8K mode. 2048-point IFFT and 8192-point IFFT will be used in the 2K mode and 8K mode respectively.

2.2.2 Signal Expression and Frame Structure

The transmitted signal is organized in frames. Each frame consists of 68 OFDM symbols and four frames constitute one super-frame. Each symbol is constituted by a set of K = 6817 and K = 1705 carriers in the 8K and 2K mode respectively. The

carriers are indexed by $k \in [K_{\min}, K_{\max}]$ and determined by $[K_{min}; K_{max}] = [0;1704]$ in 2K mode and [0;6816] in 8K mode.

The emitted signal is described by the following expression:

$$s(t) = \text{Re}\{e^{j2\pi f_c t} \sum_{m=0}^{\infty} \sum_{l=0}^{67} \sum_{k=K_{\min}}^{K_{\max}} X_{m,l,k} \times g_{m,l,k}(t)\} \qquad (2.3)$$

where

$$g_{m,l,k}(t) = \begin{cases} e^{j2\pi \frac{k'}{T_u}(t-T_g-lT_{sym}-68mT_{sym})}, & (l+68m)T_{sym} \leq t \leq (l+68m+1)T_{sym} \\ 0, & otherwise \end{cases} \qquad (2.4)$$

and k denotes the carrier number, l denotes the OFDM symbol number, m denotes the transmission frame number, T_{sym} is the symbol duration, $1/T_u$ is the carrier spacing, T_g is the duration of the guard interval, f_c is the central frequency of the RF signal, $k' = k-(K_{max}+K_{min})/2$ is the carrier index relative to the centre frequency and $X_{m,l,k}$ is complex symbol for carrier k of the data symbol no.l in frame number m.

The system is supposed to use the traditional analog broadcasting UHF (Ultra High Frequency) band with 8MHz bandwidth. The central frequency of the transmitter carrier is:

$$470MHz + 4MHz + n \times 8MHz, \qquad n = 0,1,2,3,... \qquad (2.5)$$

For countries with 7MHz or 6MHz channel bandwidth, it needs only to change the sampling period to satisfy the regulated bandwidth. The sampling period T_s is 7/64 μs for a 8MHz channel, 1/8 μs for a 7MHz channel and 7/48 μs for a 6MHz channel.

Table 2-1 lists numerical values for the OFDM parameters in the 8K and 2K modes for 8MHz channels. There is four different lengths of guard interval: $T_g/T_u = 1/4, 1/8, 1/16, 1/32$ for us to choose one of them to meet the need of the system.

Parameter	8K mode	2K mode
Number of carriers K	6817	1705
Value of carrier number K_{min}	0	0
Value of carrier number K_{max}	6816	1704
Duration T_u	896 μ s	224 μ s
Carrier spacing $\Delta f = 1/T_u$	1116 Hz	4464 Hz
Spacing between carriers K_{min} and K_{max} (K-1) / T_u	7.61 MHz	7.61 MHz
T_g / T_u	¼,1/8,1/16,1/32	¼,1/8,1/16,1/32

Table 2-1 OFDM parameter in DVB-T

2.2.3　Reference Signals

The reference signals are with symbols which are known. The main functions of them are synchronization, channel estimation and signaling. There are three kind of reference signals in DVB-T : scattered pilots, continual pilots, and TPS (Transmission Parameter Signaling) and they are all transmitted with a boosted power level. The continual and scattered pilots are modulated according to a PRBS (Pseudo Random Binary Sequence) sequence, $W_k = X^{11} + X^2 + 1$.

1.　Scattered pilot

The scattered pilots are located at scattered subcarrier indices in every symbol. For the *l*th OFDM symbol, the locations of the scattered pilots are

$$\{k = K_{min} + 3(l \mod 4) + 12p \mid p : \text{integer}, p \geq 0, k \in [K_{min}, K_{max}]\} \qquad (2.6)$$

and the corresponding scattered pilots have the values as

$$X_{m,l,k} = \frac{4}{3} \cdot (1 - 2W_k) \qquad (2.7)$$

W_k is produced by PRBS and has the value of 0 or 1 so that the values of scattered pilots are +4/3 or -4/3. At the beginning of each OFDM symbol, the PRBS is initialized so W_k has no relation to the index of OFDM symbols. It leads to that pilots have the same value as long as they are at the same carrier index.

Figure 2-13 shows the location of scattered pilots. There is a repeat for the locations of scattered pilots every four OFDM symbols thus we say the scattered pilots have a period in time direction $P_t = 4$. In frequency direction, there is one scattered pilot every 12 subcarriers so that the period is $P_f = 12$.
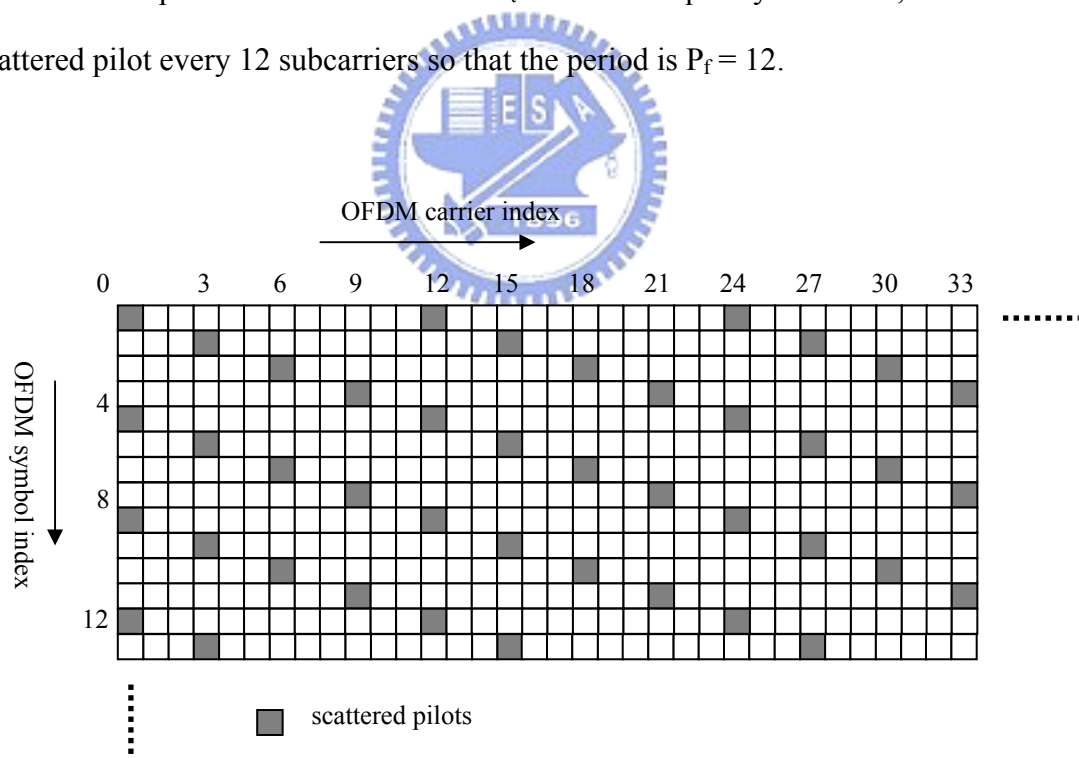
Figure 2-13 the location diagram of scattered pilots

2.   Continual pilot

In addition to the scattered pilots, there are 177 continual pilots in the 8K mode

and 45 in the 2K mode inserted into fixed subcarriers in every OFDM symbol shown in Figure 2-14. The values of the continual pilots with subcarrier index k are produced in the same way with scattered pilots.
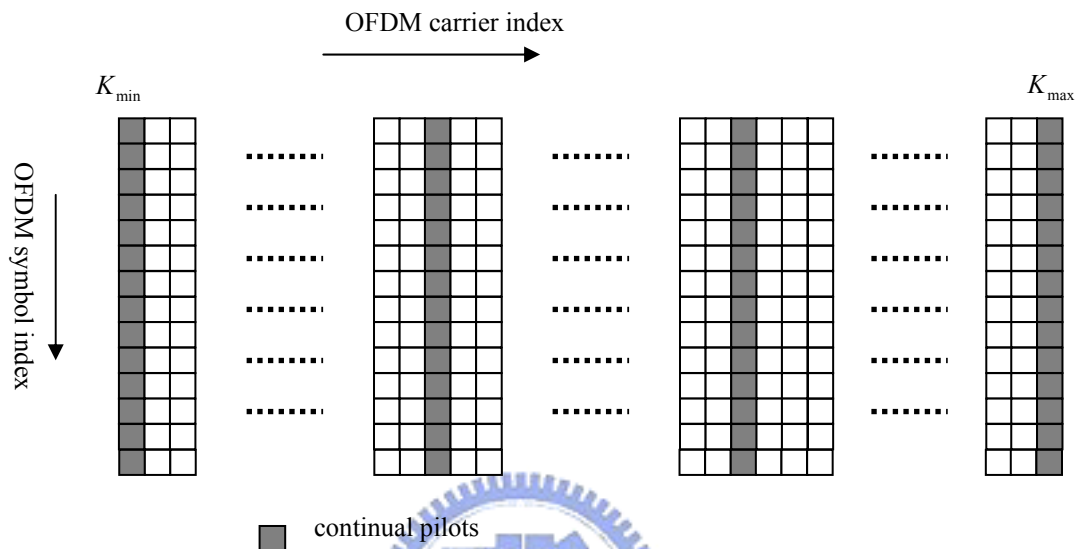
Figure 2-14 the location diagram of continual pilots

3. Transmission Parameter Signaling (TPS)

The TPS carriers are used for the purpose of signaling parameters related to the transmission scheme, coding and modulation. The TPS is transmitted in parallel on 17 TPS carriers for the 2K mode and on 68 carriers for the 8K mode. Every TPS carrier in the same symbol conveys the same differentially encoded information bit.

The TPS carriers convey information on:

- Modulation including the α value of the QAM constellation pattern;
- Hierarchy information;
- Guard interval mode
- Inner code rates;

- Transmission mode;

- Frame number in a super-frame;

- Cell identification.

2.2.4 Receiver Structure

Figure 2-15 shows the basic structure of a DVB-T receiver. In the inner receiver, there are several jobs needed to be complete. First, we must estimate the correct OFDM symbol window for FFT operation so that the post-FFT processes can be handled with correct OFDM data samples. Second, the carrier frequency and sampling clock error are needed to be synchronized. Without the carrier and clock synchronization, serious interference will result from carrier frequency offsets and clock offset. The interference will damage the system performance evidently. Next, before decision, we must estimate the response of the channel in order to equalize the effect caused by the channel and non-ideal synchronization. The equalizer is simply a one-tap filter in frequency domain because of the advantage of robust to channel dispersion in an OFDM system accomplished by inserting guard intervals. After inner receiver, the processed data is delivered to outer receiver for channel decoding procedure. In the following chapters, we will present the sampling clock synchronization schemes in chapter 4 and symbol synchronization, frequency synchronization, and channel estimation in chapter 5. After that, we consider the combined effects of the overall inner receiver and evaluate the system performance by the use of computer simulation in chapter 6.
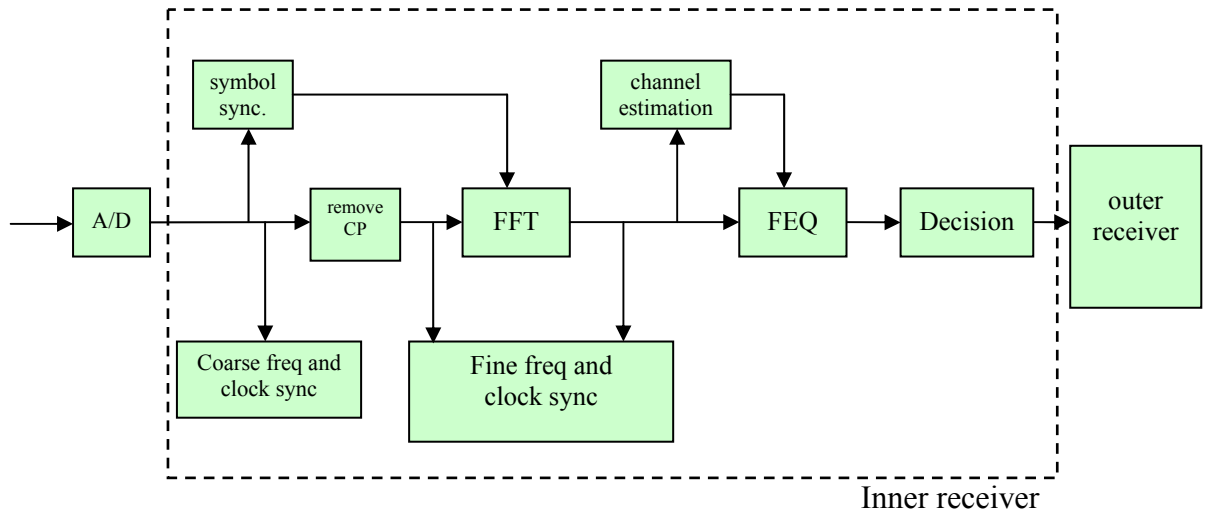
Figure 2-15 DVB-T receiver block diagram

Chapter 3
Signal and Channel Model

In this chapter, mathematical form of OFDM signal is present and the effect of non-ideal synchronization is also discussed. Moreover, the channel in a wireless environment is also stated here.

3.1 OFDM Signal Model

In this section, we first define parameters for an OFDM system:

subcarrier number: N   OFDM symbol duration: T_u

OFDM CP duration: T_g total OFDM symbol duration: $T_{sym} = T_u + T_g$

OFDM sampling period: $T_s = T_u/N$

Sampling points number of CP: $N_g = T_g/T_s$

Sampling points number of total OFDM symbol: $N_s = T_{sym}/T_s$

Figure 3-1 illustrates the OFDM transmittor and receiver baseband block diagram. At transmittor, input QAM or PSK data is modulated by IFFT and then add CP to avoid ISI problem. Next, convert digital data to analog one by DAC and then pass into the transmit filter to limit the spectrum in the allowed range. After that, outputs are

OFDM baseband signals. At receiver, the received baseband signals pass into receiver filter and are converted from analog to digital by ADC. Then, remove the guard interval and demodulate by FFT.
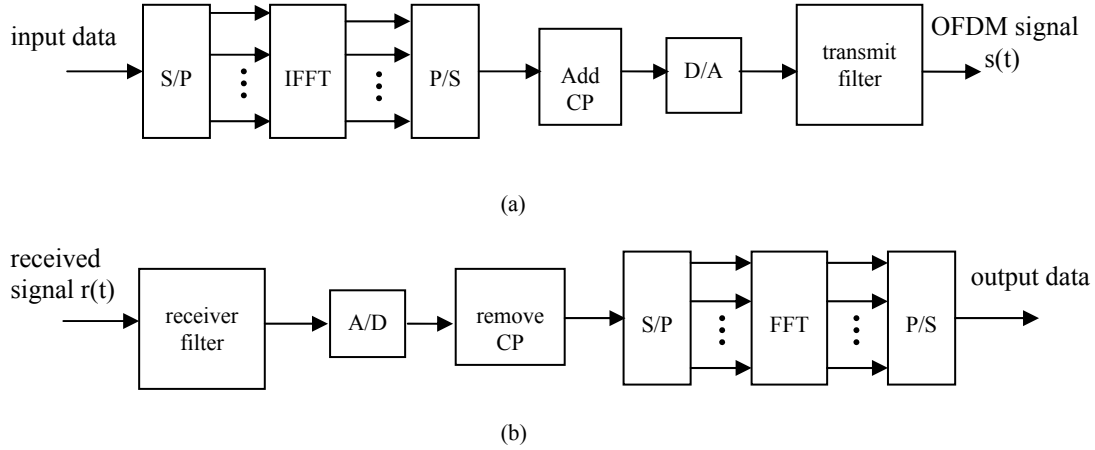
Figure 3-1 baseband OFDM system block diagram (a) transmittor (b) receiver

The transmitted baseband signal can be described by

$$s(t) = \frac{1}{\sqrt{T_u}} \sum_{l=0}^{\infty} (\sum_{k=0}^{N-1} X_{l,k} e^{\frac{j2\pi k(t-T_g-lT_{sym})}{T_u}}) \cdot u(t-l_{T_{sym}}) * g_T(\tau) \qquad (3.1)$$

where * denotes convolution, l is OFDM symbol index, k is OFDM subcarrier index, l_{Tsym} is lth OFDM symbol start time, $g_T(\tau)$ is transmit filter impulse response and $u(t)$ is a window function defined as :

$$u(t) = \begin{cases} 1, & 0 \le t < T_{sym} \\ 0, & otherwise \end{cases} \qquad (3.2)$$

The signal is transmitted over a frequency selective fading channel which is with impulse response:

$$h(\tau,t) = \sum_i h_i(t) \cdot \delta(\tau - \tau_i) \qquad (3.3)$$

and we combine the effect of transmit filter $g_T(\tau)$ and receiver filter $g_R(\tau)$ into the channel :

$$c(\tau,t) = h(\tau,t) * g_T(\tau) * g_R(\tau) = \sum_i c_i(t) * \delta(\tau - \tau_i) \qquad (3.4)$$

After passing through the channel, the received signal is

$$r(t) = \sum_i c_i(t) \cdot s(t - \tau_i) + n(t) \qquad (3.5)$$

where n(t) is Additional White Gaussian Noise (AWGN).

Sampling the signal at time instants $t_n = nT_s$ yields

$$r(t_n) = \sum_i c_i(nT_s) \cdot s(nT_s - \tau_i) + n(nT_s) \qquad (3.6)$$

After removing CP, the N samples of lth OFDM symbol are sampled at time instants

$$t_{l,n} = (n + N_g + l \cdot N_s) \cdot T_s, \qquad n = 0,1,...N-1 \qquad (3.7)$$

Accordingly, the N samples of lth OFDM symbol are

$$
\begin{aligned}
r_{l,n} &= r((n + N_g + l \cdot N_s) \cdot T_s), \qquad n = 0,1,...N-1 \\
&= \sum_i c_i((n + N_g + l \cdot N_s) \cdot T_s) \cdot s((n + N_g + l \cdot N_s) \cdot T_s - \tau_i) + n_{l,n} \\
&= \sum_i c_i((n + N_g + l \cdot N_s) \cdot T_s) \cdot \frac{1}{\sqrt{T_u}} \sum_{k=0}^{N-1} X_{l,k} e^{j2\pi k(nT_s - \tau_i)/T_u} + n_{l,n} \\
&= \frac{1}{\sqrt{T_u}} \sum_{k=0}^{N-1} X_{l,k} e^{j2\pi kn/N} \sum_i c_i((n + N_g + l \cdot N_s) \cdot T_s) e^{-j2\pi k\tau_i/T_u} + n_{l,n} \qquad (3.8)
\end{aligned}
$$

Here we assume that the channel is the same within one OFDM symbol and denoted by $c_i(l)$ so that equation (3.8) becomes :

$$r_{l,n} = \frac{1}{\sqrt{T_u}} \sum_{k=0}^{N-1} X_{l,k} e^{j2\pi kn/N} \sum_i c_i(l) e^{-j2\pi k\tau_i/T_u} + n_{l,n}$$

$$= \frac{1}{\sqrt{T_u}} \sum_{k=0}^{N-1} X_{l,k} e^{j2\pi kn/N} C_{l,k} + n_{l,n}, \qquad n = 0,1,...,N-1 \qquad (3.9)$$

where

$$C_{l,k} = \sum_i c_i(l) e^{-j2\pi k\tau_i/T_u} \qquad (3.10)$$

From equation (3.10), it is given that $C_{l,k}$ is channel frequency response at subcarrier frequency $f_k = k/T_u = k \cdot \Delta f$, where Δf is the subcarrier spacing.

After that, the N samples of lth OFDM symbol are parallel to FFT for demodulation and the demodulated data symbols are

$$R_{l,k} = \sum_{n=0}^{N-1} r_{l,n} \cdot e^{-j2\pi kn/N}, \qquad k = 0,1,...,N-1$$

$$= \frac{1}{N} \sum_{n=0}^{N-1} (\sum_{k'=0}^{N-1} X_{l,k'} C_{l,k'} \cdot e^{j2\pi k'n/N} + n_{l,k}) \cdot e^{-j2\pi kn/N}$$

$$= \frac{1}{N} \sum_{k'=0}^{N-1} X_{l,k'} C_{l,k'} \sum_{n=0}^{N-1} e^{j2\pi(k'-k)n/N} + N_{l,k}$$

$$= X_{l,k} C_{l,k} + N_{l,k} \qquad (3.11)$$

As a result, the received symbol at kth subcarrier is the effect of multiplying the channel response at kth subcarrier frequency to the transmitted symbol and interference by channel noise. For this reason, we can simply use a single-tap filter to equalize the channel effect in frequency domain at receiver.

3.2 Effect of Non-ideal Synchronization

Because of the difference between the carrier frequency of the transmittor oscillator $f_{c,tx}$ and the frequency of the receiver oscillator $f_{c,rx}$, there is a frequency

error named carrier frequency offset Δf_c :

$$\Delta f_c = f_{c,rx} - f_{c,tx} \qquad (3.12)$$

After carrier frequency down to baseband, the signal leave the effect due to carrier frequency offset, thus equation (3.4) and (3.5) must be modified to

$$c(\tau,t) = h(\tau,t) * g_T(\tau) * \hat{g}_R(\tau), \quad where \ \hat{g}_R(\tau) = g_R(\tau) \cdot e^{j2\pi\Delta f_c t} \qquad (3.13)$$

$$r(t) = \sum_i c_i(t) \cdot s(t - \tau_i) \cdot e^{j2\pi\Delta f_c t} + n(t) \qquad (3.14)$$

In addition, there is also a mismatch between the sampling frequency at receiver (T_s') and that of transmittor (T_s), which is called sampling clock offset. Here, for the sake of convenience, we define a normalized sampling clock offset as

$$t_\Delta = \frac{T_s' - T_s}{T_s} \qquad (3.15)$$

and then the sampling time instants of the N samples of lth OFDM symbol are changes to:

$$t_{l,n} = (n + N_g + l \cdot N_s) \cdot T_s', \qquad n = 0,1,...N-1 \qquad (3.16)$$

$$
\begin{aligned}
r_{l,n} &= r((n + N_g + l \cdot N_s) \cdot T_s'), \qquad n = 0,1,...N-1 \\
&= \sum_i c_i((n + N_g + l \cdot N_s) \cdot T_s') \cdot s((n + N_g + l \cdot N_s) \cdot T_s' - \tau_i) \\
&\quad \cdot e^{j2\pi\Delta f_c((n+N_g+l\cdot N_s)\cdot T_s')} + n_{l,n} \qquad\qquad (3.17)
\end{aligned}
$$

Provided that symbol synchronization is completed (i.e. OFDM symbol boundary is found without error), the data symbol after FFT becomes:

$$R_{l,k} = \sum_{n=0}^{N-1} r_{l,n} \cdot e^{-j2\pi kn/N}, \qquad k = 0,1,...,N-1$$

$$= (e^{j\pi\phi_k} \cdot e^{j2\pi\frac{lN_s + N_g}{N}\phi_k}) \cdot \sin c(\phi_k) X_{l,k} C_{l,k} +$$

$$\underbrace{\sum_{i;i\neq k}(e^{j\pi\phi_{i,k}} \cdot e^{j2\pi\frac{lN_s + N_g}{N}\phi_i}) \cdot \sin c(\phi_{i,k}) X_{l,i} C_{l,i} + n_{l,k}}_{ICI} \qquad (3.18)$$

where

$$\phi_{i,k} = (1+t_\Delta)(\Delta f_c T_u + i) - k \qquad (3.19)$$

$$\phi_k = \phi_{k,k} \approx \Delta f_c T_u + t_\Delta \cdot k \qquad (3.20)$$

Here we model the ICI as additional noise $N_{l,k}^{ICI}$ so that equation (3.18) can be written as

$$R_{l,k} = (e^{j\pi\phi_k} \cdot e^{j2\pi\frac{lN_s + N_g}{N}\phi_k}) \cdot \sin c(\phi_k) X_{l,k} C_{l,k} + N_{l,k}^{ICI} + N_{l,k} \qquad (3.21)$$

and the power of $N_{l,k}^{ICI}$ is approximately equal to [17]:

$$P_k^{ICI} \approx \frac{\pi^2}{3} |H_k|^2 \phi_k^2 \qquad (3.22)$$

3.3 Channel Model

The performance of wireless system is usually influenced by channel significantly. In wireless environment, the channel changes with time randomly because the surroundings vary all the time. For example, a mobile vehicle, a moving person with his cellular phone and changes of a circumstance all cause the channel environment varied. The varying characteristic of the channel will cause the system performance degrade and inconvenience to simulations and analyses of the system. In addition, due to the physical characteristic of wave, transmitted signals suffered from the phenomenon of reflection, diffraction and scattering and these are more serious in

urban areas. Because there are obstacles and reflectors in the wireless propagation channel, the transmitted signal arrivals at the receiver from various directions over a multiplicity of paths. Such a phenomenon is called *multipath.* It is an unpredictable set of reflections and/or direct waves each with its own degree of attenuation and delay.

Multipath is usually described by

- **Line-of-sight (LOS)**: the direct connection between the transmitter (TX) and the receiver (RX).
- **Non-line-of-sight (NLOS)**: the path arriving after reflection from reflectors.

The illustration of LOS and NLOS is shown in Figure 3-2.
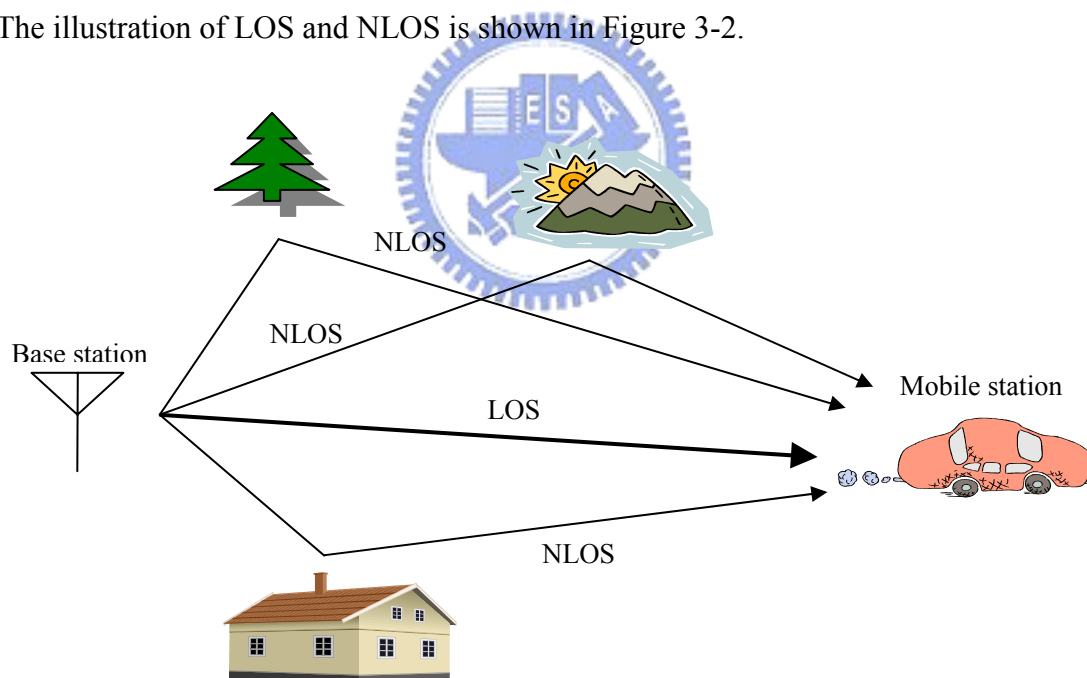
Figure 3-2 multipath environment diagram

3.3.1   Multipath Channel Model

In this thesis, we use a multipath Rayleigh fading channel model to simulate the wireless channel. As illustrated in Figure 3-3, the channel effects are comprised of multipath interference, path loss and Rayleigh fading.
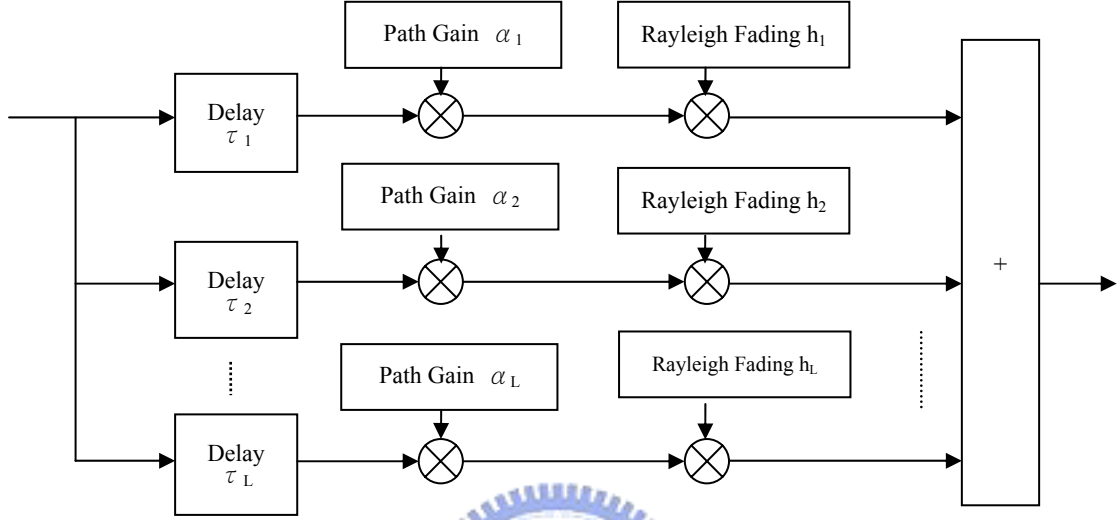
Figure 3-3 multipath Rayleigh fading channel model

In time domain, we usually characterize the channel impulse response h(τ,t), with a time-varying tapped delay line filter :

$$h(\tau,t) = \sum_{i=1}^{L} \beta_i(t)\delta(\tau - \tau_i(t))e^{j\phi_i(t)} \qquad (3.23)$$

L is the number of paths. For every path, there are three parameters to describe it: path delay τ_i, signal attenuation at this path β_i and signal phase rotation caused by this path φ_i. The path delay τ_i is basically decided by the distance between the transmittor and receiver, the signal attenuation β_i is determined by path energy loss α_i and Rayleigh fading h_i and the signal phase rotation is relative to the path delay, the carrier frequency and the Rayleigh fading. The relation between them is:

$$\alpha_i h_i = \beta_i e^{j\phi_i} \qquad (3.24)$$

28

Therefore, equation (3.23) can be written as:

$$h(\tau, t) = \sum_{i=1}^{L} \alpha_i(t) h_i(t) \delta(\tau - \tau_i(t)) \qquad (3.25)$$

3.3.2   Jakes Fading Model

Jakes fading model is a deterministic method for simulating time-correlated Rayleigh fading waveforms and is still widely used nowadays. It uses a set of complex sinusoids to approach the Rayleigh distribution and the number of sinusoids must be sufficiently large that the pdf of the resulting envelope of simulating waveform provides an acceptably accurate approximation.

Considering a two-dimensional multipath propagation model, the baseband expression of the waveform can be written as a superposition of plane waves:

$$T(t) = E_0 \sum_{n=1}^{N} c_n e^{j(\omega_m t \cos\alpha_n + \phi_n)} \qquad (3.26)$$

Where E_0 is the waveform power, c_n is the strength of nth rays, N is the number of arrival rays, $w_m = 2\pi f v$ is the maximum Doppler shift where v is the mobile velocity, f is the frequency of the carrier, and c is the speed of light, α_n are the arrival angles, and φ_n are the phases of the nth arrival wave.

Jakes model assumes that the N arrival paths are equal-strength and with uniformly distributed arrival angles:

$$c_n = \frac{1}{\sqrt{N}} \qquad (3.27)$$

$$\alpha_n = \frac{2\pi n}{N}, \qquad n = 1, 2, ..., N \qquad (3.28)$$

Figure 3-4 shows path arrival angles in Jakes model. From that, we can see there is quadrantal symmetry in the magnitude of the Doppler shift, except for angles 0 and π. Using this character, equation (3.26) can be simplified to:

$$T(t) = T_c(t) + j \cdot T_s(t) \tag{3.29}$$

$$T_c(t) = \frac{E_0}{\sqrt{N}}(\sqrt{2}\sum_{n=1}^{N_0} \cos \beta_n \cos \omega_n t + \cos \alpha \cos \omega_m t + \theta_0) \tag{3.30}$$

$$T_s(t) = \frac{E_0}{\sqrt{N}}(\sqrt{2}\sum_{n=1}^{N_0} \sin \beta_n \cos \omega_n t + \sin \alpha \cos \omega_m t + \theta_n) \tag{3.31}$$

where $T_c(t)$ is the real part of $T(t)$, $T_s(t)$ is the imaginary part of $T(t)$, $N_0 = (N/2-1)/2$, α and β_n are phases, and θ_n are initial phases usually set to zero. Setting $\alpha = 0$ and $\beta_n = \pi n/(N_0+1)$ gives zero cross-correlation between $T_c(t)$ and $T_s(t)$.
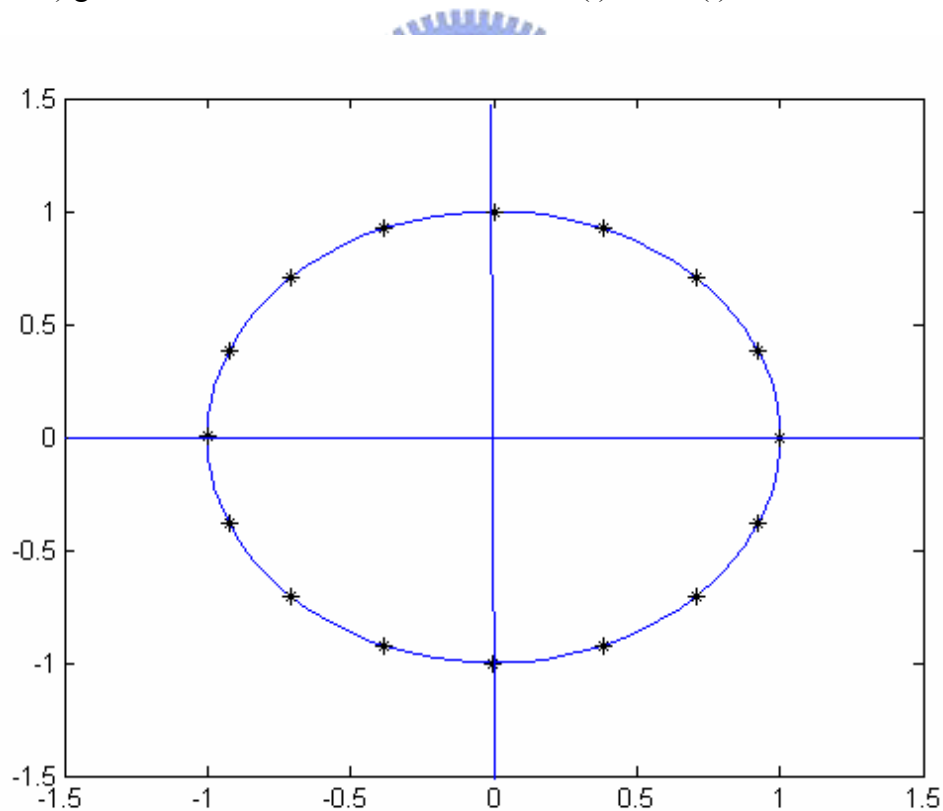
Figure 3-4 path arrival angles

To generate L multipath waveforms:

$$T(t) = T_{c,k}(t) + j \cdot T_{s,k}(t), \qquad k = 1,2,...,L \qquad (3.32)$$

$$T_{c,k}(t) = \frac{E_0}{\sqrt{N}} (\sqrt{2} \sum_{n=1}^{N_0} \cos \beta_n \cos \omega_n t + \cos \alpha \cos \omega_m t + \theta_{0k}) \qquad (3.33)$$

$$T_{s,k}(t) = \frac{E_0}{\sqrt{N}} (\sqrt{2} \sum_{n=1}^{N_0} \sin \beta_n \cos \omega_n t + \sin \alpha \cos \omega_m t + \theta_{nk}) \qquad (3.34)$$

Jakes suggests that using

$$\theta_{nk} = \frac{\pi n + 2\pi(k-1)}{N_0 + 1} \qquad (3.35)$$

However, it has shortcomings in the correlation functions. The independence between different waveforms is not good [12]. To generate uncorrelated waveforms, [12] proposed that using a orthogonal code, Walsh-Hadamard code, to eliminate the correlation between different paths. Moreover, [12] re-chooses $\alpha_n = 2\pi(n-0.5)/N$ as Figure 3-5 showed so that it provide quadrantal symmetry for all Doppler shifts and it leads to equal power oscillators. After all, the model is modified to:

$$T_k(t) = \frac{E_0}{\sqrt{N}} \sum_{n=1}^{N_0} A_k(n)(\cos \beta_n + j \cdot \sin \beta_n) \cos(\omega_n t + \theta_n), \quad k = 1,2,...,L \qquad (3.36)$$

where $N_0 = N/4$, $\alpha_n = 2\pi(n-0.5)/N$, $\beta_n = \pi n/N0$, θ_n are the independent random phases, each of which is uniformly distributed in $[0,2\pi)$ and $A_k(n)$ is the kth Walsh-Hadamard codeword in n which satisfies

$$\frac{1}{N_0} \sum_{n=1}^{N_0} A_k^*(n) A_l(n) = \begin{cases} 1, & k = l \\ 0, & k \neq l \end{cases} \qquad (3.37)$$

31
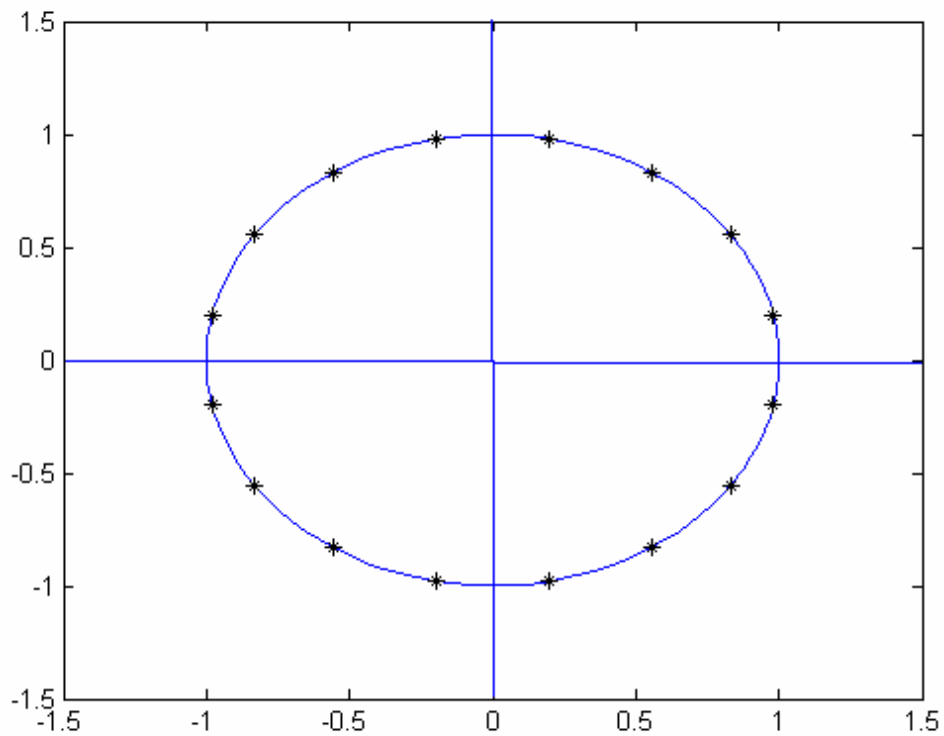
Figure 3-5 modified path arrival angles

The modified Jakes fading model is illustrated in Figure 3-6 and Figure 3-7 (a), (b), and (c) show the variation of channel total power with mobile velocities, 100,200 and 300 km/hr respectively.
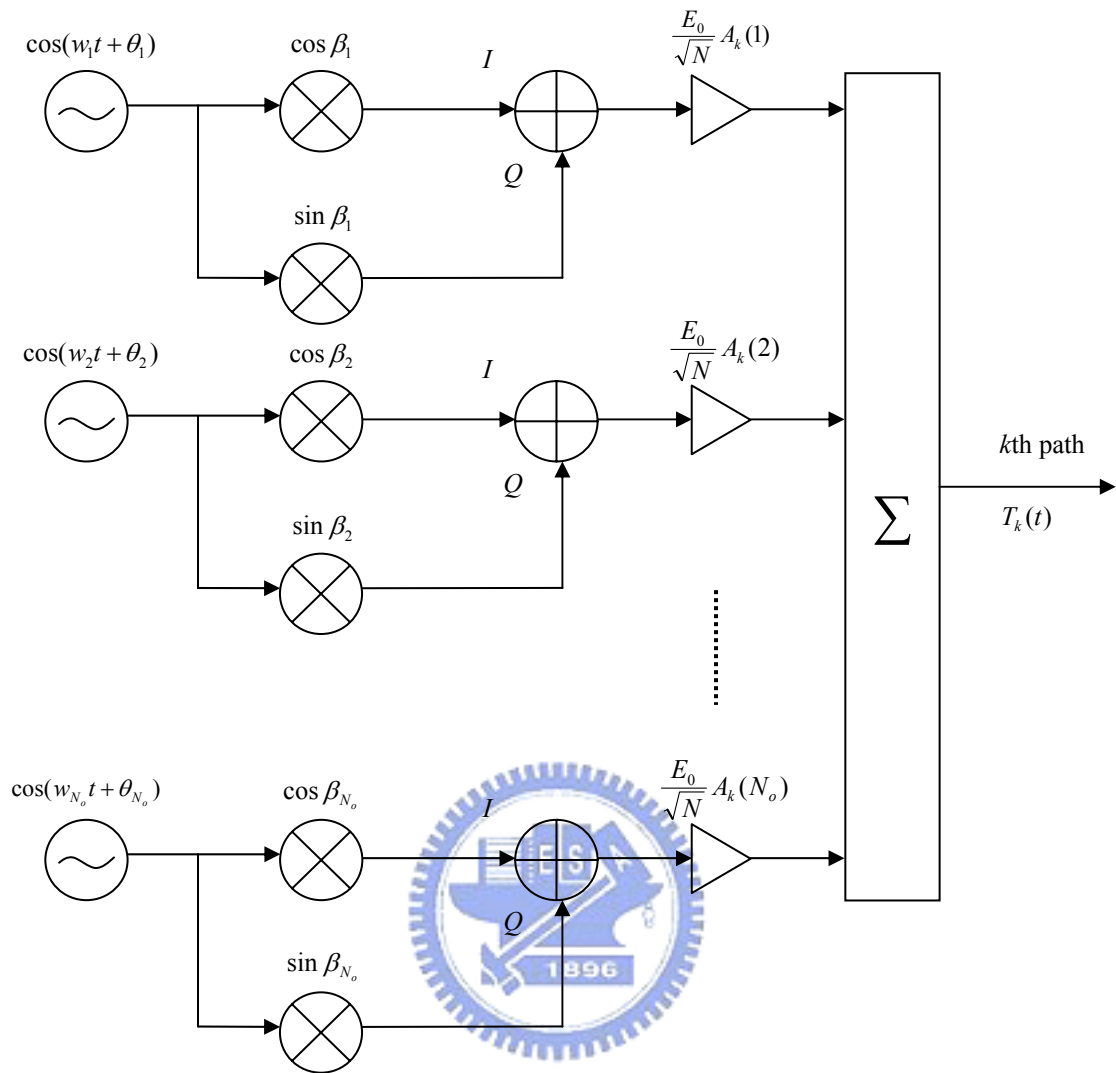
Figure 3-6 modified Jakes fading model

channel power, speed = 100 km/hr
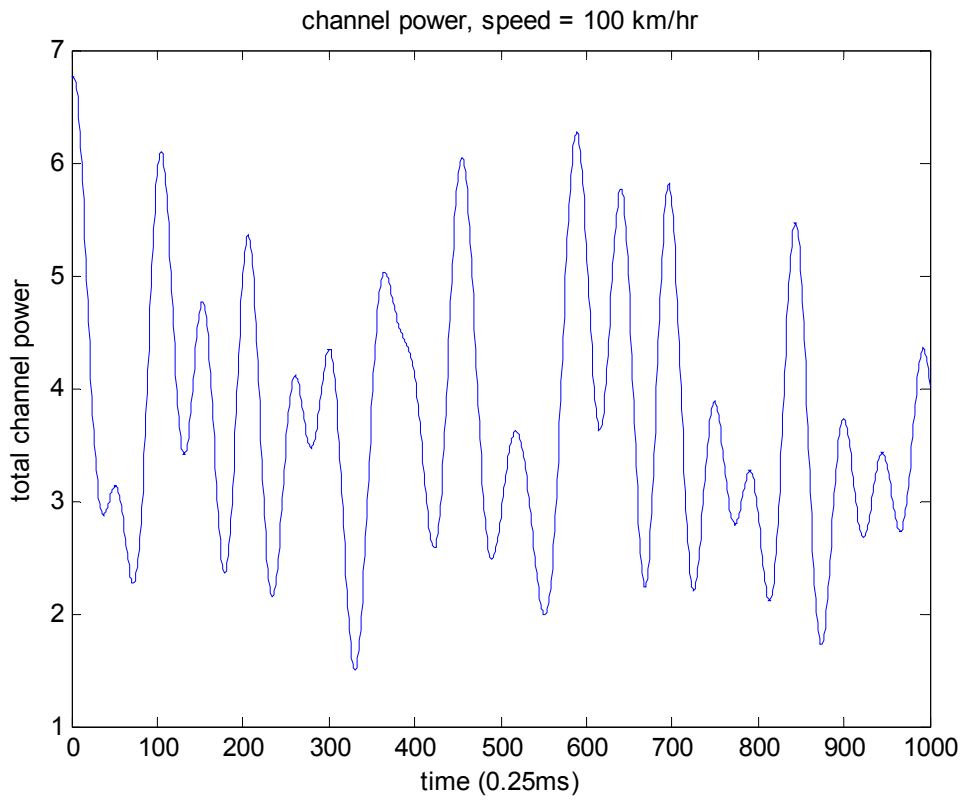
Figure 3-7 (a) channel power variation at a velocity of 100 km/hr

channel power, speed = 200 km/hr
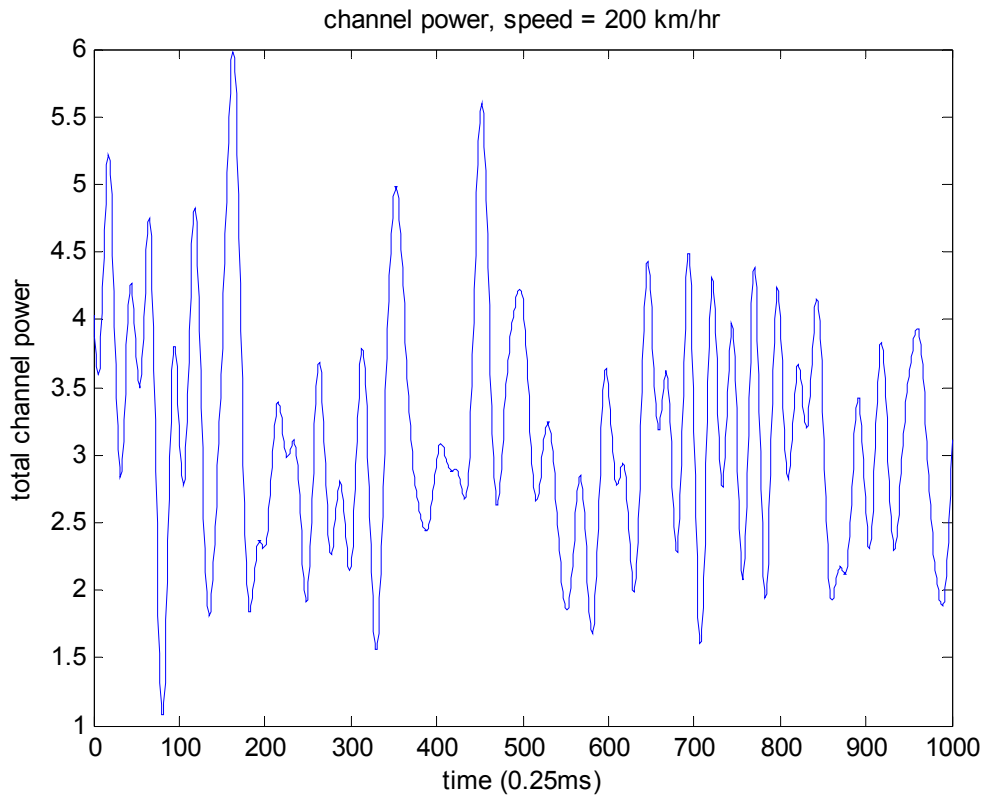
Figure 3-7 (b) channel power variation at a velocity of 200 km/hr

34
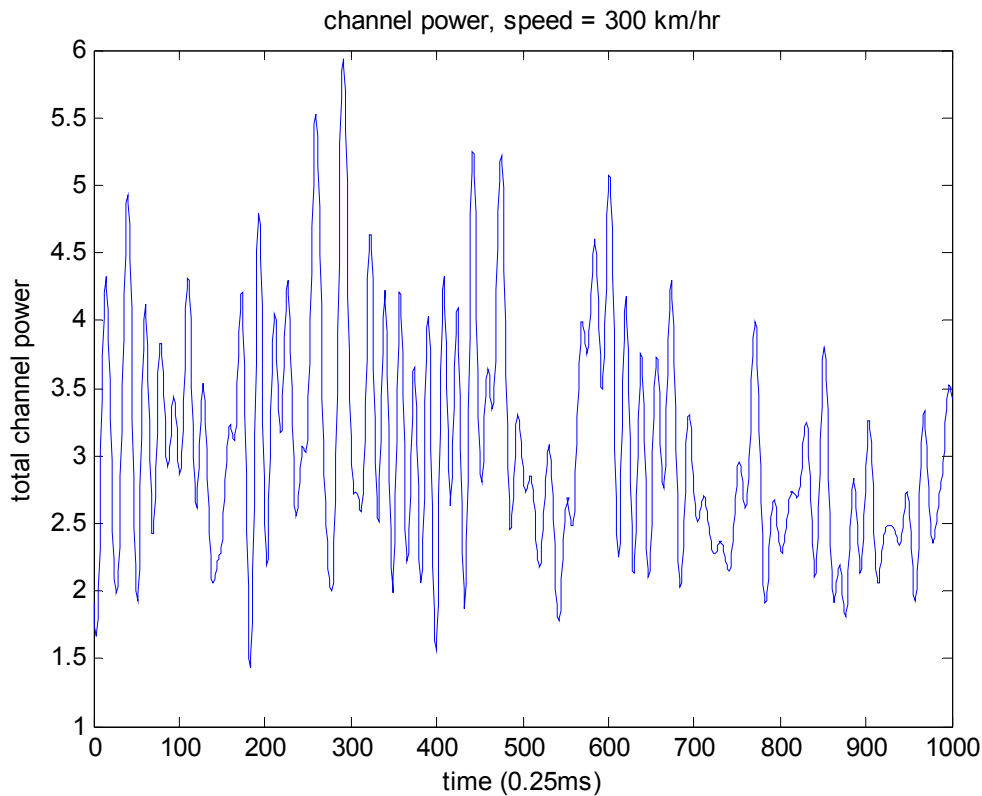
Figure 3-7 (c) channel power variation at a velocity of 300 km/hr

3.3.3 COST207 Channel Model

In a wireless system, the channel is different for various areas. In this thesis, we use the channel models established in COST207 to simulate the actual channel model. The channel models in COST207 are set up by the organization, European Co-operation in the field of Scientific and Technical research. They surveyed the wireless channels in French, Britain, Holland, Sweden, and Switzerland during 1984~1988. COST207 is a tapped delay line model and contains tap weights and Doppler spectra of four different areas: Rural Area (RA), Typical Urban Area (TU), Bad Urban Area (BU), and Hilly Terrain (HT). The power delay profiles of them are showed in mathematic forms below and graphs in Figure 3-8.

1. Rural Area (RA)

$$P(\tau) = \begin{cases} e^{-9.2\tau/\mu s}, & 0 < \tau < 0.7\,\mu s \\ 0, & elsewhere \end{cases} \qquad (3.38)$$

2. Typical Urban Area (TU)

$$P(\tau) = \begin{cases} e^{-\tau/\mu s}, & 0 < \tau < 7\,\mu s \\ 0, & elsewhere \end{cases} \qquad (3.39)$$

3. Bad Urban Area (BU)

$$P(\tau) = \begin{cases} e^{-\tau/\mu s}, & 0 < \tau < 5\,\mu s \\ 0.5e^{5-\tau/\mu s}, & 5 < \tau < 10\,\mu s \\ 0, & elsewhere \end{cases} \qquad (3.40)$$

4. Hilly Terrain (HT)

$$P(\tau) = \begin{cases} e^{-3.5\tau/\mu s}, & 0 < \tau < 2\,\mu s \\ 0.1e^{15-\tau/\mu s}, & 15 < \tau < 20\,\mu s \\ 0, & elsewhere \end{cases} \qquad (3.41)$$
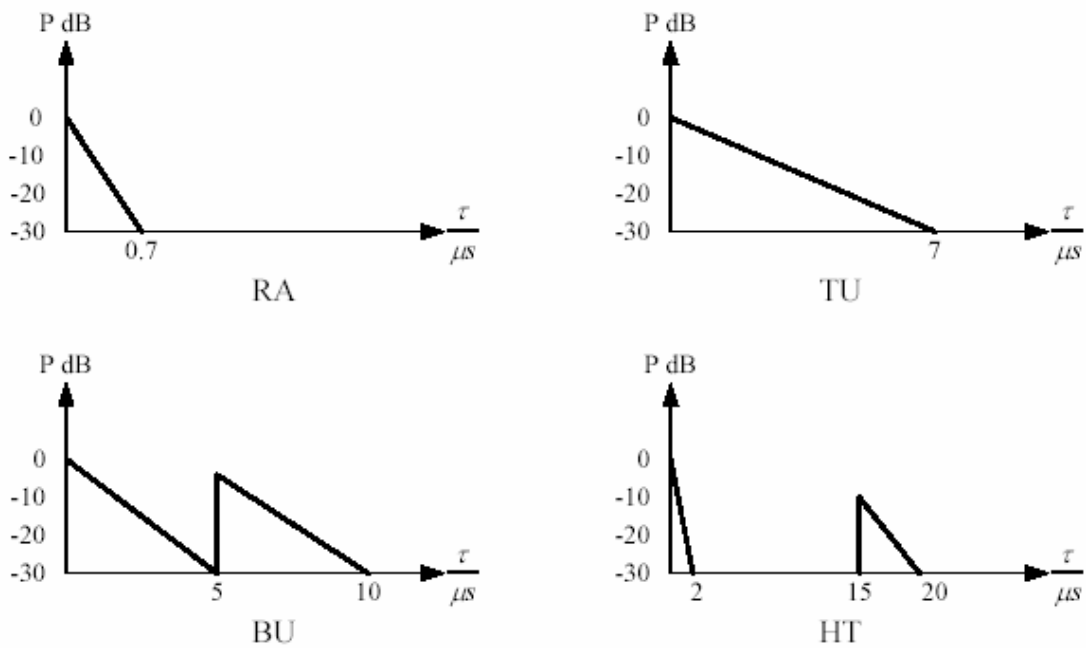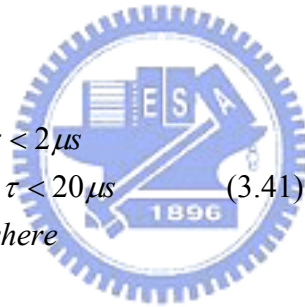
Figure 3-8 power delay profiles for COST207 channels

Chapter 4
Sampling Clock Synchronization

This chapter is mainly focused on sampling clock synchronization. At the beginning, we introduce the effect of sampling clock error at a receiver. After that, we propose two schemes for the detection of clock offset. One is post-FFT algorithm, which is used in DVB-T system traditionally; the other is pre-FFT strategy, which is proposed here for the mobile environment. After detecting the clock error, we should compensate for the effects by the estimated timing offsets. We first introduce two kinds of compensating methods that are commonly used. Then, we show the mechanism of timing recovery for our inner receiver design. Finally, we present the performance comparison of compensating methods comparison between our proposed and traditional algorithm for clock error detection.

4.1 Effect of Sampling Clock Error

The crystal oscillation components are typically used as the clock reference to trigger integrated circuit. However, no matter how precise the crystal components oscillate, there is always an error in oscillated frequency between any two of them. Therefore, the sampling period of ADC (Analog to Digital Converter) at receiver is

not one hundred percent identical to that of DAC at transmittor. The difference is called "sampling clock offset". Figure 4-1 illustrates the sampling clock error problem. The timing error caused by a sampling clock offset is accumulated with the number of sampling point. As we can see, the last sample point of symbol 1 drifts from the correct point by e_1. After symbol 2, the timing error of the last point is added to e_2 which is larger than e_1. At this rate, the timing error will be accumulated more and more and it can result in problem of OFDM symbol window drift which leads to incorrect samples for FFT operation as shown in Figure 4-2. With the mis-selection of OFDM symbol window, problem of ISI, ICI, and phase rotation is introduced and cause system performance decay significantly as shown in chapter 3. For example, for 8K mode and a sampling clock offset 100ppm, the symbol window drift reach one sample per OFDM symbol. If there is no clock synchronization, after 10000 OFDM symbol (about 10 sec) the received OFDM symbol will be completely different one from the transmitted symbol. Consequently, the sampling clock synchronization is very important to the system. In following contents, we discuss how to solve this problem.
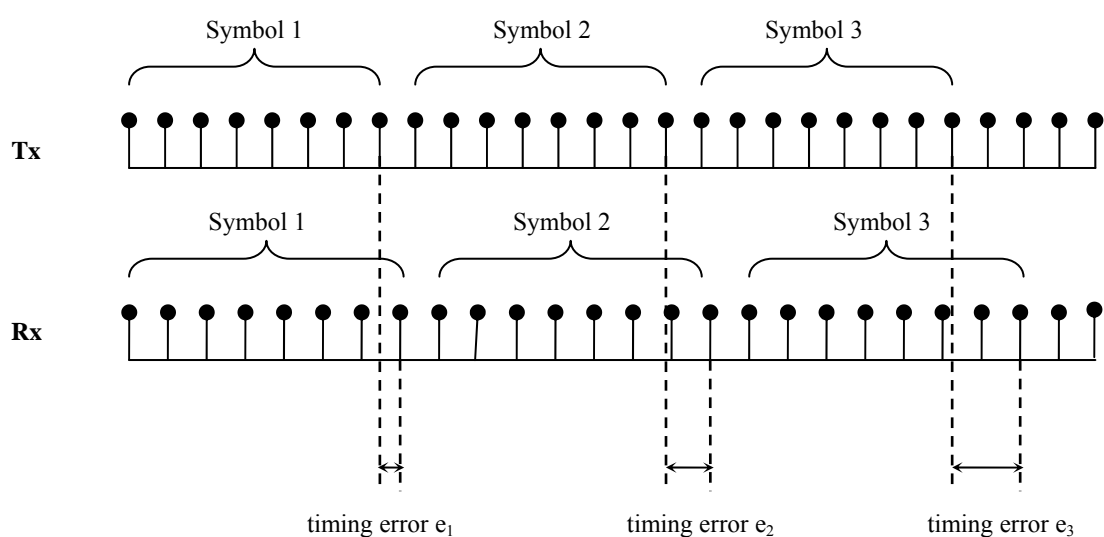
Figure 4-1 the accumulation of sampling clock error
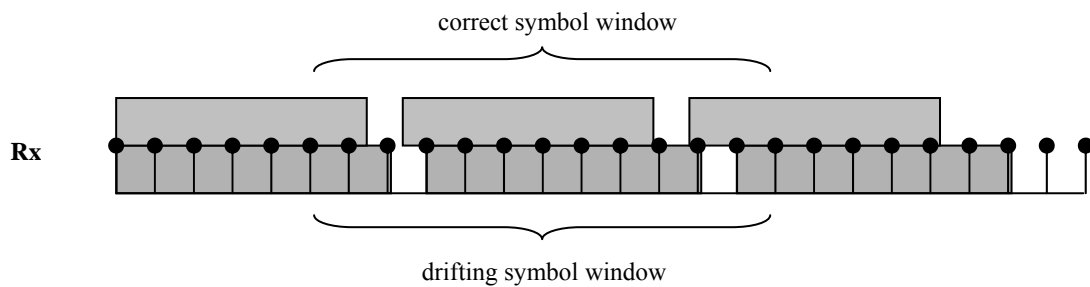
Figure 4-2 window drift of OFDM symbol

4.2 The Approach for Sampling Clock Synchronization

For sampling clock synchronization, our goal is to recover data samples as like those without clock error. For this, we first need to do is sampling clock error detection (SCED). In our following sections, we will introduce the traditional algorithm (Post-FFT one) for SCED and propose a new strategy (Pre-FFT one) for better performance in a mobile environment.

After estimating the clock error, we should conduct sampling clock error compensation (SCEC) to recover the original data without the effects of clock error. In a synchronized sampling system shown by Figure 4-3(a) [15, 16], SCED controls a VCXO (Voltage Controlled Crystal Oscillator) in order to align the receiver clock with the transmitter clock. The adjustment of the clock of the AD converter naturally removes the sampling clock offset, provided that sampling clock error detection is accurate. In this sense, it is the optimal way of performing the correction. To complete the sampling clock adjustment, we may need a Voltage-Control Crystal Oscillator (VCXO) component. In additional, to provide the analog signal to adjust the oscillation frequency of VCXO, we need a DA converter to convert the digital sampling clock error information to an analog signal. To provide precise clock

adjustment, a high-resolution DA converter is required. Although, this approach is straightforward, the extra expense on hardware components makes this approach unattractive. During the recent years, the trend in receiver design has been towards all digital receivers. Figure 4-3(b) [15, 16] illustrates one way of non-synchronized sampling system, in which the sampling clock correction is completed with a fixed crystal oscillator controlling the AD converter. There are two effects resulting from the sampling clock error. First, the useful frequency-domain signal component is rotated and attenuated. The rotation of the received symbol is compensated for in the digital domain by inversely rotating the angle caused by the clock error (Rotor) in frequency domain. The other is the ICI and unfortunately cannot be eliminated by simple angle rotation. With the Rotor compensation, the ICI problem and the signal attenuation caused by sampling clock error still remains and eventually result in the degradation of system performance. Instead, we recover the timing by resampling original data at correct sampling instants. The structure is illustrated in Figure 4-3(c). After estimating the sampling clock error, SCED controls digital resampler to resample data after ADC using interpolation. The approach gives the correct sampling point for each sample so that there is not the ICI and the signal attenuation problems. To obtain the correct signal values at the resampling points, we use interpolation technique. It is well known that interpolation is the process of estimating the intermediate values of a continuous event from discrete samples. In later sections, we present various interpolation methods for SCEC.
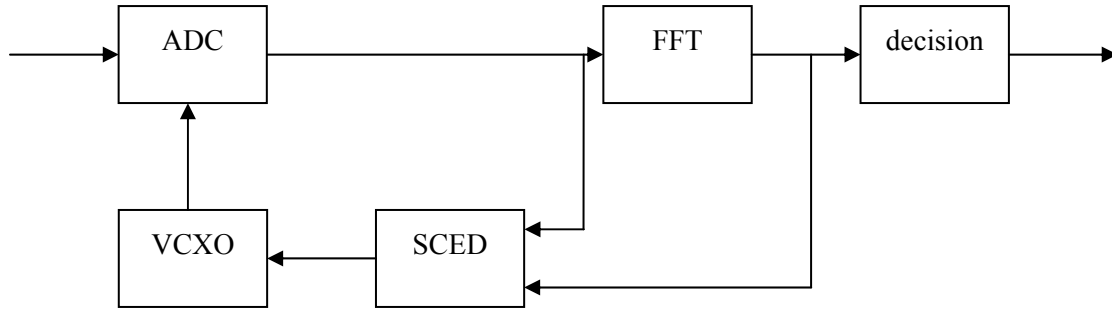
Figure 4-3 (a) a synchronized sampling system
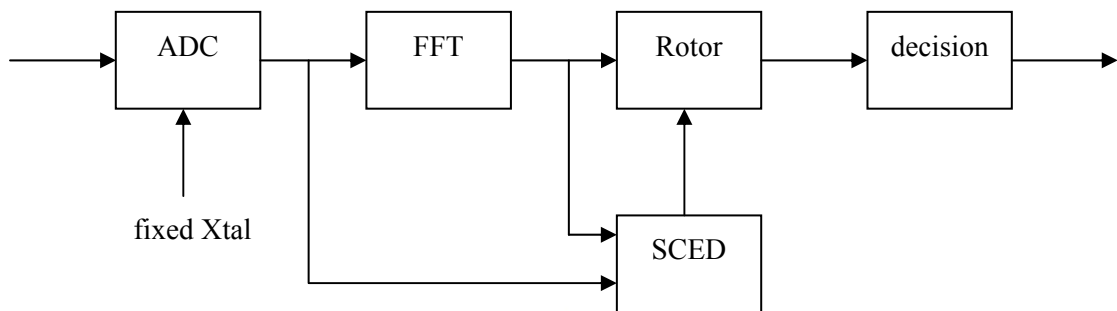
Figure 4-3 (b) a non-synchronized sampling system with Rotor
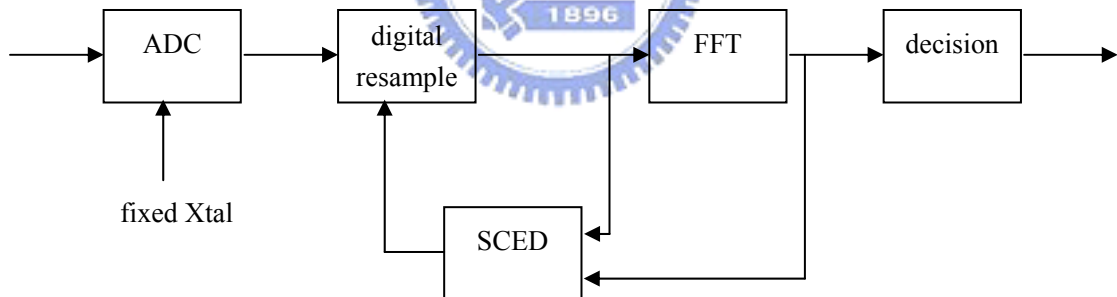
Figure 4-3 (c) a non-synchronized sampling system with digital resample

For sampling clock synchronization, we may first estimate the clock error roughly by averaging several iterations of detected clock error by SCED approach introduced later to reduce the range of clock offset. After coarse estimation, we track the smaller offset with a close-loop in Figure 4-3 (c) to get more precision estimated clock error.

4.3 Post-FFT Sampling Clock Error Detection (SCED)

Post-FFT SCED [17-19] is operated in the frequency domain. After FFT, received data in the time domain is translated into symbols in frequency domain where reference data can be used to detect the sampling clock error.

As equation (3.21), considering a carrier frequency offset Δf and a sampling clock offset t_Δ, the symbol after FFT becomes:

$$R_{l,k} = (e^{j\pi\phi_k} \cdot e^{j2\pi \frac{lN_s + N_g}{N}\phi_k}) \cdot \sin c(\phi_k) X_{l,k} C_{l,k} + N_{l,k}, \qquad k = 0,1,...,N-1 \qquad (4.1)$$

where we denote the normalized carrier offset as $\Delta f_c'$

$$\phi_k = \Delta f_c T_u + t_\Delta \cdot k = \Delta f_c' + t_\Delta \cdot k \qquad (4.2)$$

and the noise term $N_{l,k}$ includes channel noise and ICI noise.

To take out the sampling clock offset t_Δ, we utilize reference data which has value known by the receiver. Here we choose scattered pilots rather than continual pilots for SCED because of two reasons : one is that the number of scattered pilots is more than that of continual pilots which let us be able to choose more pilots with better SNR to detect t_Δ without less noise interference. The other is that the locations of scattered pilots are scattered while that of continual pilots are identical in different ODFM symbols. Considering the condition that the channel SNR of the continual pilots are all poor, it is very difficult to detect t_Δ accurately with strong noise interference. On the other hand, there are four subsets of subcarrier locations in scattered pilots and if the channel SNR of one subset are all poor, there still pilots of another three subsets can be used with less noise interference.

Suppose that k_p is a subcarrier index of a scattered pilot in *l*th OFDM symbol, as Figure 2-13 shown, the locations of scattered pilots repeat for every four OFDM symbols so that k_p is also a subcarrier index of a scattered pilot in *(l-4)*th OFDM symbol. Denote the subset of scattered pilots as *SP* and then symbols after FFT at k_pth subcarriers in *l*th and *(l-4)*th OFDM symbols are:

$$R_{l,k_p} = (e^{j\pi\phi_{k_p}} \cdot e^{j2\pi\frac{lN_s+N_g}{N}\phi_{k_p}}) \cdot \sin c(\phi_{k_p})X_{l,k_p}C_{l,k_p} + N_{l,kp}, \quad k_p \in SP \qquad (4.3)$$

$$R_{l-4,k_p} = (e^{j\pi\phi_{k_p}} \cdot e^{j2\pi\frac{(l-4)N_s+N_g}{N}\phi_{k_p}}) \cdot \sin c(\phi_{k_p})X_{l-4,k_p}C_{l-4,k_p} + N_{l-4,kp}, \quad k_p \in SP \qquad (4.4)$$

Correlate $R_{l,kp}$ with $R_{l-4,kp}$ and we get :

$$Y_{l,k_p} = R_{l,k_p} \cdot R^*_{l-4,k_p} = e^{j2\pi\frac{4N_s}{N}\phi_{k_p}} \cdot (X_{l,k_p} \cdot X^*_{l-4,k_p}) \cdot (H_{l,k_p} \cdot H^*_{l-4,k_p}) \qquad (4.5)$$

The phase of the correlation $Y_{l,k}$ is :

$$\angle Y_{l,k_p} = 2\pi\frac{4N_s}{N}\phi_{k_p} + \angle(X_{l,k_p} \cdot X^*_{l-4,k_p}) + \angle(C_{l,k_p} \cdot C^*_{l-4,k_p}) \qquad (4.6)$$

As mentioned in chapter 4, the values of pilots in DVB-T system are all real number so that

$$\angle(X_{l,k_p} \cdot X^*_{l-4,k_p}) = 0 \qquad (4.7)$$

and equation (4.6) becomes

$$\angle Y_{l,k_p} = 2\pi\frac{4N_s}{N}\phi_{k_p} + \angle(C_{l,k_p} \cdot C^*_{l-4,k_p}) \qquad (4.8)$$

Under the condition of slow-fading channel, the variation of the channel during four OFDM symbol is very small and can be neglected so that $C_{l-4,k}$ is roughly equal to $C_{l,k}$. Therefore, the correlation of $C_{l,k}$ and $C_{l-4,k}$ and its phase are

$$C_{l,k_p} \cdot C^*_{l-4,k_p} \approx |C_{l,k_p}|^2 \qquad (4.9)$$

$$\angle\{C_{l,k_p} \cdot C^*_{l-4,k_p}\} \approx 0 \qquad (4.10)$$

and it leads to equation (4.8) changes to

$$\angle Y_{l,k_p} = 2\pi \frac{4N_s}{N} \phi_{k_p} \qquad (4.11)$$

Consequently, φ_{kp} can be detected from the phase of $Y_{l,kp}$:

$$\phi_{k_p} = \frac{\angle Y_{l,k_p}}{2\pi \cdot 4N_s / N}, \quad k_p \in SP \qquad (4.12)$$

From equation (4.2), φ_k is linear equation of k with a slope of t_Δ and the section of y axis is Δf_c'. Hence, we can find a line approaching equation (4.12) to detect not only the sampling clock offset t_Δ but also carrier frequency offset Δf_c as illustrated in Figure 4-4.
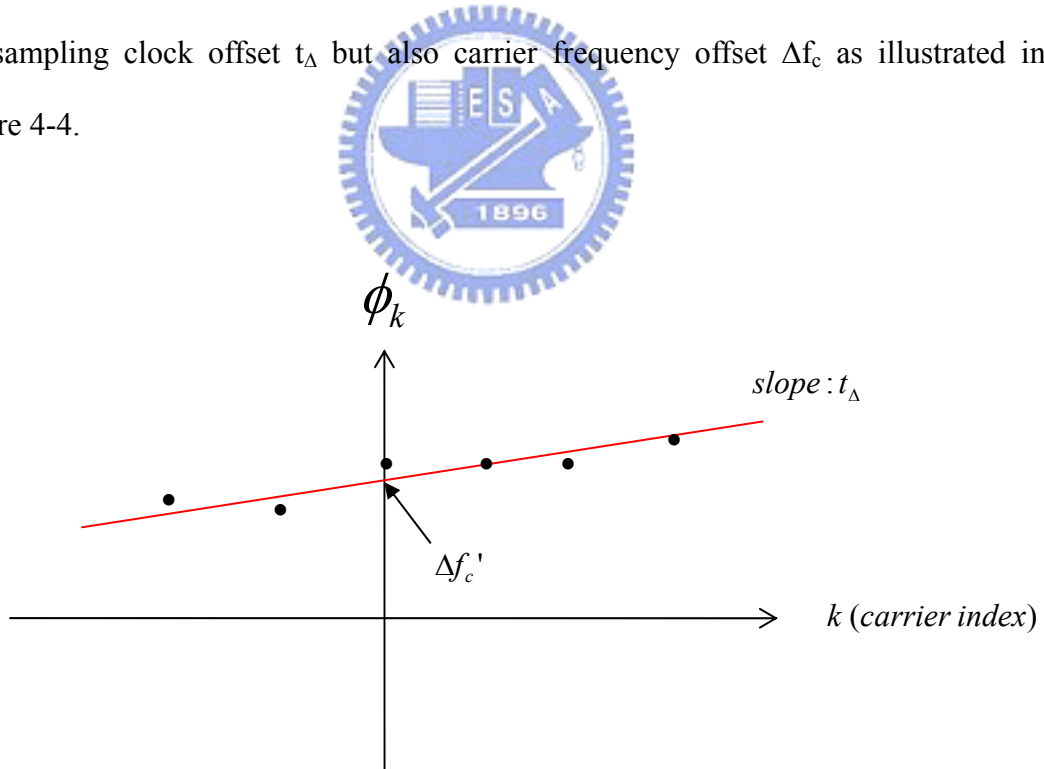
Figure 4-4 fitting line of φ_k

To find this line, a simple criterion is Least-Squares Curve-Fitting (LSCF) [20], the principle of which is that using the relation of inputs and outputs to find unknown

elements by minimizing the summation of the squares of error between observed outputs and correct outputs. Here, inputs are φ_{kp}, k_p: {scattered pilots}, and want to find a line

$$\phi_k = \hat{t}_\Delta k + \Delta \hat{f}_c' \qquad (4.13)$$

to fit LSCF criterion. Therefore, the estimated sampling clock offset and carrier frequency offset are

$$\{\hat{t}_\Delta, \Delta f_c'\} = \arg\left\{\min_{\hat{t}_\Delta, \Delta \hat{f}_c'} E_{\hat{t}_\Delta, \Delta \hat{f}_c'}\right\} \qquad (4.14)$$

where $E_{\hat{t}_\Delta, \Delta \hat{f}_c'}$ is the square error

$$E_{\hat{t}_\Delta, \Delta \hat{f}_c'} = \sum_{p=1}^{N_p} (\phi_{kp} - (\hat{t}_\Delta k_p + \Delta \hat{f}_c')) \qquad (4.15)$$

and N_p is the number of scattered pilots. To find the minimum of the square error, let its partial differentials be equal to zero:

$$\begin{cases} \dfrac{\partial E_{\hat{t}_\Delta, \Delta \hat{f}_c'}}{\partial \hat{t}_\Delta} = 0 \\[4mm] \dfrac{\partial E_{\hat{t}_\Delta, \Delta \hat{f}_c'}}{\partial \Delta \hat{f}_c'} = 0 \end{cases} \qquad (4.16)$$

As a result, solving this simultaneous equations lead to the estimations:

$$\hat{t}_\Delta = \frac{N_p \cdot \sum_{p=1}^{N_p} \phi_{k_p} k_p - (\sum_{p=1}^{N_p} k_p) \cdot (\sum_{p=1}^{N_p} \phi_{k_p})}{N_p \cdot \sum_{p=1}^{N_p} k_p{}^2 - (\sum_{p=1}^{N_p} k_p)^2} \qquad (4.17)$$

$$\Delta \hat{f}_c' = \frac{(\sum_{p=1}^{N_p} k_p{}^2) \cdot (\sum_{p=1}^{N_p} \phi_{k_p}) - (\sum_{p=1}^{N_p} k_p) \cdot \sum_{p=1}^{N_p} \phi_{k_p} k_p}{N_p \cdot \sum_{p=1}^{N_p} k_p{}^2 - (\sum_{p=1}^{N_p} k_p)^2} \qquad (4.18)$$

At this moment, the clock and carrier offsets are both detected. Equation (4.17) can be utilized for coarse clock offset estimation and the tracking of a clock offset. Equation (4.18) is made use of the tracking of a carrier offset in chapter 6.

The equations above use all scattered pilots to estimate clock and carrier offsets. However, there are some pilots which suffer deep fading from the channel and may be disturbed by channel noise largely. A better way is choosing the pilots with better channel SNR. In this way, it can not only save the computation complexity but also promote the performance of estimation due to fewer effect by channel noise. Moreover, we can use a weighted form for estimation, that is, give more weight to the pilots with larger SNR.

4.3.1 Synchronization Problem in a Fast-fading Channel

In the discussion above, we assume that the channel is slow fading. For a mobile environment, however, the channel is not static. Figure 4-5 (a),(b), and (c) shows the variation of the phase of channel frequency response at a mobile velocity 100, 200, and 300km/hr respectively. We can see from Figure 4-5 that the variation of the channel during four OFDM symbol is very fast so that the phase of the correlation of $C_{l,k}$ and $C_{l-4,k}$ cannot be ignored. For example, the phase variation between 25th and 29th OFDM symbol in Figure 4-5 (c) is almost one rad. As a result, equation (4.12) must be modified to

$$\hat{\phi}_{k_p} = \frac{\angle Y_{l,k_p}}{2\pi \cdot 4N_s / N} + \frac{\angle(C_{l,k_p} \cdot C^*_{l-4,k_p})}{2\pi \cdot 4N_s / N}, \quad k_p \in SP \qquad (4.19)$$

ϕ_{kp} is disturbed by the correlation term of varying channel and it follows to effect the estimation of sampling clock error notably. It is potential problem for post-FFT SCED

and we will display its tracking diagram in static and mobile environments later.
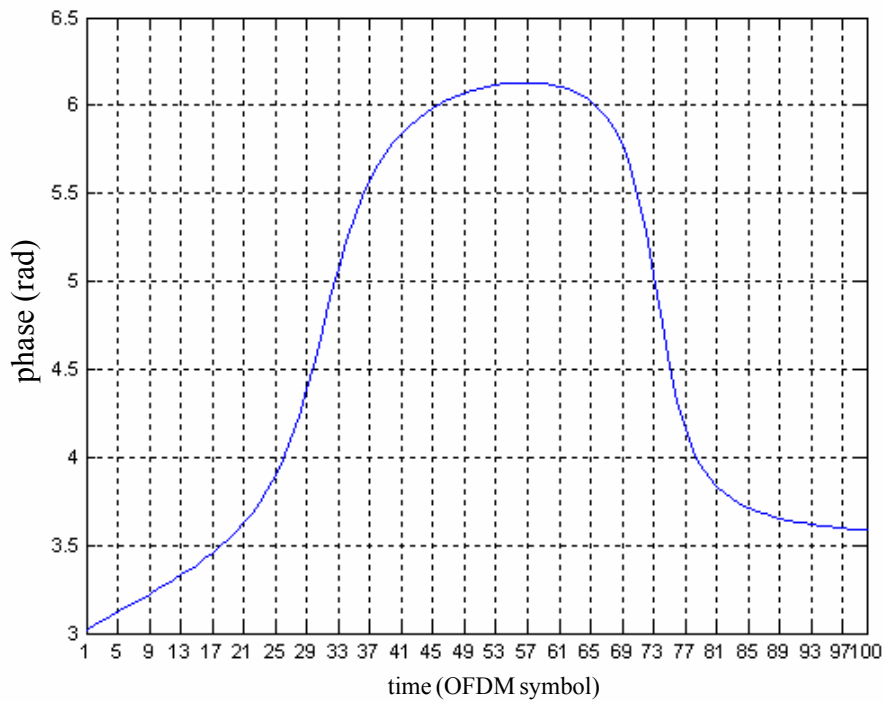
Figure 4-5 (a) the variation of the phase of channel response for 500th subcarrier with a velocity of 100 km/hr
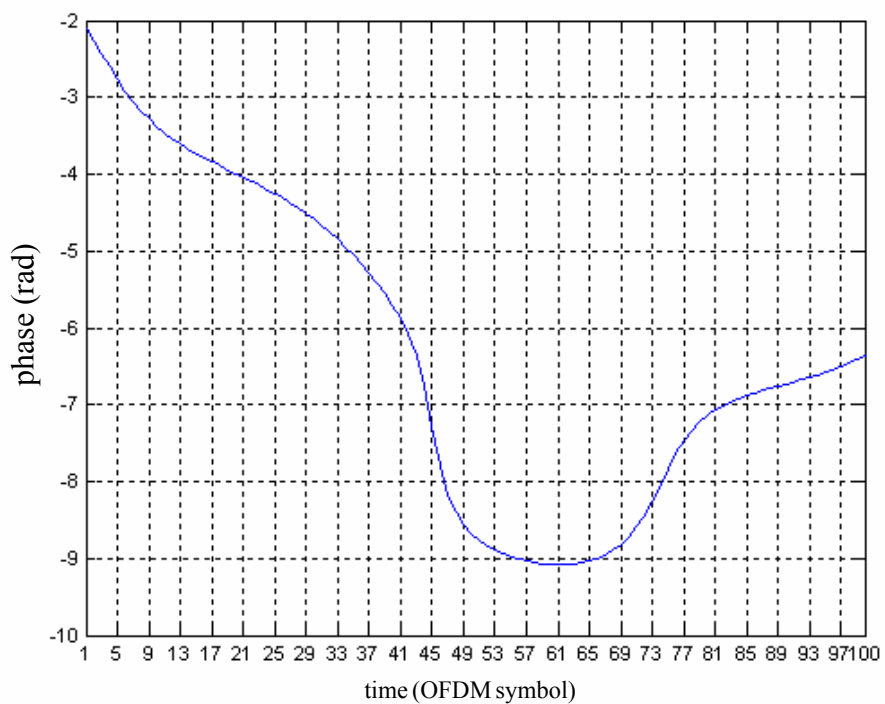
Figure 4-5 (b) the variation of the phase of channel response for 500th subcarrier with a velocity of 200 km/hr
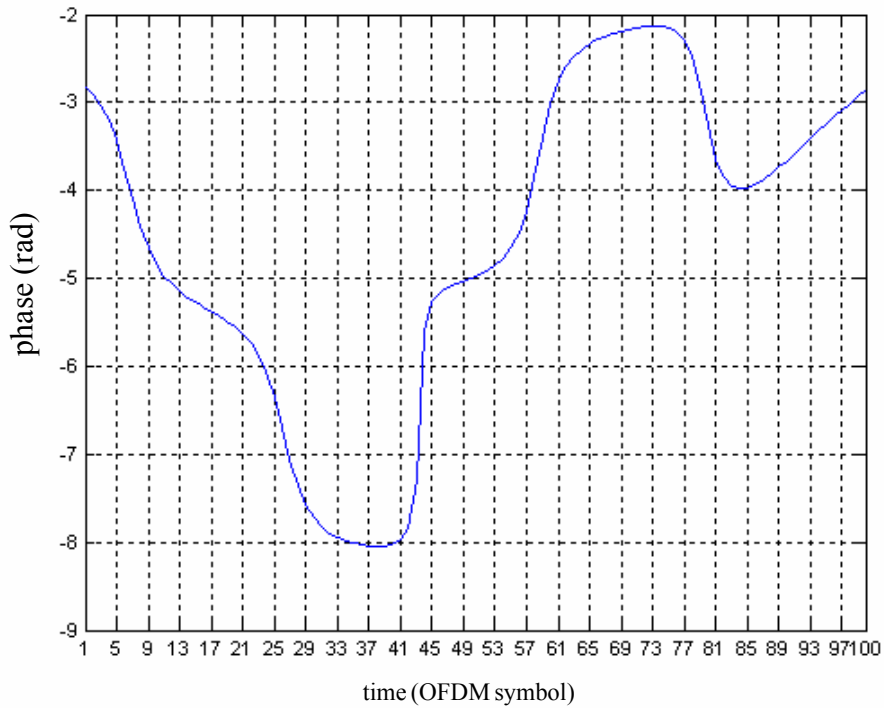
Figure 4-5 (c) the variation of the phase of channel response for 500th subcarrier with a velocity of 300 km/hr

4.4 Proposed Pre-FFT SCED

The traditional method for SCED operates after FFT (i.e. in frequency domain). In this section, we propose a new algorithm for SCED which handles before FFT (i.e. in time domain). For DVB-T, there is no reference data in time domain and the information can be utilized in time domain is only the guard interval. In an OFDM symbol, guard interval is the copy of last part of OFDM symbol so that we make use of this cyclic property for SCED.

Provided that the OFDM symbol window is found correctly, the samples of the lth OFDM symbol is

$$\{r_{l,0}, r_{l,1}, ..., r_{l,N_s-1}\} \qquad (4.20)$$

with sampling time

$$\{t_{l,0}, t_{l,1}, ..., t_{l,N_s-1}\} \qquad (4.21)$$

which can also be written as

$$\{t_{l,0}, t_{l,0} + T_s', ..., t_{l,0} + (N_s - 1)T_s'\} \qquad (4.22)$$

Without loss of generality, we assume that the sampling period at transmittor is equal to unit so that T_s' can be written as

$$T_s' = 1 + t_\Delta \qquad (4.23)$$

and sampling time can be further changed to

$$\{t_{l,0}, t_{l,0} + (1 + t_\Delta), ..., t_{l,0} + (N_s - 1)(1 + t_\Delta)\} \qquad (4.24)$$

The timing location is illustrated in Figure 4-6 (a).

   Assume that the sampling time of $r_{l,0}$, $t_{l,0}$, is correct, then the correct sampling time of the nth sample of the lth OFDM symbol is $(t_{l,0} + n)$. However, because of a sampling clock error, there is a timing error of $n \cdot t_\Delta$ for the nth sample. For example, the sampling instant of Nth data is $t_N = t_0 + N(1 + t_\Delta)$ but the correct samples should be sampled at $t_{N,c} = t_0 + N$ as Figure 4-6 (b) shown.
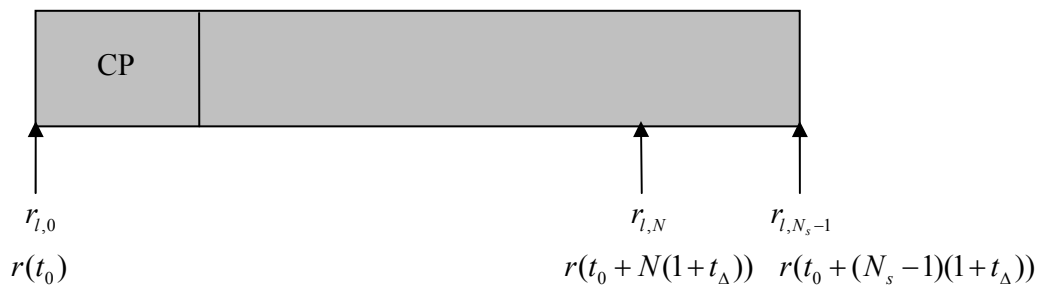
Figure 4-6 (a) timing diagram for samples in one OFDM symbol
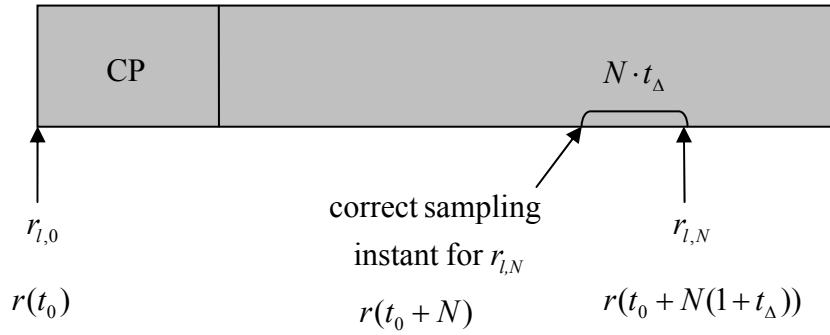
Figure 4-6 (b) timing diagram for the Nth samples

With the express of Taylor Series

$$f(x) = f(x_0) + f'(x_0) \cdot (x - x_0) + \frac{1}{2!} f''(x_0) \cdot (x - x_0)^2 + \dots \qquad (4.25)$$

we can relate $r(t_0 + n)$ and $r(t_0 + n(1 + t_\Delta))$ as

$$r(t_{l,0} + n(1 + t_\Delta)) = r(t_{l,0} + n) + r'(t_{l,0} + n) \cdot (nt_\Delta) + \frac{1}{2!} r''(t_{l,0} + n) \cdot (nt_\Delta)^2 + \dots \qquad (4.26)$$

Because the sampling clock offset is usually small, here we neglect the terms after derivation of second order in equation (4.26) and it gives

$$r(t_{l,0} + n(1 + t_\Delta)) \approx r(t_{l,0} + n) + r'(t_{l,0} + n) \cdot (nt_\Delta) \qquad (4.27)$$

Therefore, the sampling clock offset can be estimated approximately as:

$$t_\Delta \approx \frac{r(t_{l,0} + n(1 + t_\Delta)) - r(t_{l,0} + n)}{n \cdot r'(t_{l,0} + n)} \qquad (4.28)$$

At present, there are two problems to detect t_Δ from equation (4.28): first, $r(t_{l,0} + n)$, the nth sample with correct sampling timing is not known by the receiver. The other is how to find the first order deviation of $r(t_{l,0} + n)$.

To solve the first problem, we utilize the cyclic property of the guard interval. Let n equal to the FFT size N, hence there are

$$r(t_{l,0} + N) = r(t_{l,0}) \qquad (4.29)$$

$$r'(t_{l,0} + N) = r'(t_{l,0}) \qquad (4.30)$$

With this term, the unknown point $r(t_{l,0} + n)$ can be replaced by $r(t_{l,0})$ and all points in guard interval can use this property to estimate t_Δ :

$$t_\Delta \approx \frac{r(t_{l,i} + N(1 + t_\Delta)) - r(t_{l,i})}{N \cdot r'(t_{l,i})}, \quad i = 0,1,...,N_g - 1 \qquad (4.31)$$

Accordingly, the remaining work for the detection of t_Δ is how to find the first order deviation of $r(t_{l,i})$.

In order to find $r'(t_{l,i})$, we can apply a digital differentiator. For our clock recovery scheme, we choose the digital differentiator by B-spline technique to do it and the combinational digital filters is shown in Figure 4-7. With respect to B-spline and its principle, we will give an introduction and discuss in later section.
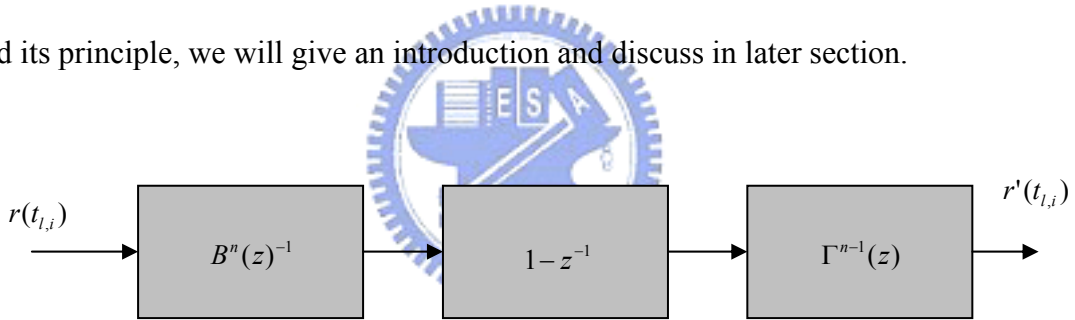
Figure 4-7 first order deviation using B-spline

In OFDM system, the guard interval, CP, is designed to prevent the ISI problem; naturally, the guard interval will suffer from ISI effect as shown in Figure 4-8. For our proposed pre-FFT SCED, we can use the ISI-free part to avoid the ISI interference. Otherwise, we can still make use of the part suffered from ISI and treat the ISI as an additional noise. With the mechanism of the sampling clock recovery loop in Figure 4-3 (c), the additional noise from ISI is eliminated and does not affect the performance of sampling clock synchronization significantly.

channel length

CP

Δ

ISI

ISI-free part Ω
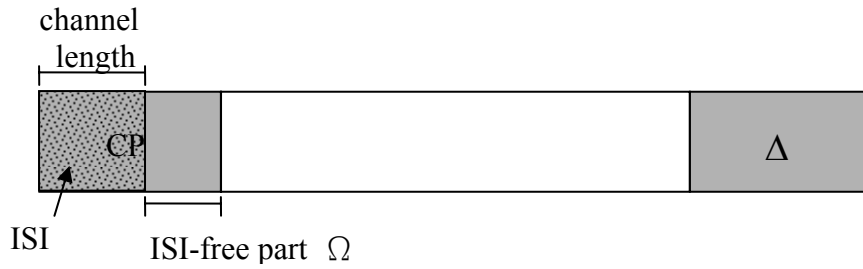
Figure 4-8 the guard interval with ISI effect

4.5 Sampling Clock Error Compensation (SCEC)

After detecting the sampling clock error, all we need to do is to compensate for effects caused by this error. Our scheme for SCEC is to resample the data in time domain as shown in Figure 4-3 (c) [21]. We recover the timing by resampling original data at correct sampling instants.

The goal of the resampler is to obtain received samples with correct sampling timing. As illustrated in Figure 4-9 (a), the period of input samples is T_s' and we want to have samples with correct period T_s. Reconstructing the continuous signal y(t) by input samples with period of T_s' with a reconstruct filter $R_I(t)$ and then resampling the reconstructed signal y(t) with the wanted period of T_s. The concept of resampler can be modeled as a concept of interpolator and is a fictitious, hybrid analog/digital method of rate conversion. The equivalent model is shown in Figure 4-9 (b).

$x(mT_s')$ → interpolation → $y(kT_s)$

(a)

$x(mT_s')$ → reconstruct filter $R_I(t)$ → $y(t)$ → ⊠ → $y(kT_s)$

at $t = kT_s$

(b)
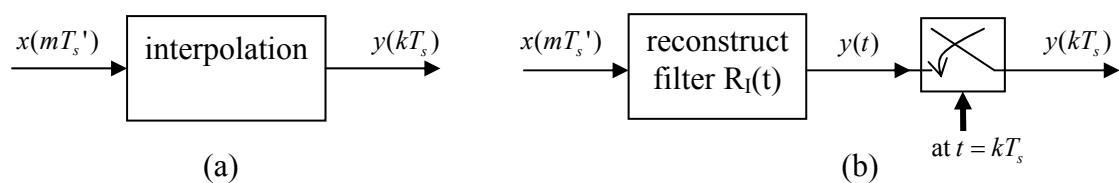
Figure 4-9 resample block diagram (a) a concept diagram (b) an equivalent model

The time-continuous output of the reconstruct filter is

$$y(t) = \sum_m x(mT_s')R_I(t) \qquad (4.32)$$

Then resample y(t) at time instants $t = kT_s$ and will get new samples represented by

$$y(kT_s) = \sum_m x(mT_s')R_I(kT_s - mT_s') \qquad (4.33)$$

Recognizing that m is a signal index, define a filter index

$$i = \text{int}[\frac{kT_s}{T_s'}] - m \qquad (4.34)$$

where int[x] means largest integer not exceeding x. In addition, define a basepoint index

$$m_k = \text{int}[\frac{kT_s}{T_s'}] \qquad (4.35)$$

and a fractional interval

$$\mu_k = \text{int}[\frac{kT_s}{T_s'}] - m_k \qquad (4.36)$$
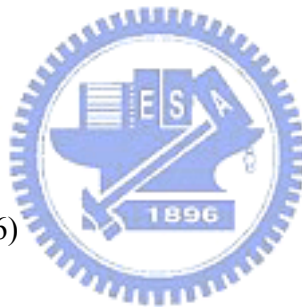
where $0 \le \mu_k < 1$. Timing relations among theses indices are illustrated in Figure 4-10.
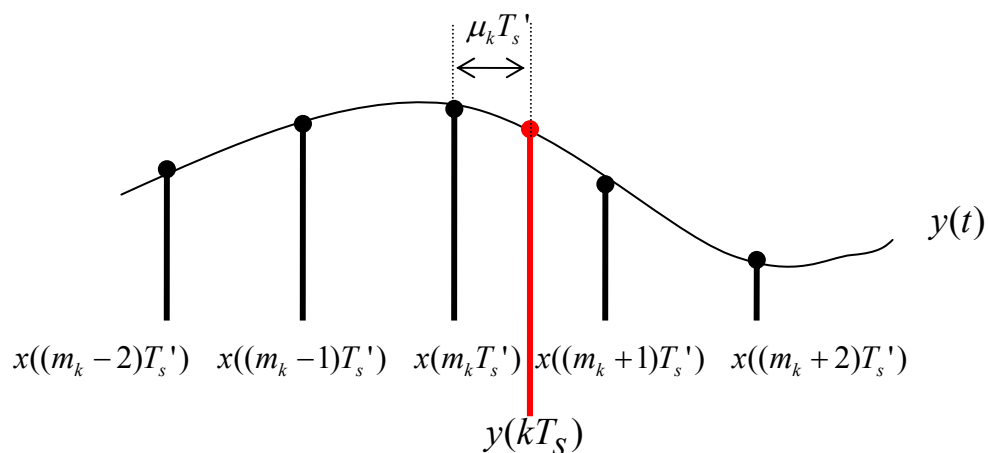
Figure 4-10 relation of timing indices for resample

by index replacing, function arguments in equation (4.33) become $m = m_k - I$ and $(kT_s - mT_s') = (I + \mu_k) T_s'$, and the resampling instant $kT_s = (m_k + \mu_k) T_s'$ so that the equation can be rewritten as

$$y(kT_s) = y[(m_k + \mu_k)T_s']$$

$$= \sum_i x((m_k - i)T_s')R_I((i + \mu_k)T_s') \qquad (4.37)$$

It is well known that the bandlimited input signal x(t) could be recovered from its samples $\{x(m\ T_s')\}$ by the ideal reconstruct filter with impulse response

$$R_I(t) = \sin c(\frac{t}{T_s'}) \qquad (4.38)$$

where $sinc(x) = sin(\pi x)/\pi x$. Accordingly, equation (4.37) becomes

$$y(kT_s) = \sum_{i=-\infty}^{\infty} x((m_k - i)T_s')\sin c(i + \mu_k) \qquad (4.39)$$

The sinc filter is IIR and noncausal and cannot be realized with any practical filter so that truncation for the sinc filter is needed for practice. Denote the truncated window size is $2 \cdot I + 1$ so that the reconstructed signal by windowed sinc filter is

$$y(kT_s) = \sum_{i=-I}^{I} x((m_k - i)T_s')\sin c(i + \mu_k) \qquad (4.40)$$

However, the window of sinc filter usually needs very large size for better accurate of interpolation with sinc function. The computation is so complex that it is not feasible for implement. For this reason, we consider other methods for interpolation. In following sections, we present two popular polynomial-based interpolations: Lagrange interpolation and B-spline interpolation.

4.5.1   Lagrange Interpolation

Lagrange interpolation is one of popular architecture for resampling data presently. In this section, we introduce the method of Lagrange interpolation and display the structure of cubic Lagrange interpolation which is with an order of three and used frequently for implement.

For an interpolation problem, supposing that we receive N+1 data points, we can find the unique polynomial of order N which passes through the given points by solving the simultaneous equations. If the polynomial is

$$p(x) = c_0 + c_1 x + c_2 x^2 + \cdots + c_N x^N \qquad (4.41)$$

Assume that the kth data point has the location $(x_k, p(k))$. The N+1 data points must passes through the polynomial so that

$$\begin{bmatrix} 1 & x_0 & x_0^2 & \cdots & x_0^N \\ 1 & x_1 & x_1^2 & \cdots & x_1^N \\ \vdots & \vdots & \vdots & \ddots & \vdots \\ 1 & x_N & x_N^2 & \cdots & x_N^N \end{bmatrix} \begin{bmatrix} c_0 \\ c_1 \\ \vdots \\ c_N \end{bmatrix} = \begin{bmatrix} p(k_0) \\ p(k_1) \\ \vdots \\ p(k_N) \end{bmatrix} \qquad (4.42)$$

However, for a large number of data points, the computation is very complex and the resultant high-order polynomial may oscillate widely between the data points. Lagrange interpolation divides the range of data points into a number of sub-intervals. Therefore, we can use low-order polynomial to interpolate the data within this sub-interval. In general, an nth order Lagrange interpolation involves n+1 data points. The general form of an nth order Lagrange interpolation polynomial with n+1 basepoints is:

$$\phi^n(x) = \sum_{i=I_1}^{I_2} \lambda_i(x) p(I_1 + I_2 - i) \qquad (4.43)$$

where

$$\lambda_i(x) = \prod_{j=I_1, j \neq i}^{I_2} \frac{x - x_j}{x_i - x_j} \qquad (4.44)$$

For odd value of n, the limits are set to $I_1 = -(n+1)/2$ and $I_2 = (n+1)/2 - 1$, respectively. A interpolated point with a interpolated distance, d, where $0 \leq d < 1$, can be written from equation (4.43) as

$$\phi^n(d) = \sum_{i=I_1}^{I_2} \lambda_i(d) p(I_1 + I_2 - i) \qquad (4.45)$$

Cubic Lagrange interpolation (i.e. n = 3) is popular due to its simple complexity, and it has interpolation polynomial:

$$\phi^3(d) = \sum_{i=-2}^{1} \lambda_i(d) p(-1-i) \qquad (4.46)$$

From equation (4.46), however, the argument of λ function is the interpolation distance d. This means the coefficients of λ function for the interpolation filter must re-calculate as d changes. For a tracking scheme for clock synchronization, the interpolation distance may be changed all the time before reaching to steady state so the structure of equation (4.45) is not acceptable for realistic implement because it needs much computation complexity to calculate samples of λ function for every interpolated point. Here we use an efficient method, Farrow structure [22], to remove this problem.

The technique of Farrow structure is to decompose a polynomial function as a power series form. In this way, for cubic Lagrange interpolator, from equation (4.44) we have

$$\lambda_{-2}(d) = \frac{1}{6}d^3 - \frac{1}{6}d$$

$$\lambda_{-1}(d) = -\frac{1}{2}d^3 + \frac{1}{2}d^2 + d$$

$$\lambda_0(d) = \frac{1}{2}d^3 - d^2 - \frac{1}{2}d + 1 \qquad\qquad (4.47)$$

$$\lambda_1(d) = -\frac{1}{6}d^3 + \frac{1}{2}d^2 - \frac{1}{3}d$$

so that we can get the structure of cubic Lagrange interpolator with Farrow structure shown in Figure 4-11. For more detail about Lagrange interpolator, see [23].
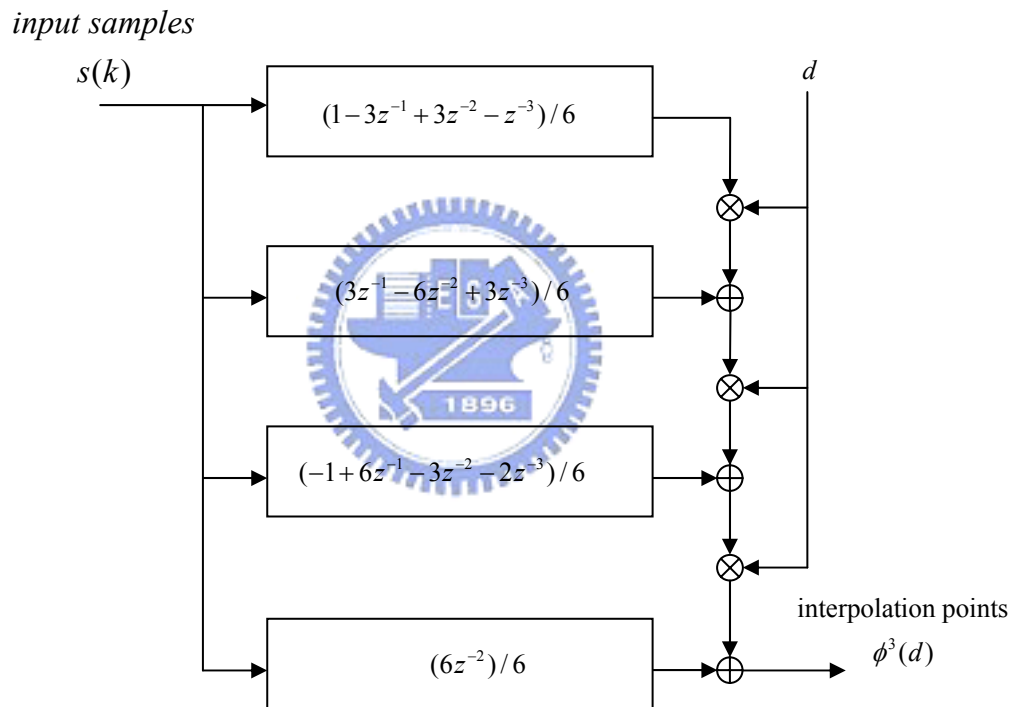
Figure 4-11 the structure of cubic Lagrange interpolator with Farrow structure

4.5.2　B-spline Interpolation

Splines are piecewise polynomials and each piece is smoothly connected to adjacent ones. The joining points of the polynomial pieces are called knots. Knots may not space evenly. A spline is of degree n when each segment of that is a

polynomial of degree n. Splines are widely used in signal interpolation, image process, and computer graphics. Among these splines, there is a very special class of piecewise polynomials, namely B-splines, which is first proposed by Schoenberg in 1946 [24], because all other polynomial splines can be obtained as a linear combination of shifted B-splines [25].

● **Basic Principle of B-spline**

Define a subspace S_n as that all continuous piecewise polynomial functions of degree n with derivatives up to order n-1 that are continuous everywhere on the real line. The action of B-splines is to provide a basis of S_n. It is natural that signals in digital signal processing are almost represented in the form of uniformly spaced samples thus we consider the condition that knots are unit spaced uniformly here. As a result, any function $\varphi_n(x)$ contained in S_n can be represented as [26]

$$\phi^n(x) = \sum_{i=-\infty}^{\infty} c(i)\beta^n(x-i) \qquad (4.48)$$

where $\beta^n(x)$ is the B-spline of order n

$$\beta^n(x) = \sum_{j=0}^{n+1} \frac{(-1)^j}{n!}\binom{n+1}{j}(x+\frac{n+1}{2}-j)^n \cdot \mu(x+\frac{n+1}{2}-j) \qquad (4.49)$$

where $\mu(x)$ is the unit step function

$$\mu(x) = \begin{cases} 0, & x < 0 \\ 1, & x \geq 0 \end{cases} \qquad (4.50)$$

and $\binom{n+1}{j}$ are the binomial coefficients

$$\binom{n+1}{j} = \frac{(n+1)!}{(n+1-j)!\,j!} \qquad (4.51)$$

and $\{c(i)\}$ are the B-spline coefficients produced by input data and will be stated later.

Equation (4.48) tells us that any polynomial spline $\varphi_n(x)$ in S_n can be written from a weighted sum of shifted B-spline and is uniquely determined by its spline coefficients $\{c(i)\}$. Latter, we will use this property to reconstruct the signal and interpolate the desired points.

We now introduce several of the properties of polynomial splines. First, the convolution property : a B-spline of order n can be generated by convolving one of order n-1 and other of order zero or convolving one of order zero n+1 times with itself :

$$\beta^n(x) = \beta^{n-1} * \beta^0(x) = \underbrace{\beta^0 * \beta^0 * \cdots * \beta^0(x)}_{(n+1)} \qquad (4.52)$$

where * denote the convolution operation. Figure 4-12 shows graph of B-splines of order 0, 1, 2, and 3 and their convolving relation.
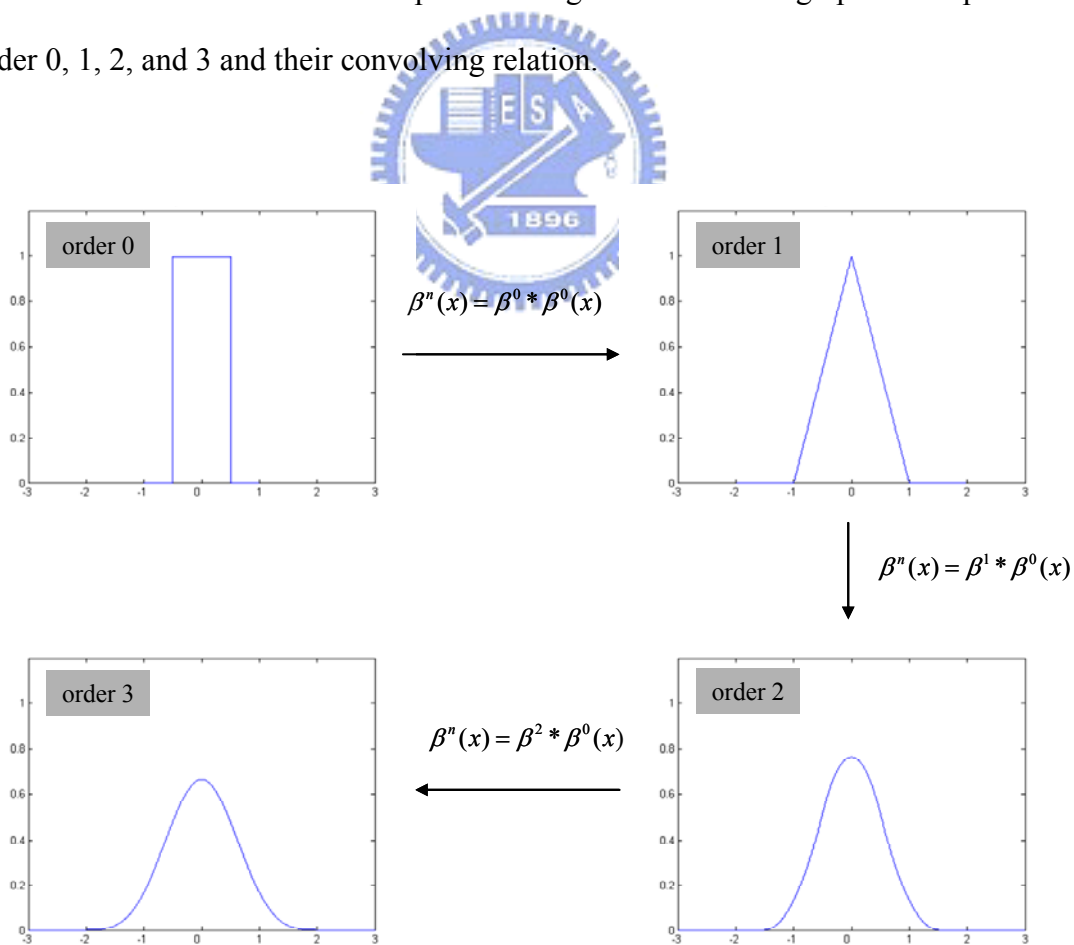
Figure 4-12 convolving relation among B-splines with order 0~3

Second, from the definition of B-spline, we can derive the property of recursion:

$$\beta^n(x) = \frac{(\frac{n+1}{2} + x)\beta^{n-1}(x + \frac{1}{2}) + (\frac{n+1}{2} - x)\beta^{n-1}(x - \frac{1}{2})}{n} \quad (4.53)$$

which states B-spline of order n can be constructed recursively with B-splines of lower orders recursively. With the recursive property, we can also show the differential property of B-spline as

$$\frac{\partial \beta^n(x)}{\partial x} = \beta^{n-1}(x + \frac{1}{2}) - \beta^{n-1}(x - \frac{1}{2}) \quad (4.54)$$

In order to have efficient algorithms for representing discrete signals with B-spline, we then investigate the properties of discrete B-spline which is obtained by sampling continuous spline functions.

Define discrete B-splines as samples of continuous B-splines

$$b^n(k) \equiv \beta^n(k) = \sum_{j=0}^{n+1} \frac{(-1)^j}{n!} \binom{n+1}{j} (k + \frac{n+1}{2} - j)^n \cdot \mu(k + \frac{n+1}{2} - j) \quad (4.55)$$

The discrete B-splines of order 0~3 are illustrated in Figure 4-13. As a result, their z-transform, $B^n(z)$ defined as

$$B^n(z) \equiv \sum_{k=-\infty}^{\infty} b^n(k) \cdot z^{-k} \quad (4.56)$$

can be calculated and are listed for n=0 to 5 in Table 4-1.
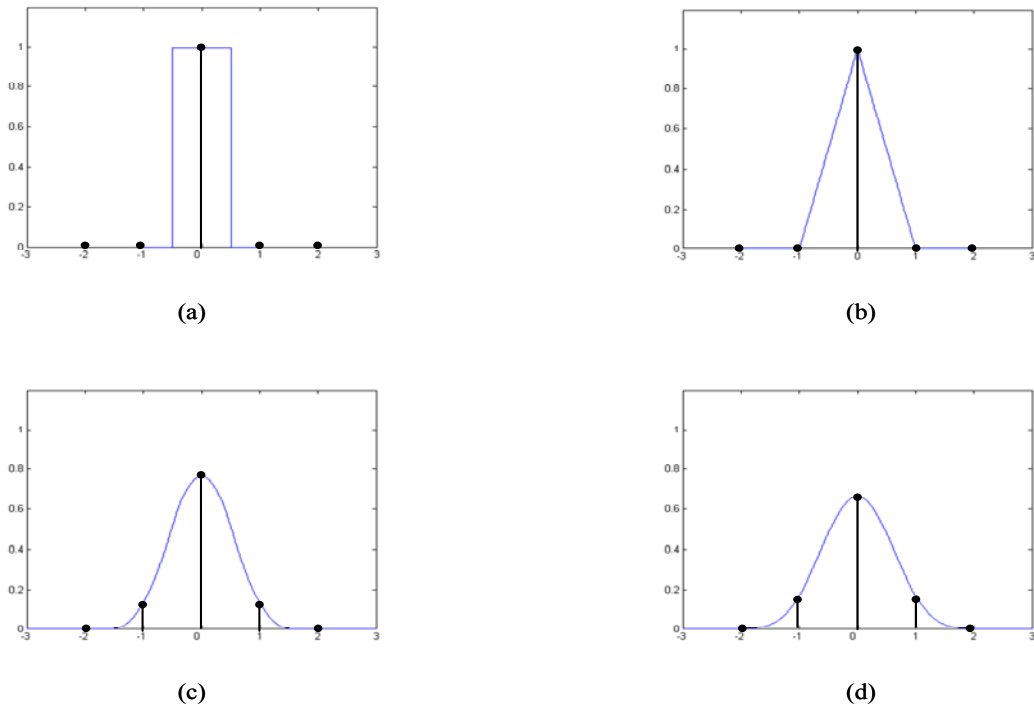
Figure 4-13 discrete B-splines of (a) order 0 (b) order 1 (c) order 2 (d) order 3

n	$B^n(z)$	$\Gamma^n(z)$
0	1	1
1	1	$\dfrac{z+1}{2}$
2	$\dfrac{z+6+z^{-1}}{8}$	$\dfrac{z+1}{2}$
3	$\dfrac{z+4+z^{-1}}{6}$	$(\dfrac{z+1}{2})(\dfrac{z+22+z^{-1}}{24})$
4	$\dfrac{z^2+76z+230+76z^{-1}+z^{-2}}{384}$	$(\dfrac{z+1}{2})(\dfrac{z+10+z^{-1}}{12})$
5	$\dfrac{z^2+26z+66+26z^{-1}+z^{-2}}{120}$	$(\dfrac{z+1}{2})(\dfrac{z^2+236z+1446+236z^{-1}+z^{-2}}{1920})$

Table 4-1 z transforms of discrete B-spline and its shift version

● Differential Processing using B-spline

In section 4-4, we use B-spline to calculate the derivation of data. Here the process how to get the differentiation in Figure 4-7 is present.

The derivative of a signal is formally obtained by differentiating its continuous B-spline representation:

$$\frac{\partial \phi^n(x)}{\partial x} = \sum_{i=-\infty}^{\infty} c(i) \frac{\partial \beta^n(x-i)}{\partial x} \qquad (4.57)$$

Utilizing the differential property of B-spline in equation (4.54), we can get

$$\frac{\partial \phi^n(x)}{\partial x} = \sum_{i=-\infty}^{\infty} c(i)\{\beta^{n-1}(x-i+\frac{1}{2}) - \beta^{n-1}(x-i-\frac{1}{2})\}$$

$$= \sum_{i=-\infty}^{\infty} \{c(i) * (\delta(i) - \delta(i-1))\}\beta^{n-1}(x-i+\frac{1}{2}) \qquad (4.58)$$

Define the shift version of B-spline as $\gamma^n(x)$:

$$\gamma^n(x) \equiv \beta^n(x+\frac{1}{2}) \qquad (4.59)$$
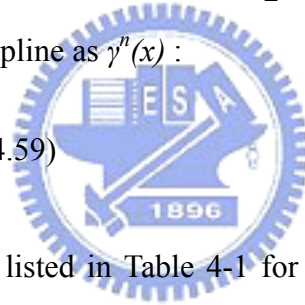
which has z-transforms $\Gamma^n(z)$ listed in Table 4-1 for n = 0 to 5 and equation (4.58) changes to

$$\frac{\partial \phi^n(x)}{\partial x} = \sum_{i=-\infty}^{\infty} \{c(i) * (\delta(i) - \delta(i-1))\}\gamma^{n-1}(x-i) \qquad (4.60)$$

From equation (4.60), we can use a combinational filter structure shown in Figure 4-7 to compute the first order derivation of data. Furthermore, we can also obtain the second order derivation by differentiating the first order derivation. For a polynomial in the subset of S_n, we can compute derivation of orders up to n-1 with the same way.

● B-spline Coefficients

Consider discrete signals $\{s(k)\}$, k = -∞,…, ∞, for interpolating from $\{s(k)\}$ we must find a polynomial representing the continuous waveform of $\{s(k)\}$ by equation

(4.48) under the constrain of

$$\phi^n(x)\,|_{x=k} = \sum_{i=-\infty}^{\infty} c(i)b^n(k-i) = s(k), \quad k = -\infty,...,\infty \qquad (4.61)$$

That is, the polynomial must match to the original sampling points at their corresponding positions. The constrain gives

$$s(k) = b^n * c(k) \qquad (4.62)$$

which has the z-transform

$$S(z) = B^n(z)C(z) \qquad (4.63)$$

where $S(z)$, $B^n(z)$, and $C(z)$ are the z-transforms of $s(k)$, $b^n(k)$, and $c(k)$I respectively. Consequently, we can determined the B-spline coefficients $\{c(k)\}$ simply by a inverse filter of B-spline, $B^n(z)^{-1}$

$$C(z) = B^n(z)^{-1} S(z) \qquad (4.64)$$
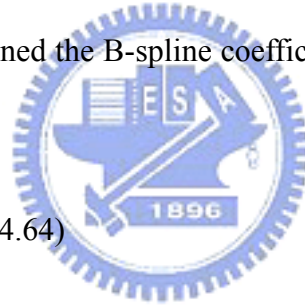
where

$$B^n(z)^{-1} = \frac{1}{\displaystyle\sum_{k=-\infty}^{\infty} b^n(k)z^{-k}} \qquad (4.65)$$

The operation of computation for B-spline coefficients is called "direct transform" and $B^n(z)^{-1}$ is also called "prefilter" shown in Figure 4-14. More details about the prefilter are introduced latter in the subsection "FIR approximations of the prefilter".

input samples $s(k)$ → | prefilter $B^n(z)^{-1}$ | → B-spline coefficients $c(k)$
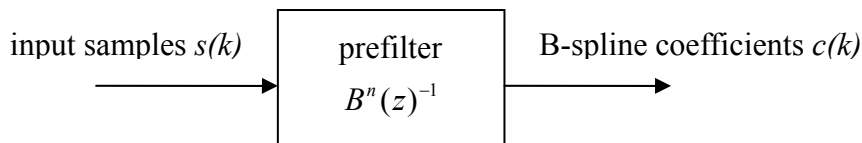
Figure 4-14 direct transform of B-spline

● **Interpolation Architecture with Farrow Structure**

A interpolated point away from the kth sample by a interpolated distance, d, where $0 \leq d < 1$, can be written from equation (4.48) as

$$\phi^n(x)|_{x=k+d} = \phi^n(k+d) = \sum_{i=-\infty}^{\infty} c(i)\beta^n(k+d-i) \qquad (4.66)$$

Here we take a parameter replacing for convenience of expression; let $k' = k-i$ and equation (4.66) changes to

$$\phi^n(k+d) = \sum_{k'=-\infty}^{\infty} c(k-k')\beta^n(k'+d) \qquad (4.67)$$

which has the index k' from $-\infty$ to ∞. However, from the definition of B-spline, its discrete samples are not zeros only for certain points range from $-K_1$ to K_2 hence:

$$\phi^n(k+d) = \sum_{k'=-K_1}^{K_2} c(k-k')\beta^n(k'+d) \qquad (4.68)$$

where $K_1 = [n/2] + 1$ and $K_2 = [n/2]$. For example, as showed in Figure 4-15, $[K_1\ K_2]$ is equal to $[1\ 0]$ and $[2\ 1]$ for B-spline of order $n = 1$ and $n = 3$ respectively. Therefore, we can get the digital structure of interpolation in Figure 4-16.

(a)   (b)
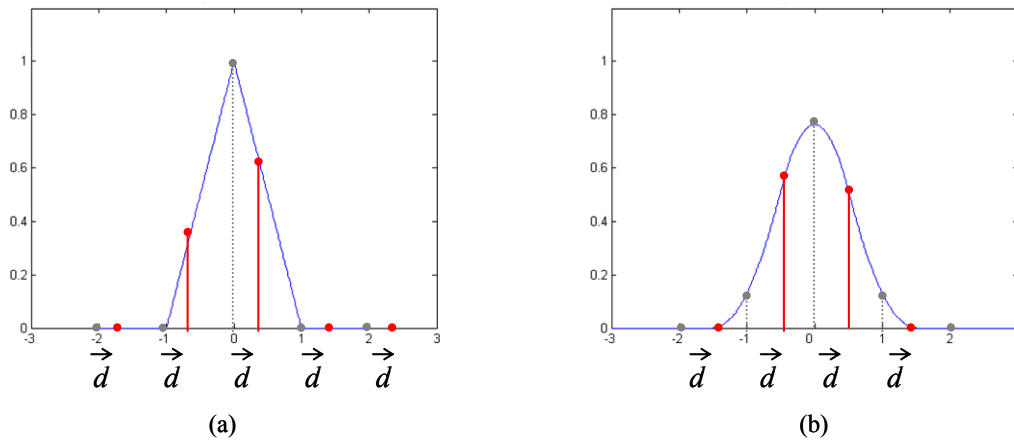
Figure 4-15 discrete B-spline samples with an interpolation distance d
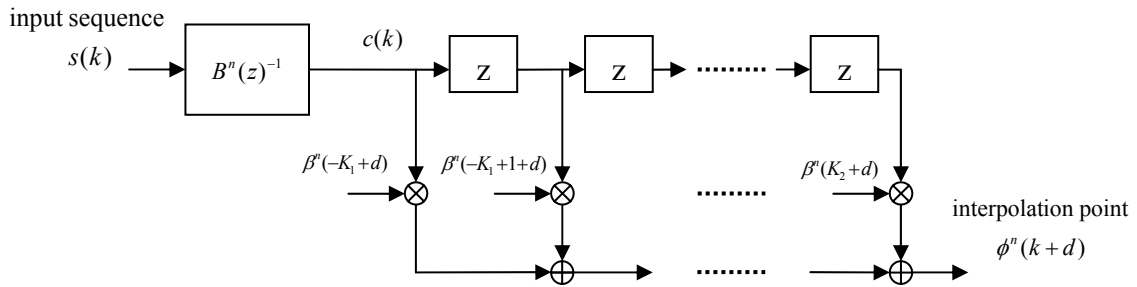
Figure 4-16 the structure of B-spline interpolation

For Farrow structure, we rewrite $\beta^n(k'+d)$ as

$$\beta^n(k'+d) = \sum_{p=0}^{n} a_p(k') \cdot d^p \qquad (4.69)$$

where

$$a_p(k') = \sum_{j=0}^{n+1} \frac{(-1)^j}{n!} \binom{n+1}{j}\binom{n}{p}(k'+\frac{n+1}{2}-j)^{n-p} \mu(k'+\frac{n+1}{2}-j) \qquad (4.70)$$

which is fixed coefficients for the chosen order n.

Substituting equation (4.70) into equation (4.69) , we get

$$\phi^n(k+d) = \sum_{k'=-K_1}^{K_2} c(k-k')(\sum_{p=0}^{n} a_p(k') \cdot d^p) \qquad (4.71)$$

The structure of interpolation with Farrow structure is showed in Figure 4-17. In the filter structure, the filter coefficients are unconcerned with the interpolation distance and can be calculated off-line; for different interpolated point, all we need to do is changing the multiplier, interpolation distance d.
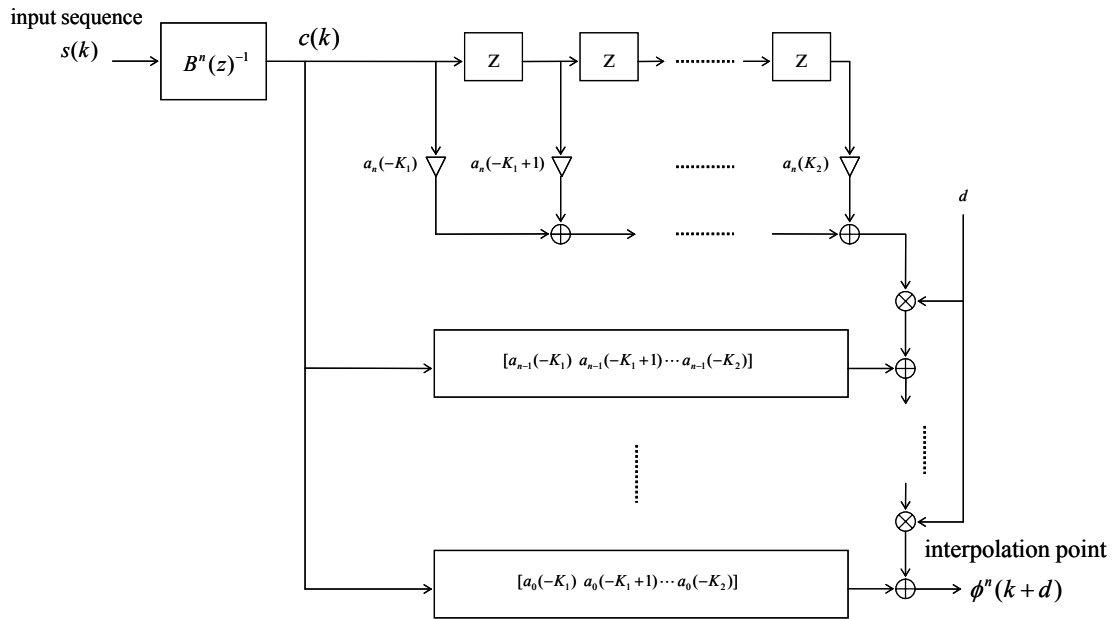
Figure 4-17 the structure of B-spline interpolation with Farrow structure

- **Cubic B-spline Interpolation**

    For cubic B-spline, substituting n = 3 into equation (4.71), we get the coefficients

of interpolator:

$$\phi^3(k+d) = \sum_{k'=-2}^{1} c(k-k')(\sum_{p=0}^{3} a_p(k') \cdot d^p) \qquad (4.72)$$

where $a_p \equiv [a_p(-2)\ a_p(-1)\ a_p(0)\ a_p(1)]$, p = 0,1,2,3 are

$$\begin{bmatrix} a_0 \\ a_1 \\ a_2 \\ a_3 \end{bmatrix} = \frac{1}{6} \begin{bmatrix} 0 & 1 & 4 & 1 \\ 0 & 3 & 0 & -3 \\ 0 & 3 & -6 & 3 \\ 1 & -3 & 3 & -1 \end{bmatrix} \qquad (4.73)$$

and from Table 4-1, $B^3(z)^{-1}$ can be obtained as

$$B^3(z)^{-1} = \frac{6}{z + 4 + z^{-1}} \qquad (4.74)$$

Therefore, the structure of cubic B-spline interpolator can be obtained as shown in

Figure 4-18. Since the coefficients of filters in the structure of interpolator are all constant, multiplication operation can be replaced by summation of several shift-and-addition operations. Only three multiplications for the interpolation distance d and several additions are needed for one resampled data.
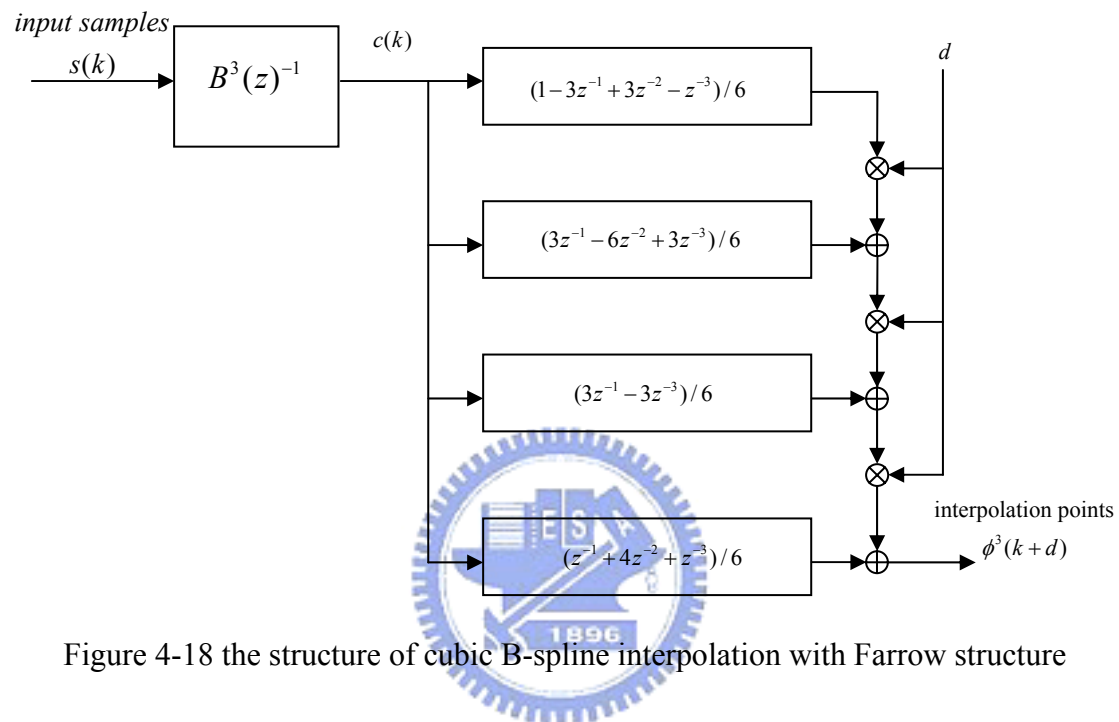
Figure 4-18 the structure of cubic B-spline interpolation with Farrow structure

● **FIR approximations of the prefilter**

From Table 4-1, the prefilter, the inverse filter of B-spline has an infinite impulse response (IIR) which may lead to instabilities and limit cycles. To avoid such problems, we may truncate the IIR filter to a FIR filter directly. However, direct truncation gives rise to large truncation error and needs large tap number of the truncated filter to reduce the error. For the efficient design of prefilters, we may use some criterion to reduce the truncation error of a short prefilter. Suppose $P_N(e^{j\omega})$ is the frequency response of the truncated prefilter, $H_d(e^{j\omega})$ is the frequency response from the B-spline coefficient end to the B-spline interpolation outputs in Figure 4-17, and $R_W(e^{j\omega})$ is the ideal low pass filter with a cut-off frequency of W. For the input signal

that with a bandwidth of W, our criterion for the truncated prefilter is to minimize the

error: $\int_{d=0}^{1}\int_{\omega=0}^{W}|P_N(e^{j\omega})H_d(e^{j\omega})-R_W(e^{j\omega})|^2 \, d\omega dd$. For simplicity, here we use an FIR

filter derived from the LMS-based algorithm [32] for *off-line* approximation of the

prefilter that needs only a few of filter taps to replace the criterion above. Figure 4-19

describes the structure for LMS-based FIR prefilter where $H_d(z)$ is the response from

the B-spline coefficient end to the B-spline interpolation outputs in Figure 4-17. The

error signal of LMS e(n) is the difference between the interpolation outputs by

B-spline and the correct interpolation points. Suppose that the desired FIR prefilter

has the coefficients **c**: $\{c_0, c_1, \ldots, c_{N-1}\}$ where N is the tap number of the prefilter, the

iterative equation for each coefficient of the prefilter is

$$c_k(n+1) = c_k(n) + \mu \cdot e(n) \cdot y(n-k), \quad k = 0,1,\ldots,N-1 \qquad (4.75)$$

where μ is the step size of the algorithm.
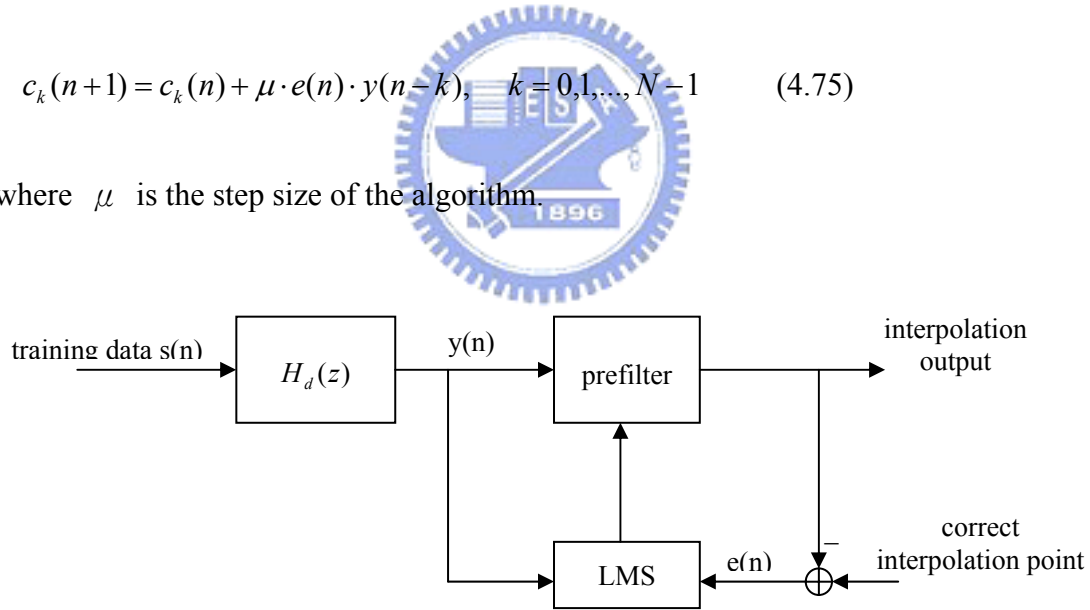
Figure 4-19 the structure for LMS-based FIR prefilter

4.6 Simulation Results and Analysis

In this section, we give the simulation results of Lagrange and B-spline

interpolators and the pre-/post-FFT SCED. First, we compare the performance of

Lagrange and B-spline of order three and five interpolators at different oversampling rate of ADC. Then, we present the comparison of the tracking ability between our proposed pre-FFT and traditional post-FFT SCED at different mobile velocities.

4.6.1　Cubic Lagrange and B-spline Interpolator

● **Simulation parameters**

The performance of Lagrange and B-spline interpolators highly concern with signal bandwidth. When signal varies rapidly, there is significant error caused by the interpolator. In such case, oversampling at ADC is needed for a good interpolation performance. For DVB-T with 8MHz channel, signal bandwidth is 7.61MHz while the sampling frequency of ADC without oversampling is 9.14 MHz.

The simulation platform for comparison of B-spline and Lagrange interpolators is shown in Figure 4-20. For emulation of ADC with oversampling rate R, we use a sinc filter with I = 4096 (i.e. 8193 taps totally) to resample input data at a frequency of R*9.14 MHz. Then, we plan to interpolate new points with a new sampling period $T_s(1+\Delta)$, where Ts is the sampling period of input data. That is, resample input data with sampling instants { $T_s(1+\Delta)$, $2T_s(1+\Delta)$, $3T_s(1+\Delta)$, … } by B-spline and Lagrange interpolators. In the following simulation, we choose $\Delta = 100$ ppm. Here, again, we use the interpolated points by sinc filter with I = 4096, $x_c(k)$, as the correct resampled data. To evaluate the performance of interpolators, we define a parameter SER (Signal-to-Error-Ratio)

$$SER \equiv \frac{\text{power of } x_c(k)}{\text{power of } e(k)} \qquad (4.76)$$

where e(k) is the difference between the correct sample and interpolated sample. For

cubic B-spline and Lagrange interpolator, as shown in Figure 4-20, e(k) is $e_B(k)$ and $e_L(k)$, respectively.

For B-spline interpolation, the prefilter $B^n(z)^{-1}$ is a noncausal IIR filter. Here, we first compare two approximated FIR prefilters; one is the prefilter which is truncated directly to an N-tap FIR filter and the other is the LMS-based prefilter which is obtained by the structure in Figure 4-19. For the consideration of hardware complexity of ADC, we get the LMS-based prefilters that are under the condition of **double oversampling rate of ADC**. After that, we present the comparison of SER performance of cubic and 5th-order B-spline and Lagrange interpolators.
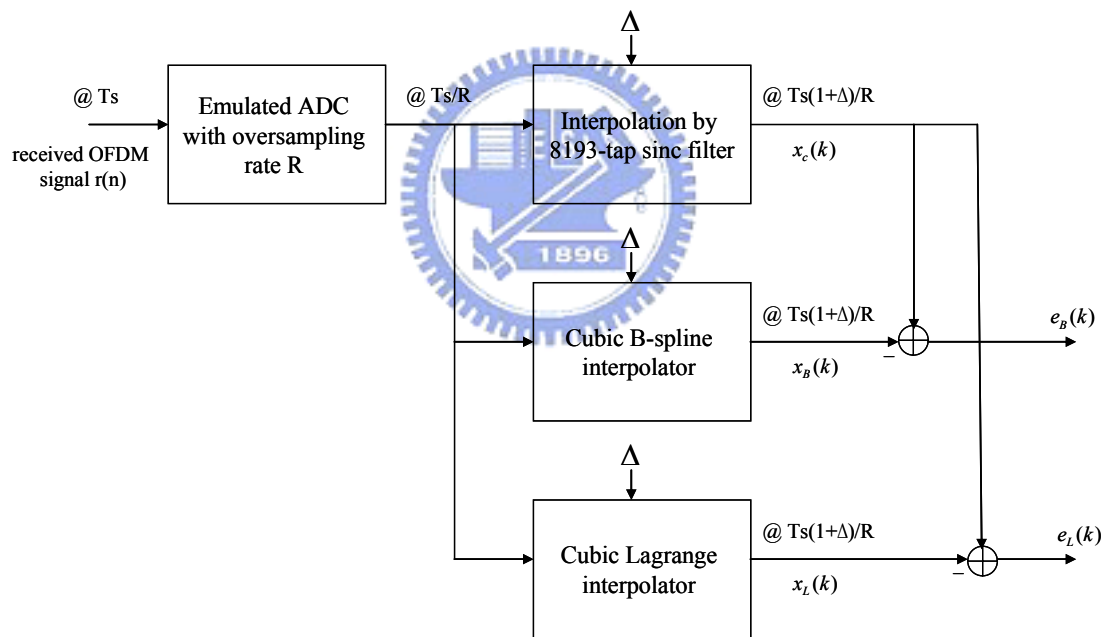
Figure 4-20 simulation model for comparison of cubic B-spline and Lagrange interpolators

● **Simulation results**

With the setting of simulation parameters above, Figure 4-21 shows the SER performance of B-spline interpolators with different length of prefilters. From

observation, without oversampling, the SER are all fewer than 20 dB which is impossible performance for implement. Suppose setting the oversampling rate of ADC as two, for cubic B-spline interpolator, the direct- truncated prefilter needs at least nine taps for a SER of 45 dB in Figure 4-21 (a) while the LMS-based prefilter needs only five taps for a SER of 45 dB in Figure 4-21 (b); for 5th-order B-spline interpolator, the direct- truncated prefilter needs at least 21 taps for a SER excess of 60 dB in Figure 4-21 (c) while the LMS-based prefilter needs only 11 taps for a SER excess of 60 dB in Figure 4-21 (d). Evidently, using the LMS-based prefilter is more efficient for hardware complexity.
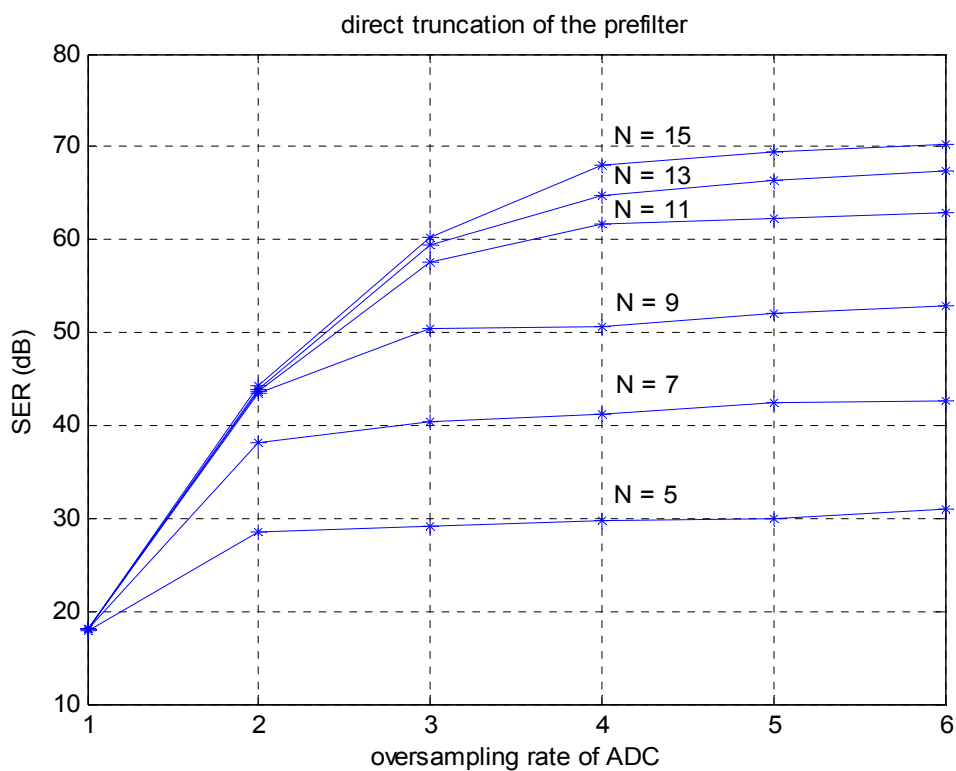
Figure 4-21 (a) SER performance of **cubic** B-spline interpolator with an N-tap direct-truncated prefilter
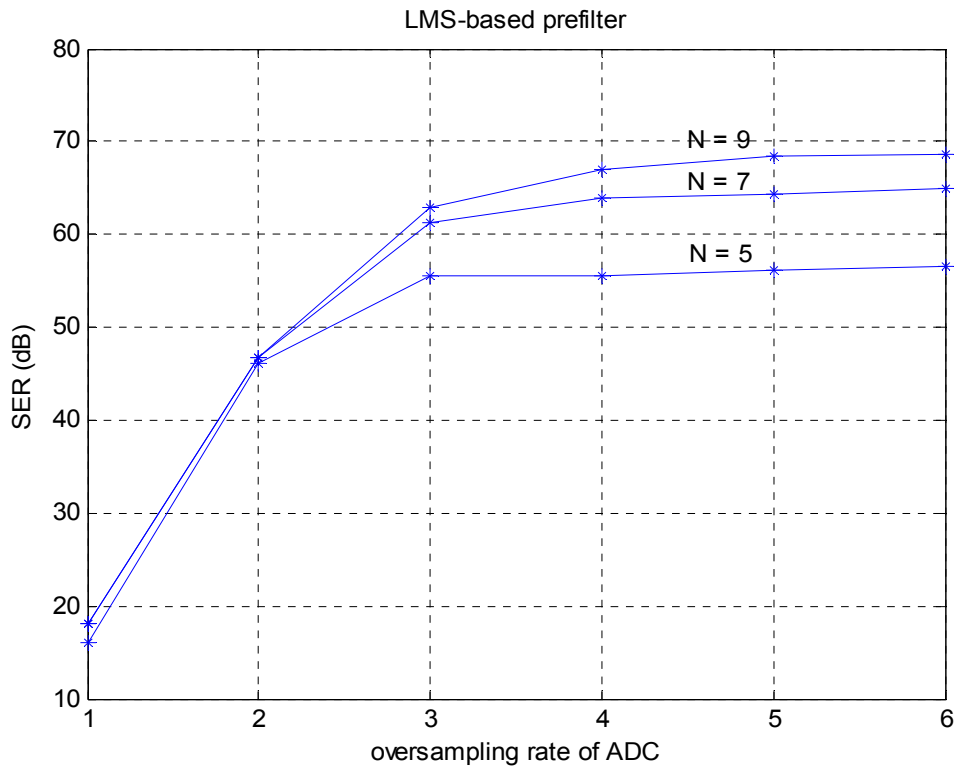
Figure 4-21 (b) SER performance of **cubic** B-spline interpolator with an N-tap
LMS-based prefilter
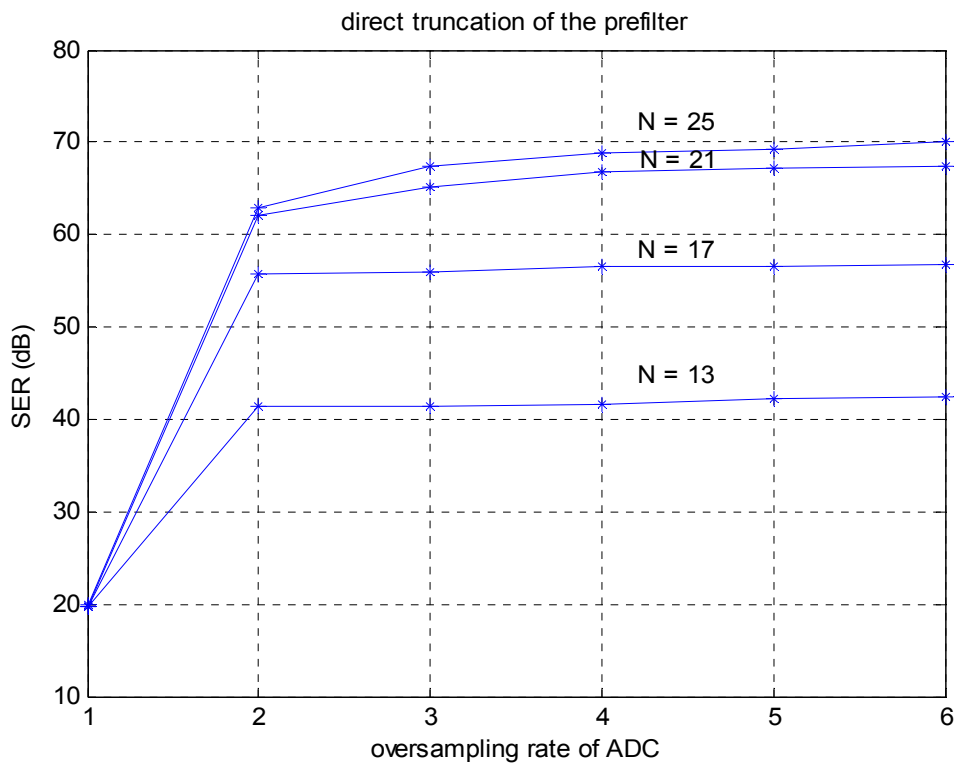
Figure 4-21 (c) SER performance of **5th-order** B-spline interpolator with an N-tap
direct-truncated prefilter
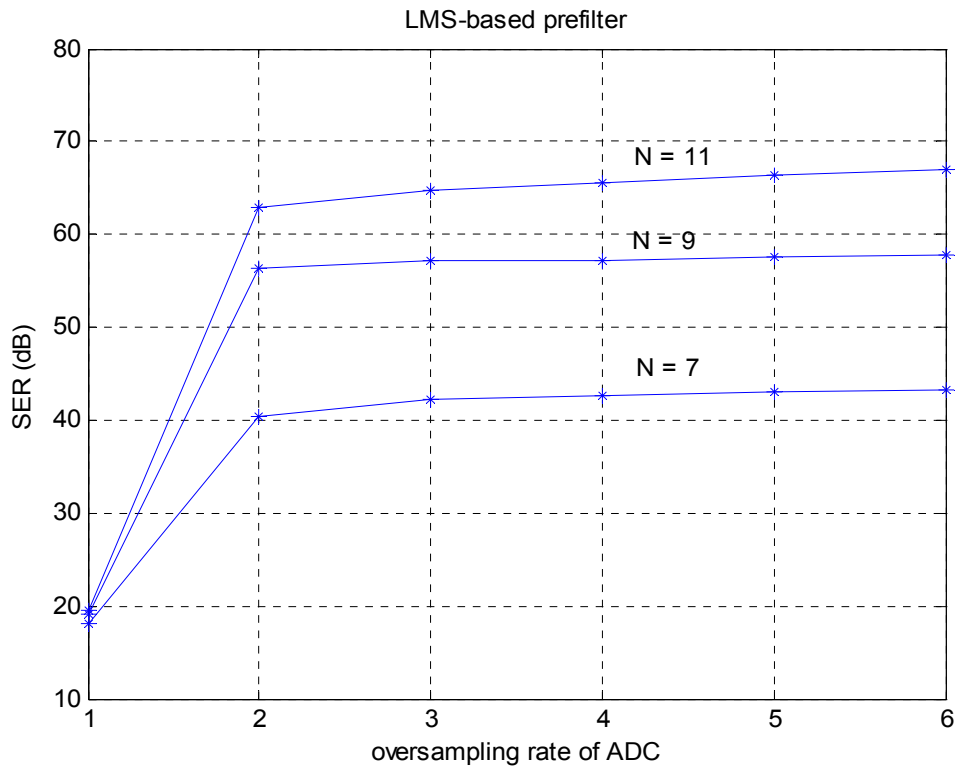
Figure 4-21 (d) SER performance of **5th-order** B-spline interpolator with an N-tap
LMS-based prefilter

Comparing with general polynomial-based interpolation algorithms, B-spline
interpolation has the extra component, the prefilter. However, the coefficients of the
prefilter are fixed number and have the symmetric property hence multipliers are not
needed and we can use only some additions to implement the prefilters. Therefore, the
hardware complexity of the prefilter is very low and can be neglected under the
comparison with the part of Farrow structure which needs order-number multipliers.

Figure 4-22 shows the SER performance comparison of cubic and 5th-order B-spline
and Lagrange interpolators. In the comparison, we choose **9-tap and 11-tap**
LMS-based FIR prefilters for **cubic and 5th-order** B-spline interpolators,
respectively. Under the double oversampling rate of ADC, no matter with order three
or five, the Lagrange interpolator has SER that is no excess of 40 dB. In the other
hand, the B-spline interpolator has SER of 46 dB and 62 dB when the order is three

and five, respectively. Under the ADC oversampling of four, the cubic Lagrange interpolator has a SER of 52 dB while other three cases all have SER excess of 60 dB.

Since the complexity of ADC is increased as the sampling frequency, under the consideration of hardware complexity, we determine to select the double oversampling rate as our ADC sampling rate. From the simulation, at double oversampling rate, the **cubic B-spline interpolator** with **5-tap LMS-based prefilter** has the SER performance of 46 dB which is high enough for general systems. For the demand of SER of 60 dB, we can select the scheme of the **5th-order B-spline** interpolator with **11-tap LMS-based prefilter**.
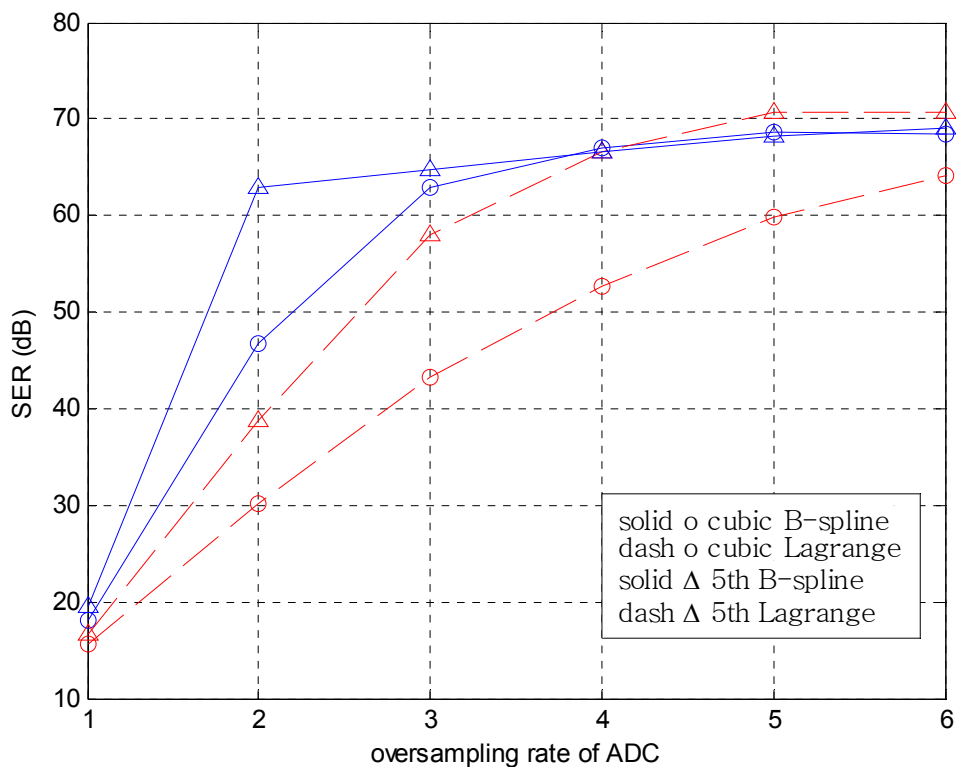
Figure 4-22 (d) SER performance comparison of **cubic** and **5th-order** B-spline interpolators

4.6.2   Performance of Sampling Clock Synchronization

● **Simulation parameters**

In this section, we show and compare the tracking performance of SCED with our proposed pre-FFT and traditional post-FFT algorithm. In our simulation for clock synchronization, we set the relative parameters as listed in Table 4-2. Here, we assume that carrier offset is zero and perfect symbol boundary estimation. From section 4.6.1, for the compromise between hardware complexity and performance, we select double ADC sampling rate and cubic B-spline interpolator with 5-tap prefilter for our digital resampling scheme. In addition, in our close loop for clock synchronization, we use a second order loop filter with transfer function:

$$F(z) = K_0 + K_1 \frac{z}{z-1} \qquad (4.77)$$

to alleviate noise interference. At the beginning of tracking, we use the loop filter with larger parameters to speed up the track; after several iterations, there is only slight offset remaining, thus we turn the parameters to a set of smaller one for reducing the noise further more.
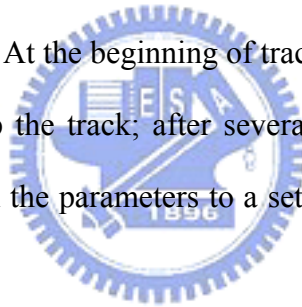
system	DVB-T
transmission mode	2K
channel bandwidth	8MHz
CP mode	1/8
modulation	QPSK
channel model	HT in COST207
mobile velocity	0, 100, 200, 300 km/hr
carrier frequency offset	0 ppm
sampling clock offset	100 ppm

A/D oversampling rate	2 (i.e. 18.28MHz)
digital resampler	cubic B-spline interpolator with 5-tap prefilter
loop filter parameter [K_0,K_1]	[0.015,0.005], [0.004, 0.0016]
SCED	proposed pre-FFT / post-FFT algorithm

Table 4-2 simulation parameters for clock synchronization

Figure 4-23 shows the simulation block diagram. For simulation of ADC with double oversampling rate, we upsample the sampling rate at the transmittor with a square-root raised cosine FIR with roll-over factor of 0.1. At receiver, the received double-rate samples after channel are delivered into the digital RX filter which has the same structure of digital TX filter. Then, we simulate the effect of sampling clock offset by an 8193-tap sinc filter like in section 4.6.1. That is, the interpolator resamples original received samples with a period of $T_s/2$ to new samples that has a new period of $T_s(1+t_\Delta)/2$. The received oversampled data with the effect of clock offset are then delivered to the close loop for clock synchronization as shown in Figure 4-23.
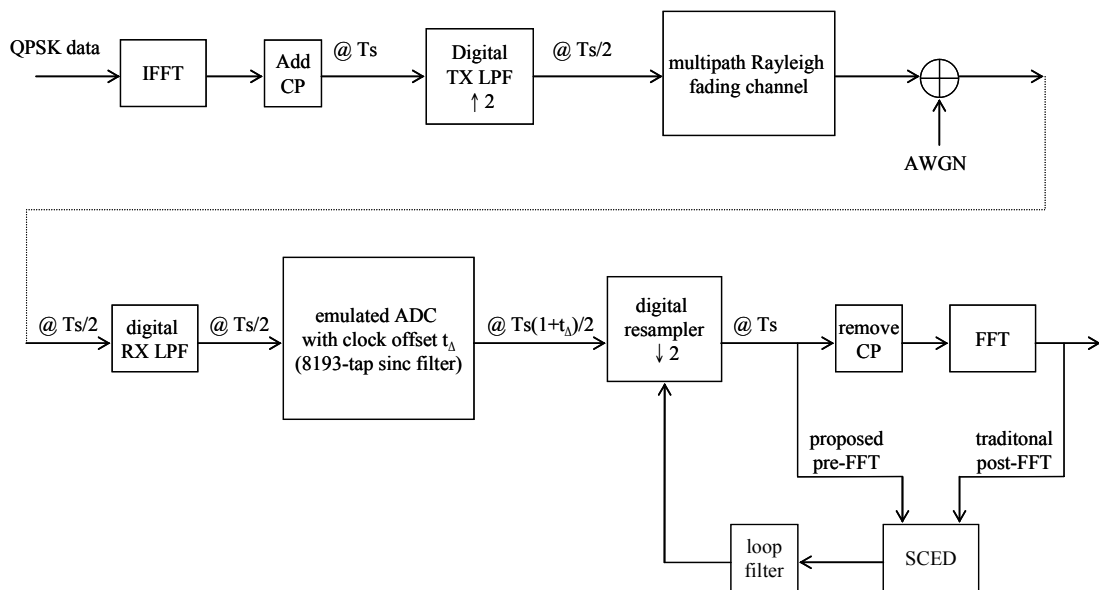
Figure 4-23 the simulation model for clock synchronization

For evaluating the performance of SCED, here we define a parameter, *residual clock offset* as the error between the mean value of tracked clock offset in steady state and the correct clock offset (here it is 100 ppm). In our simulations, we set the starting point of steady state at 2000th OFDM symbol and we select 1000 tracked clock offset for average. For the simulation, the statistic residual clock offset is the mean of the results in 16 trails.

In the following, we show the single-trial tracking diagram for sampling clock error to observe the tracking situation under different mobile velocities. Then, we present the statistic performance of SCED schemes by residual clock offset.

● **Tracking diagram of clock error with post-FFT SCED**

With the settings and parameters shown above, we show tracking diagrams for clock error here. Under the condition of an SNR of 25 dB, Figure 4-24 shows single trial of tracking diagrams for clock error with traditional post-FFT SCED. From Figure 4-24 (a) we can see, the clock error is tracked very well in a static environment. Nevertheless, in fast-fading surroundings, the results of clock tracking are very bad as shown in Figure 4-24 (b), (c) and (d); the faster the speed of a receiver is, the worse the tracking performance is. With a mobile velocity of 100 km/hr, the clock tracking may drift from the goal (100 ppm) by about 10ppm; for 200 and 300 km/hr, the error can reach up to 20 and 30 ppm, respectively. With such large clock error, it leads to serious FFT-window drift problem and cause the system performance to decay. Consequently, for a mobile system, traditional post-FFT algorithm cannot give a good performance due to the interference of channel variation.

Figure 4-24 (a) post-FFT tracking diagram of a clock offset 100 ppm in a static
environment

Figure 4-24 (b) post-FFT tracking diagram of a clock offset 100 ppm with a velocity
of 100 km/hr

78

Figure 4-24 (c) post-FFT tracking diagram of a clock offset 100 ppm with a velocity of 200 km/hr
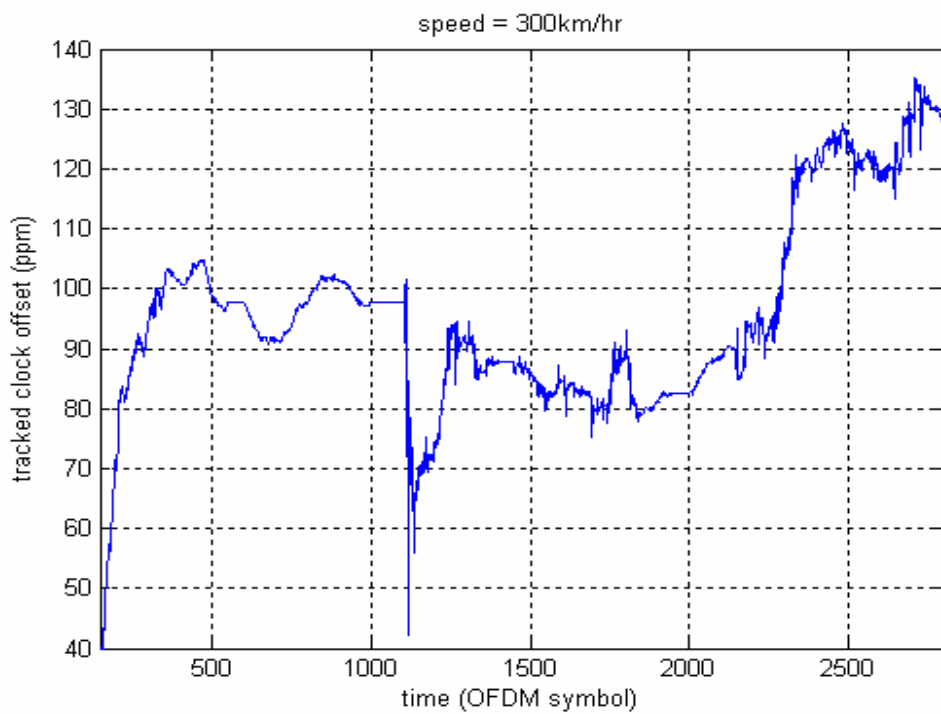
Figure 4-24 (d) post-FFT tracking diagram of a clock offset 100 ppm with a velocity of 300 km/hr

● **Tracking diagram of clock error with proposed pre-FFT SCED**

Figure 4-25 displays tracking diagrams of clock error with our proposed pre-FFT SCED with an SNR of 25 dB. From observation of those tracking diagrams, unlike the traditional post-FFT algorithm, the tracking ability of proposed pre-FFT algorithm is almost not affected by channel variation (i.e. mobile velocity). Because of the neglect of the differential terms after second order and interference in CP, the tracking ability of proposed pre-FFT algorithm in a static environment is not as good as post-FFT algorithm. However, the pre-FFT algorithm performs better than post-FFT algorithm increasingly as the mobile velocity. From Figure 4-25 we can see, no matter with a mobile velocity of 100, 200, or 300 km/hr, the tracking drift from 100 ppm is in no excess of 3 ppm while that of post-FFT SCED can be excess of 30 ppm with a mobile velocity of 300 km/hr.
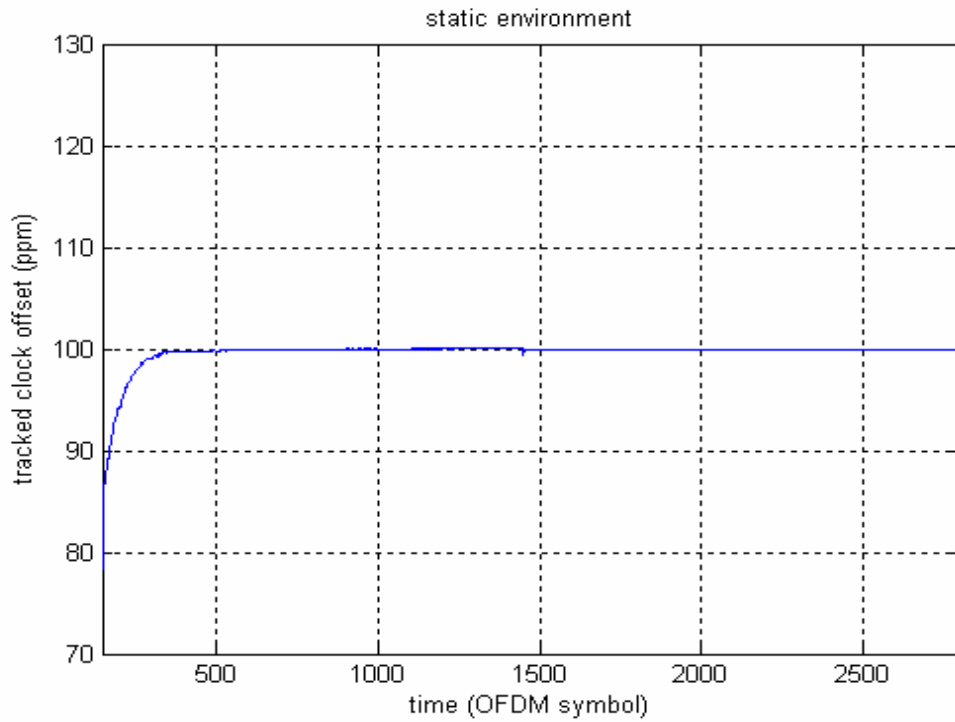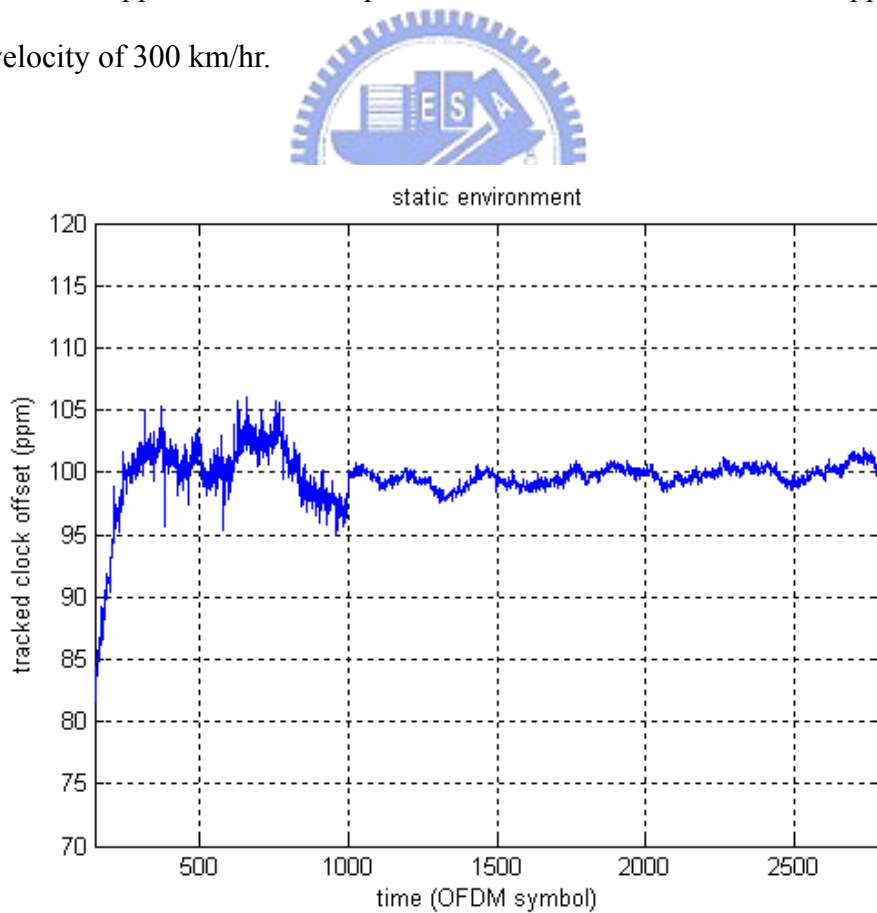

Figure 4-25 (a) proposed pre-FFT tracking diagram of a clock offset 100 ppm in a static environment
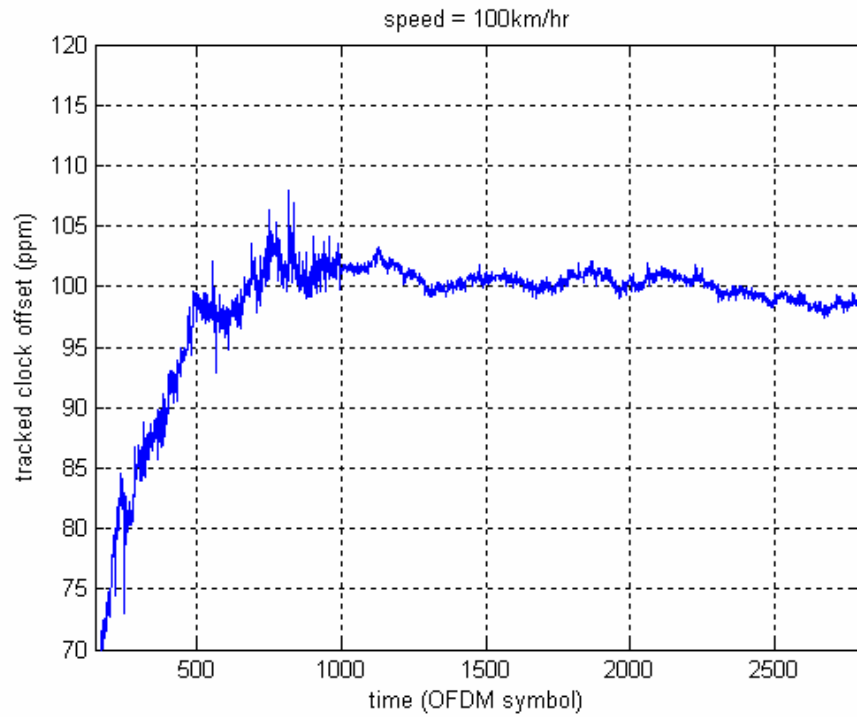
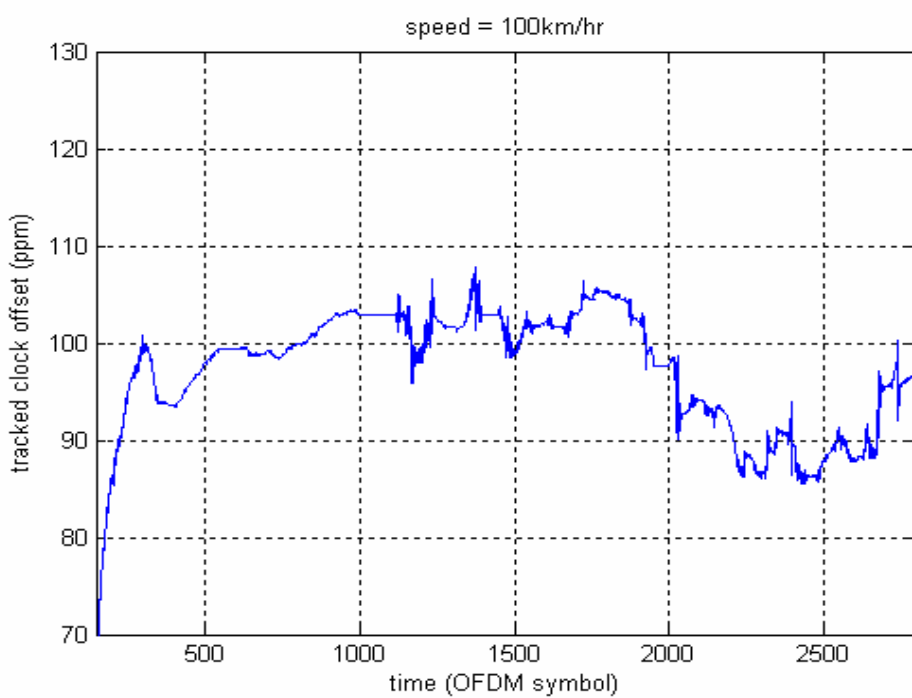Figure 4-25 (b) proposed pre-FFT tracking diagram of a clock offset 100 ppm with a velocity of 100 km/hr
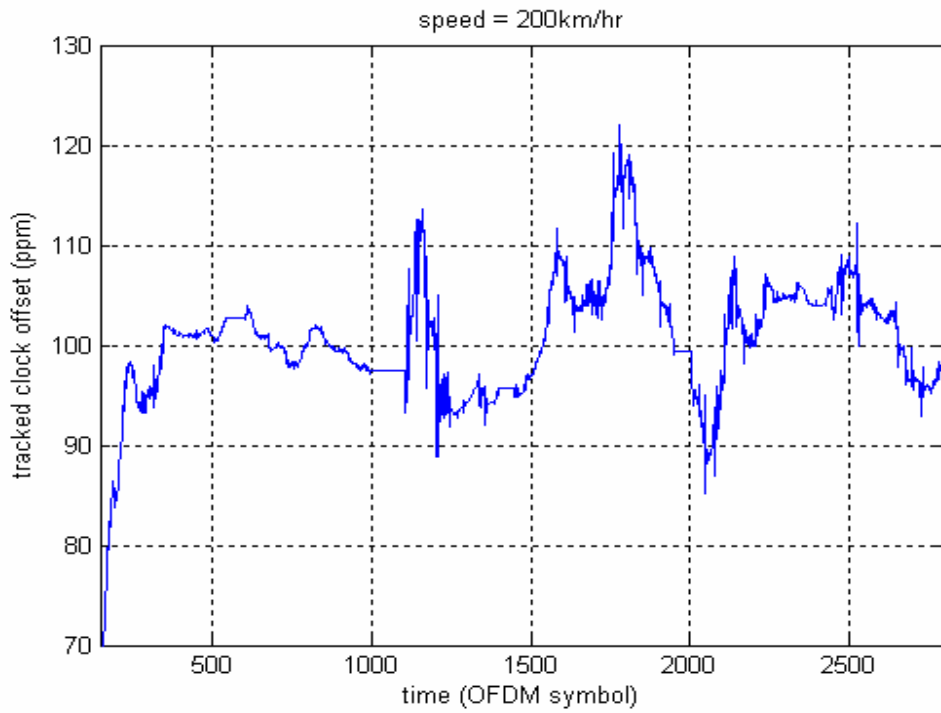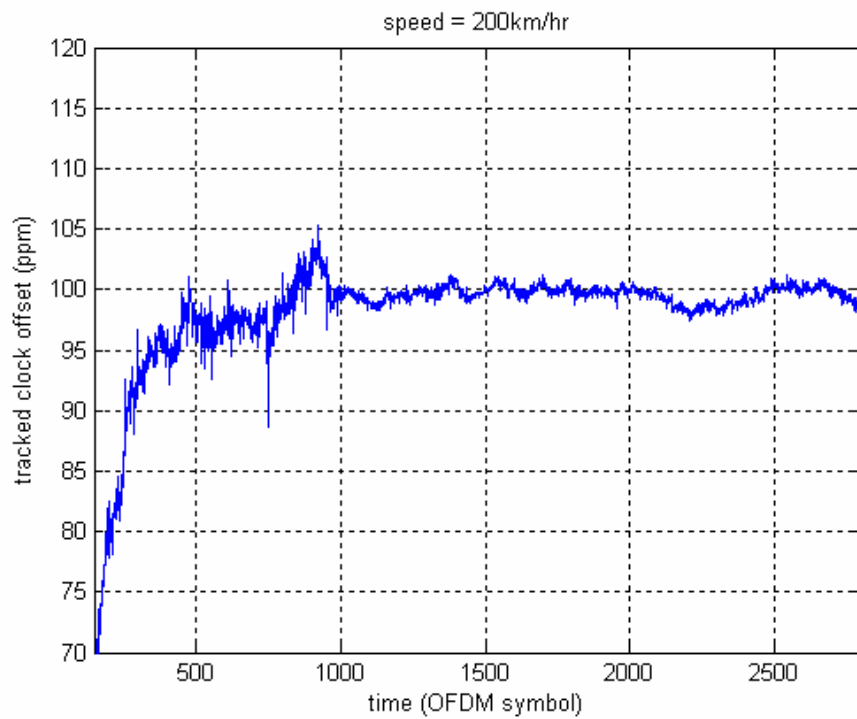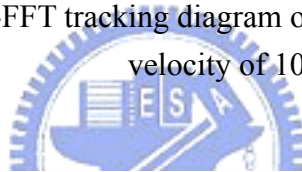

Figure 4-25 (c) proposed pre-FFT tracking diagram of a clock offset 100 ppm with a velocity of 200 km/hr
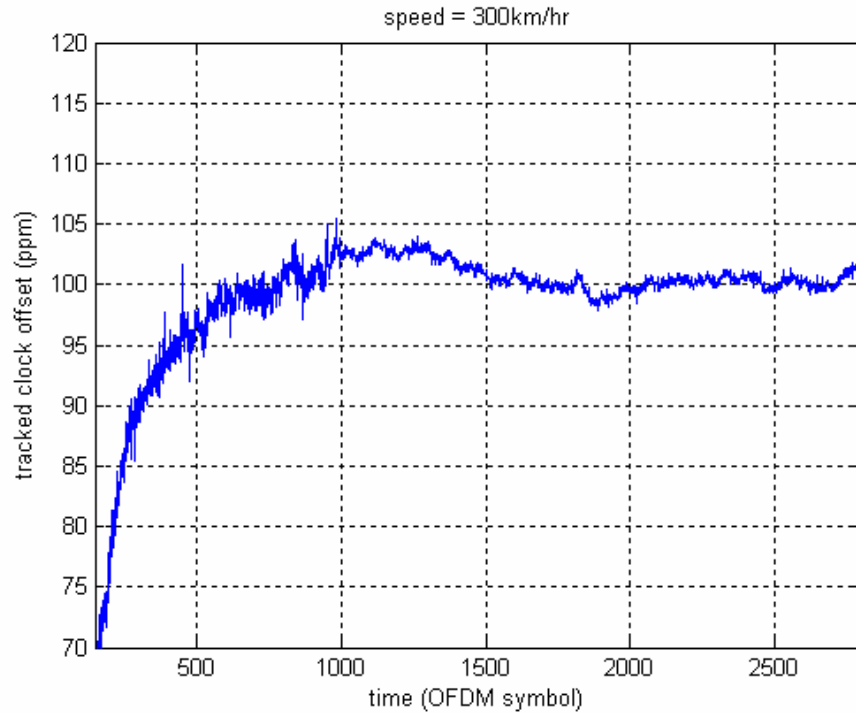
Figure 4-25 (d) proposed pre-FFT tracking diagram of a clock offset 100 ppm with a velocity of 300 km/hr

● **Comparison of post-FFT and pre-FFT SCED**

In last section, we see single trail of tracking for clock error. Here, we will show statistic performance by the residual clock offset. Figure 4-26 shows the tracking results of post-FFT and pre-FFT algorithms. From simulation, in a slow-fading channel, the residual offset can be reduced within 0.5 ppm and 1ppm using Post-FFT and Pre-FFT respectively which are both good enough for the system to prevent ICI interference (equation (3.22)). For a mobile receiver, the performance of Post-FFT algorithm is worse increasing as speed. With speeds of 100, 200, and 300 km/hr, it leaves a clock offset of about 7 ppm, 9 ppm, 15 ppm respectively and these results in a larger power of ICI which cannot be ignored especially in high-level modulation. In the other hand, proposed pre-FFT strategy in a mobile environment still performs as well as in a static one. In conclusion, the pre-FFT algorithm is better choice if the system is demanded to run in a mobile circumstance.

The post-FFT algorithm has poor endurance to a mobile environment while the pre-FFT one is very robust to a fast-fading channel. However, in a static environment, the tracking ability of the post-FFT algorithm is better than that of the pre-FFT algorithm. It is because the post-FFT algorithm utilizes symbols in frequency domain at an interval of four OFDM symbols which may suffer from the interference of channel variation. At the other hand, the pre-FFT one makes use of guard interval in one OFDM symbol which is affected by channel less. Nevertheless, the drawback of using guard interval is that CP is interfered by channel dispersion and has ISI problem. As a result, the pre-FFT algorithm operates not so well in a slow-fading channel. Moreover, the pre-FFT algorithm do not need additional reference data to work while the post-FFT algorithm needs assistant of pilots which results in the decrease of efficient data rate.
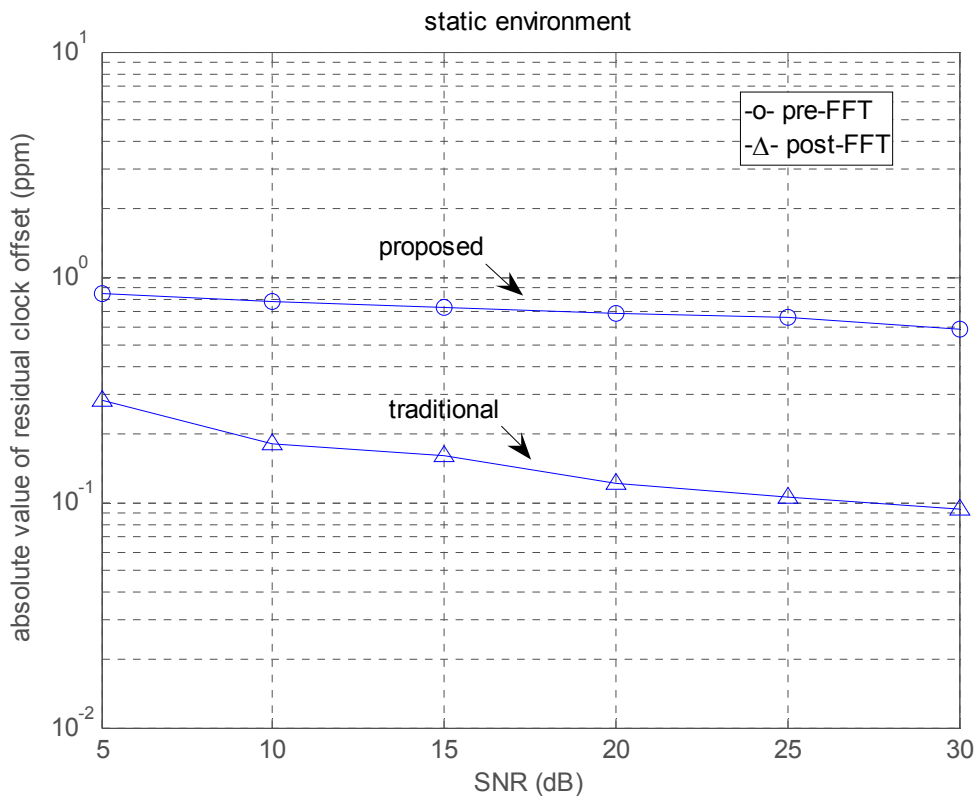
Figure 4-26 (a) tracking performance comparison in a static environment
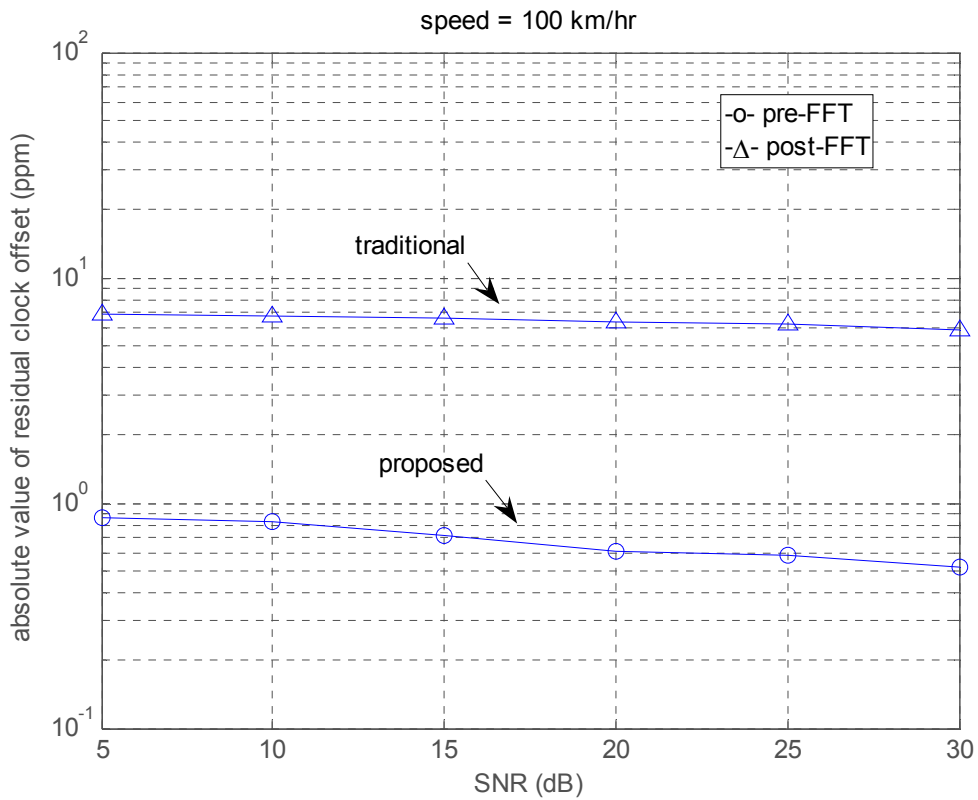
Figure 4-26 (b) tracking performance comparison under a velocity of 100 km/hr
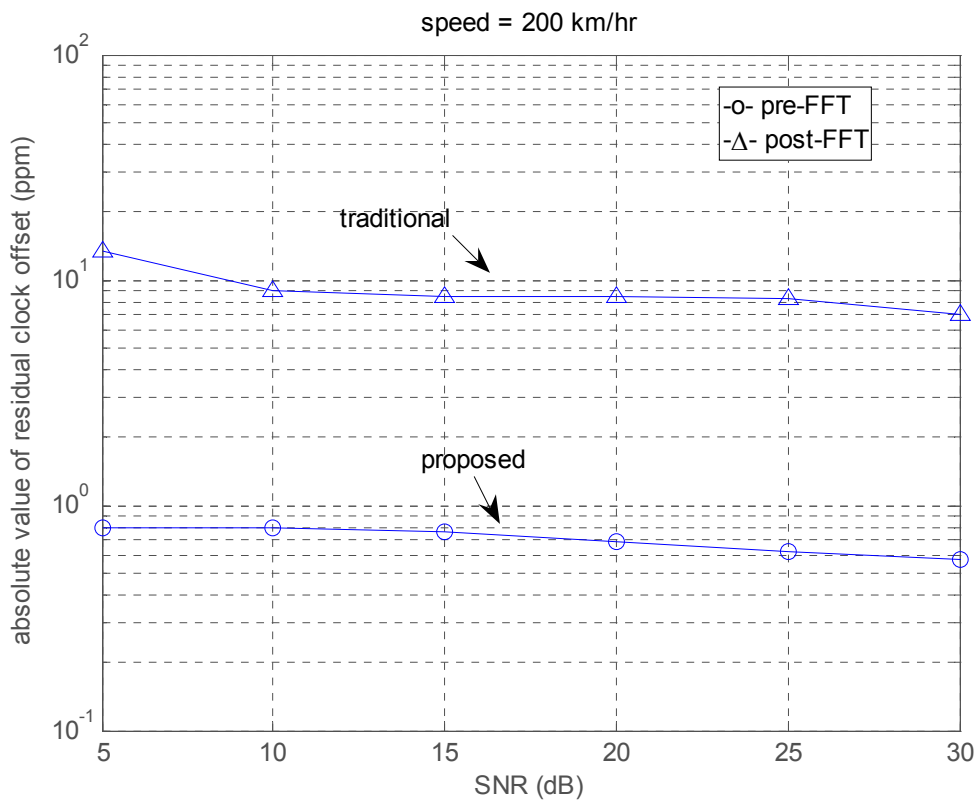
Figure 4-26 (c) tracking performance comparison under a velocity of 200 km/hr
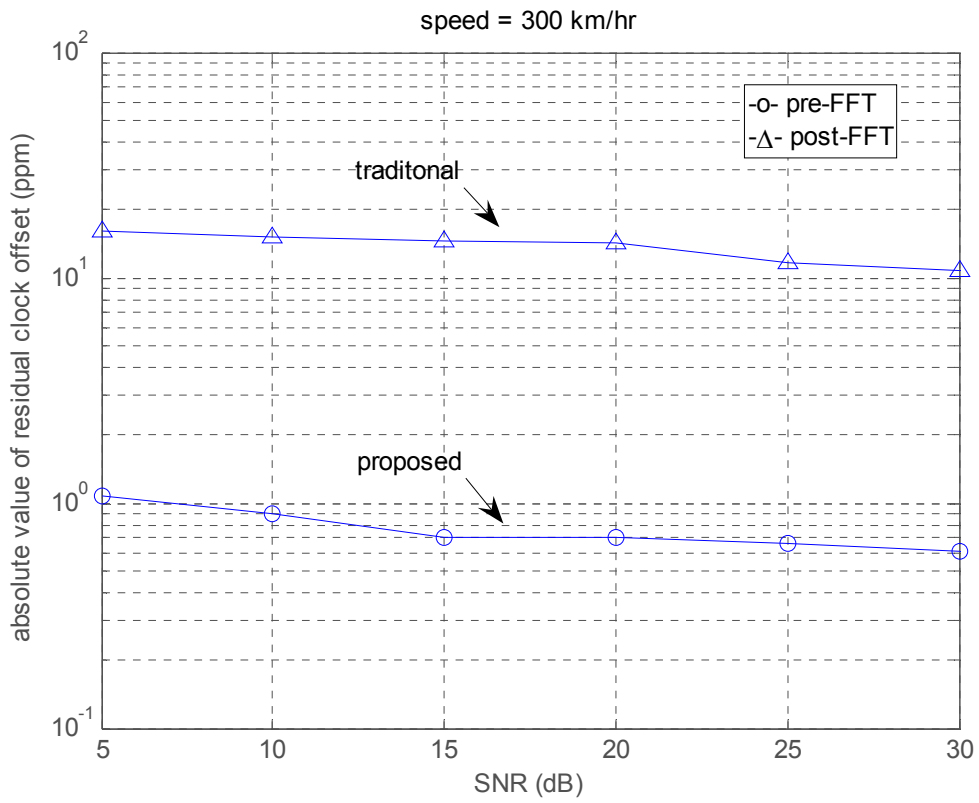
Figure 4-26 (d) tracking performance comparison under a velocity of 300 km/hr

Chapter 5
Symbol Synchronization, Carrier Synchronization, and Channel Estimation

In the inner receiver, except for sampling clock synchronization in chapter 4, there are other components of inner receiver as illustrate in Figure 4-5 introduced in this chapter. First, we need find the boundary of OFDM symbol for FFT operation and it is symbol synchronization which is present in section 5.1. Following in section 5.2 is the carrier synchronization which detects the carrier frequency error and compensates for it. Like sampling clock synchronization, there are two schemes, pre-FFT and post-FFT schemes, that will be given and compared. Finally, the algorithm of estimating channel is introduced.

5.1 Symbol Synchronization

For a receiver of OFDM system, the FFT window of each OFDM block is claimed to synchronized prior for delivering N samples to FFT and it is called "symbol synchronization". That is to say, the goal of symbol synchronization is to find the starting point of each OFDM symbols. In a DVB-T system, unlike IEEE 802.11a, there is no training symbol that can be utilized, hence it must utilize the

cyclic property of guard interval to estimate the symbol boundary [27, 28]. As Figure 5-1 shows, the part of CP has the same values with the part of Δ.

Figure 5-1 cyclic property of guard interval

We first consider an AWGN channel and neglect the effect of sampling clock offset. The nth sample with the effect of carrier frequency offset Δf_c can be written as:

$$
\begin{aligned}
\hat{r}_n &= r_n e^{j2\pi\Delta f_c nT_s} + z_n = r_n e^{j2\pi\Delta f_c T_u n/N} + z_n \\
&= r_n e^{j2\pi\Delta f_c' n/N} + z_n
\end{aligned}
\tag{5.1}
$$

where r(n) is the nth sample without the effect of Δf_c, $\Delta f_c'$ is normalized frequency offset to subcarrier frequency interval ($\Delta f = 1/T_u$) and z_n is AWGN noise of nth sample. With the cyclic property of guard interval, we make use of their correlation to judge the symbol boundary point. Define a correlation $u(\theta)$ as :

$$
\begin{aligned}
u(\theta) &= \sum_{n=\theta}^{\theta+N_g-1} \hat{r}_n \cdot \hat{r}_{n+N}^* \\
&= \sum_{n=\theta}^{\theta+N_g-1} r_n e^{j2\pi\Delta f_c' n/N} \cdot r_{n+N}^* e^{-j2\pi\Delta f_c'(n+N)/N} \\
&= \sum_{n=\theta}^{\theta+N_g-1} r_n r_{n+N}^* \cdot e^{-j2\pi\Delta f_c'}
\end{aligned}
\tag{5.2}
$$

where θ is the estimated starting point of the correlation and noise is ignored. Because CP and Δ have the same value, the correlation has a peak absolute value when θ is chosen to the beginning point of CP. By comparing the correlations of all θ which has a range of N_s points, the θ with max absolute value of correlation should be the

correct symbol boundary. Therefore, the estimated symbol boundary is found by:

$$\hat{\theta} = \arg(\max_{\theta} | u(\theta) |) \qquad (5.3)$$

In a multipath fading channel, however, the preceding part of CP suffers from ISI problem which is illustrated in Figure 5-2. In order to avoid ISI interference, the summation range of u(θ) is chosen to the ISI-free part Ω with length l_Ω so that equation (5.2) becomes

$$u(\theta) = \sum_{n=\theta}^{\theta+l_\Omega-1} \hat{r}_n \cdot \hat{r}_{n+N}^* \qquad (5.4)$$

Otherwise, still use the part with ISI and treat ISI as other additional noise.
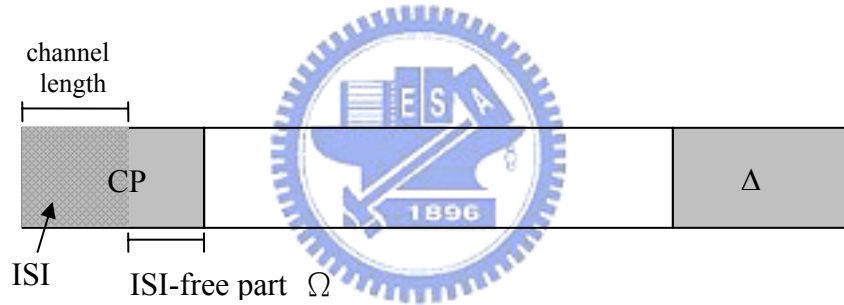
Figure 5-2 guard interval with ISI effect

In the chapter 3, we have discussed the effect of symbol boundary error. From equation (3.25) and (3.27), we know that there is only a phase rotation for symbol in the case of $N_e > 0$ while a phase rotation, ISI, and ICI effect for symbol in the other case of $N_e < 0$. It is obvious that if there is an inevitable symbol boundary error due to noise, the case of $N_e > 0$ is a better choice. As a result, a bias N_b is usually given to the estimated symbol boundary for the prevention of the case of $N_e < 0$. However, the bias N_b can not let the biased estimated symbol boundary exceed beyond the part of Ω; otherwise, ISI will be introduced to the symbols.

5.2 Carrier Frequency Synchronization

In a DVB-T system, there is no constrain for the magnitude of frequency carrier offset. The offset may be large to several subcarrier spacings so the synchronization is with three steps. At the beginning, we distinguish the carrier offset (Δf_c) between integer part (Δf_I) and fractional part (Δf_F) and normalize them to subcarrier spacing ($\Delta f = 1/T_u$):

$$\Delta f_c = \Delta f_I + \Delta f_F = (n_I + \Delta f_F')(1/T_u) \qquad (5.5)$$

$$\Delta f_c' = \Delta f \cdot T_u = \Delta f_I' + \Delta f_F' \qquad (5.6)$$

where $\Delta f_I'$ is the normalized integer offset and $\Delta f_F'$ is the normalized fractional offset. For example, supposing that the carrier offset is 100ppm and carrier frequency is 500MHz, Δf_c is equal to 50kHz and it leads to a integer bias $\Delta f_I' = 11$ and a fractional bias $\Delta f_F' = 0.2$ in the carrier frequency.

To detect the carrier offset, a three-step scheme is our scenario [18, 19]. The first step is pre-FFT coarse carrier synchronization which is acquisition stage for the fractional part preceding the FFT operation. The second is post-FFT integer carrier synchronization which estimates the integer part post-FFT operation. The last is fine carrier synchronization which is tracking stage for the fractional part either before FFT or after FFT operation. After detecting the carrier frequency offset, we compensate for it after AD converter by rotating the phase effect back in time domain.

5.2.1 Pre-FFT Coarse Carrier Synchronization

Together with symbol synchronization, pre-FFT coarse carrier synchronization makes use of the cyclic property of guard interval. From equation (5.2), the correlation can be rewrite with a normalized offset as

$$
\begin{aligned}
u(\theta) &= \sum_{n=\theta}^{\theta+N_g-1} r_n r_{n+N}^* \cdot e^{-j2\pi\Delta f_c'} \\
&= \sum_{n=\theta}^{\theta+N_g-1} r_n r_{n+N}^* \cdot e^{-j2\pi(\Delta f_I' + \Delta f_F')} \\
&= \sum_{n=\theta}^{\theta+N_g-1} r_n r_{n+N}^* \cdot e^{-j2\pi\Delta f_F'}
\end{aligned}
\qquad (5.7)
$$

Assume that the estimated symbol boundary $\hat{\theta}$ is correct, with the property of CP

$$
r_{n+N} = r_n, \qquad n \in CP \qquad (5.8)
$$

equation (5.7) changes to

$$
u(\hat{\theta}) = \sum_{n=\hat{\theta}}^{\hat{\theta}+N_g-1} |r_n|^2 \cdot e^{-j2\pi\Delta f_F'} \qquad (5.9)
$$

Therefore, the fractional part of carrier offset can be derived as

$$
\Delta f_F' = \frac{-1}{2\pi} \angle \{u(\hat{\theta})\} \qquad (5.10)
$$

which is ML (Maximum-Likelihood) frequency estimation [27].

Due to phase ambiguity, this strategy can only detect the fractional part $\Delta f_F'$ ranged from -0.5 to +0.5 and can not estimate the value of the integer part $\Delta f_I'$. In addition, the performance of this algorithm using CP largely depends on the channel characteristic due to ISI noise. Therefore, we need other stages to estimate the integer offset and fractional offset more accurately.

5.2.2   Post-FFT Integer Carrier Synchronization

With the effect of carrier offset, the frequency of each subcarrier is shifted. Figure 5-3 illustrates the effect of an integer carrier offset $\Delta f_I'$ which cause all carrier frequencies shifted by $\Delta f_I'$ subcarrier spacing. In other word, the received symbol at the kth subcarrier is actually from the $(k-\Delta f_I')$th subcarrier. Accordingly, the signal after FFT can be modified from equation (3.21) into the form

$$R_{l,k} = (e^{j\pi\phi_k'} \cdot e^{j2\pi\frac{lN_s+N_g}{N}(\Delta f_I'+\phi_k')}) \cdot \sin c(\phi_k') X_{l,k-\Delta f_I'} C_{l,k-\Delta f_I'} + noise \qquad (5.11)$$

where

$$\phi_k' = \Delta f_F' + t_\Delta \cdot (k - \Delta f_I') \qquad (5.12)$$

Thanks to the first-step synchronization, the residual fractional offset $\Delta f_F'$ is small so that the effect of ICI noise can be negligible here.
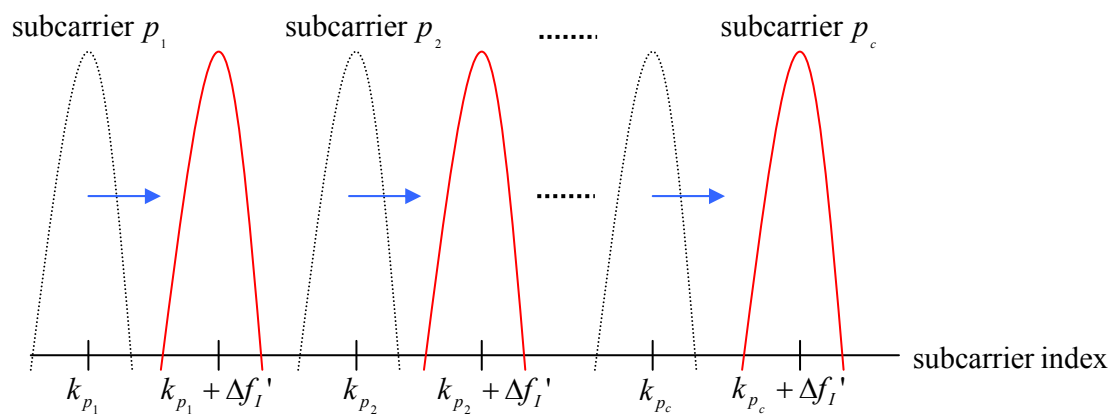

Figure 5-3 frequency shift due to a carrier offset

In the estimation of integer offset, we utilize the correlation of two consecutive OFDM symbols which is

$$\Psi_{l,\Lambda} = \sum_{k\in\Lambda} R_{l,k} \cdot R^*_{l-1,k}$$

$$= \sum_k (e^{j2\pi\frac{N_s}{N}(\Delta f_I'+\phi_k')}) \cdot \sin c^2(\phi_k')(X_{l,k-\Delta f_I'} X^*_{l-1,k-\Delta f_I'})(C_{l,k-\Delta f_I'} C^*_{l-1,k-\Delta f_I'}) + noise \qquad (5.13)$$

Then we need aid of reference data to detect $\Delta f_I'$ from equation (5.13). With regard to continual pilots, we have known their carrier frequency indices as

$$C : \{k_{p_1}, k_{p_2}, ..., k_{p_c}\} \qquad (5.14)$$

but receive them at the location

$$C_{\Delta f_I'} : \{k_{p_1} + \Delta f_I', k_{p_2} + \Delta f_I', ..., k_{p_c} + \Delta f_I'\} \qquad (5.15)$$

From chapter 2, the values of pilots with the same subcarrier indices are all the same and are either +4/3 or -4/3. In addition, because now we are going to detect an "integer" estimator the effect of channel variation during one OFDM symbol is relatively small and can be neglected for the correlation in equation (5.13). Accordingly, the correlation with $k \in C_{\Delta f_I'}$ becomes

$$\Psi_{l,C_{\Delta f_I'}} = \sum_{k\in C_{\Delta f_I'}} (e^{j2\pi\frac{N_s}{N}(\Delta f_I'+\phi_k')}) \cdot \sin c^2(\phi_k') \frac{16}{9} | C_{l,k-\Delta f_I'} |^2 + noise$$

$$= \frac{16}{9} e^{j2\pi\frac{N_s}{N}\Delta f_I'} \sum_{k\in C_{\Delta f_I'}} (e^{j2\pi\frac{N_s}{N}\phi_k}) \cdot \sin c^2(\phi_k') | C_{l,k-\Delta f_I'} |^2 + noise \qquad (5.16)$$

Considering small residual offsets $\Delta f_F'$ and t_Δ, owing to the full correlation of pilots with the same subcarrier index, the absolute value of $\Psi_{l,C\varepsilon}$ is large provided that ε is equal to $\Delta f_I'$; Otherwise, the correlation has the terms multiplied by uncorrelated data symbol so that the absolute value of $\Psi_{l,C\varepsilon}$ will be small. Therefore, we can search $\Delta f_I'$ for a range $\varepsilon \in [-N_I, N_I]$ by judge if $(C+\varepsilon)$ is matched to $C_{\Delta fI'}$ or not; namely, find the maximum absolute value of $\Psi_{l,C\varepsilon}$ for the given range of ε :

$$\Delta \hat{f}_I \, ' = \arg \{ \max_{\varepsilon \in [-N_I, N_I]} | \Psi_{l,C_\varepsilon} | \} \qquad (5.17)$$

5.2.3   Fine Carrier Synchronization

After the first and second stage of carrier synchronization, there is only a small residual offset remaining. At the last step, we use a close loop to track the residual offset as shown in Figure 5-4. There are two schemes at this stage. One is post-FFT estimation [18] and the other is pre-FFT estimation [19].

Remembering that in Chapter 4, we can utilize scattered pilots to estimate the clock offset and carrier offset simultaneously by LS criterion. From equation (4.18), the estimated residual offset is

$$\Delta \hat{f}_F \, ' = \frac{(\sum_{p=1}^{N_p} k_p{}^2) \cdot (\sum_{p=1}^{N_p} \phi_{k_p}) - (\sum_{p=1}^{N_p} k_p) \cdot \sum_{p=1}^{N_p} \phi_{k_p} k_p}{N_p \cdot \sum_{p=1}^{N_p} k_p{}^2 - (\sum_{p=1}^{N_p} k_p)^2} \qquad (5.18)$$

However, like sampling clock synchronization, it has the effect of channel variation in the frequency domain. As a result, the estimation error in a fast-fading channel will be significant. Therefore, we take account of pre-FFT synchronization like clock synchronization. The way for pre-FFT synchronization is using the same strategy with that of the first stage. In other word, seek the aid of guard interval. After the coarse synchronization for carrier and clock offsets, the interference is reduced largely hence the result of the scheme using CP at this stage is more precise than that at the first stage . The estimated residual offset is

$$\Delta \hat{f}_F' = \frac{-1}{2\pi} \angle \{ \sum_{n=\theta_l}^{\theta_l+N_g-1} \hat{r}_{l,n} \cdot \hat{r}_{l,n+N}^* \} \qquad (5.19)$$

where θ_l is the correct starting point of lth OFDM symbol.
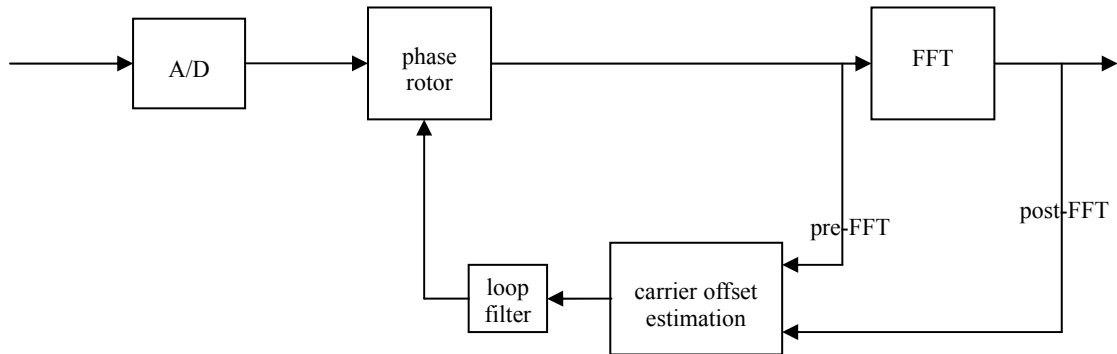
Figure 5-4 tracking loop for carrier offset

5.2.4 Performance Analysis

● **Simulation parameters**

This section gives the comparative performance analysis between these two schemes for carrier synchronization:

TD scheme : pre-FFT coarse carrier synch. + post-FFT carrier synch. for integer part

+ *pre-FFT* fine carrier synch.

FD scheme : pre-FFT coarse carrier synch. + post-FFT carrier synch. for integer part

+ *post-FFT* fine carrier synch.

The simulation parameters are listed in Table 5-1. Here we assume there is no clock offset and symbol synchronization is performed perfectly. As clock tracking, we also use the second-order loop filter with two sets of parameters. Furthermore, we also define the *residual carrier offset* as the error between the mean value of tracked

carrier offset in steady state and the correct carrier offset (here it is 100ppm). In our simulations, we set the starting point of steady state at 2000th OFDM symbol and we select 1000 tracked carrier offset for average. For the simulation, the statistic residual carrier offset is the mean of the results in 16 trails.

system	DVB-T
transmission mode	2K
channel bandwidth	8MHz
CP mode	1/8
modulation	QPSK
channel model	HT in COST207
carrier frequency f_c	500MHz
carrier frequency offset	100 ppm
sampling clock offset	0 ppm
mobile velocity	0, 100, 200, 300 km/hr
loop filter parameter [K_0,K_1]	[0.015,0.005], [0.004, 0.0016]

Table 5-1 simulation parameters for carrier synchronization

● **Simulation results**

Figure 5-5 shows the performance of these two tracking methods. In a motionless environment, with the same condition of clock synchronization, the carrier synchronization has better performance with the aid of reference data in frequency domain than that of CP in time domain shown in Figure 5-5 (a). However, for the same reason with clock synchronization, the post-FFT estimation is influenced by channel variation largely while the pre-FFT one is robust to a fast-fading channel as

shown in Figure 5-5 (b), (c), and (d). From the simulation results, in a static condition, the residual carrier offsets of schemes are both under 10^{-3} subcarrier interval which is small enough to prevent the interference. With a speed of 100 and 200km/hr, the residual carrier offsets of FD scheme are worsen to 10^{-2} level while those of TD scheme are almost remaining the same under 10^{-3}. With a speed up to 300km/hr, the residual carrier offset of FD scheme is almost up to 10-1 level which leads to the interference with non-neglected power while that of TD scheme is still almost the same under 10^{-3}.
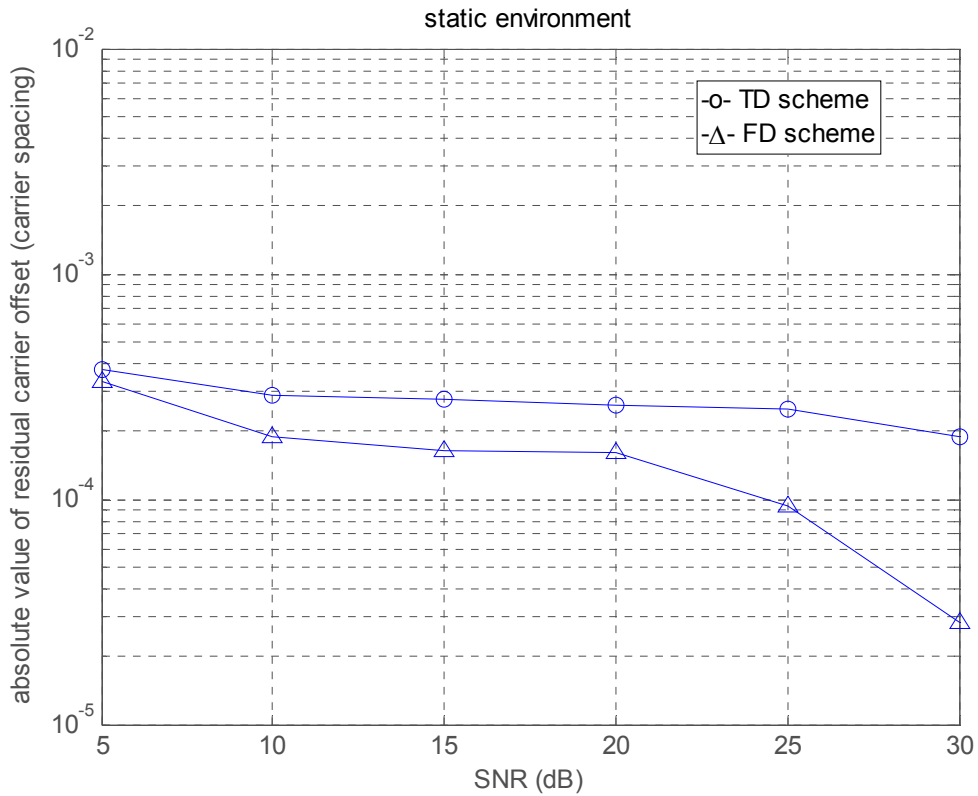
Figure 5-5 (a) performance of carrier synchronization in a static environment
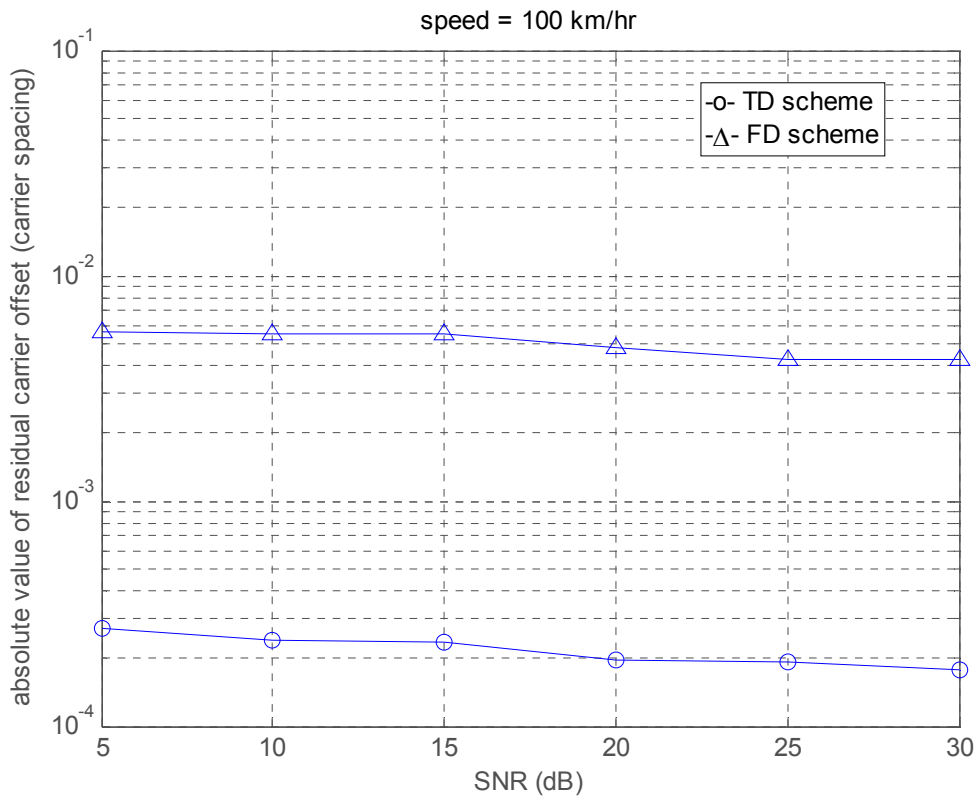
Figure 5-5 (b) performance of carrier synchronization with a velocity of 100 km/hr
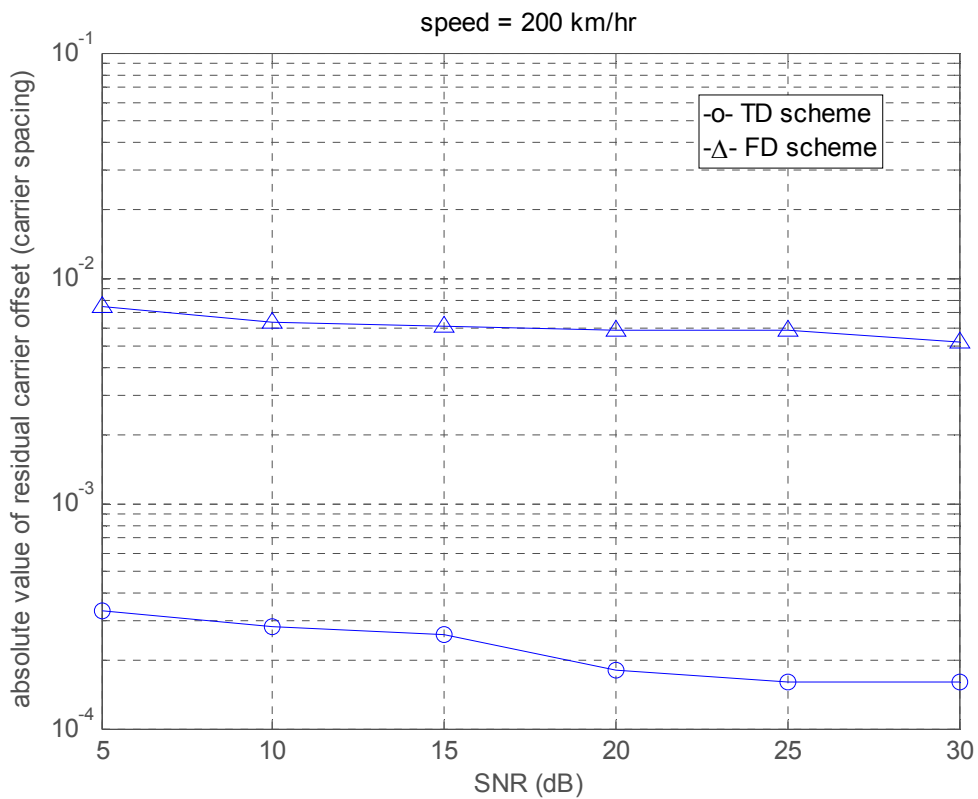
Figure 5-5 (c) performance of carrier synchronization with a velocity of 200 km/hr

97
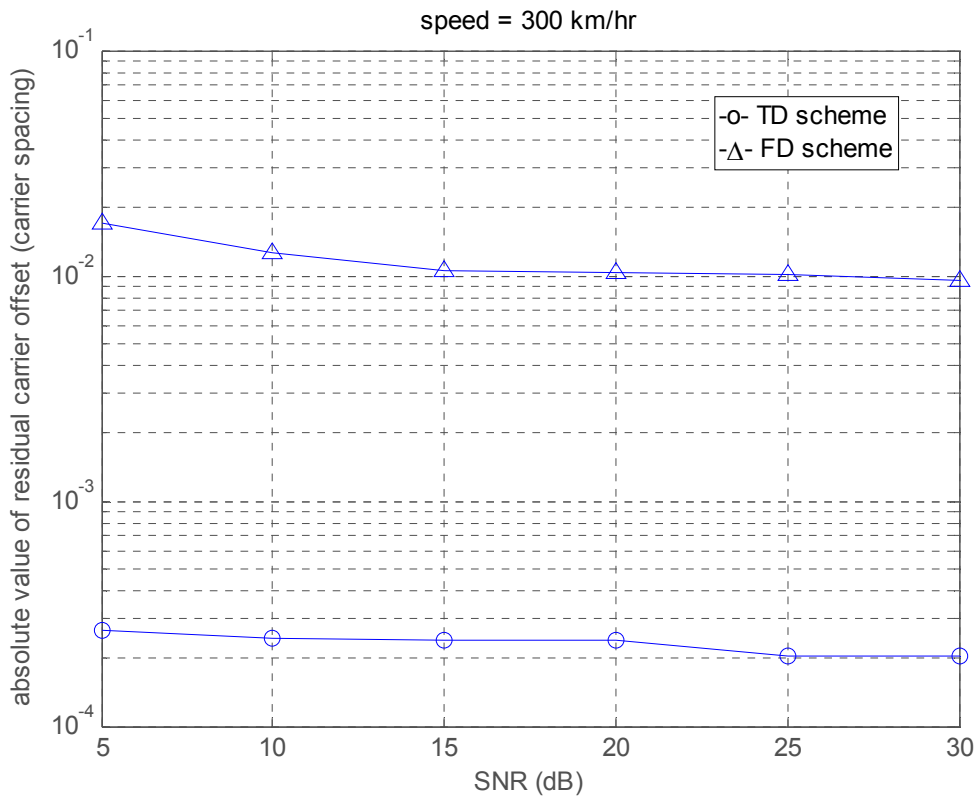
Figure 5-5 (d) performance of carrier synchronization with a velocity of 300km/hr

5.3 Channel Estimation

In a multipath fading channel, the received signals has problem of phase shift and amplitude variation due to the channel and non-ideal synchronization. The purpose of the channel estimation unit is to estimate these phase shift and amplitude variation for equalizer to eliminate them before data detection. In a DVB-T system, we can make use of scattered pilots to estimate the channel responses at those corresponding subcarrier frequencies. Then, with these estimated channel response, other channel responses at data-carrying subcarrier frequency can be found by interpolation. With these estimated channel response, we then can equalize the received post-FFT symbols by a single-tap equalizer.

Provided that carrier and clock synchronization are done perfectly, the post-FFT

signal can be written from equation (3.11) as

$$R_{l,k} = X_{l,k}C_{l,k} + N_{l,k} \qquad (5.20)$$

and the estimated channel response at the kth subcarrier can be obtained as

$$\hat{C}_{l,k} = \frac{R_{l,k}}{X_{l,k}} = C_{l,k} + \frac{N_{l,k}}{X_{l,k}} \qquad (5.21)$$

if we know the transmitted symbol $X_{l,k}$. In a DVB-T system, with the aid of scattered pilots, we can get the channel response at these locations of scattered pilots, $k_p = 12i + 3(l-1)$ where $i = 0, 1, 2\ldots$ as shown in Figure 5-6:

$$\hat{C}_{l,k_p} = \frac{R_{l,k_p}}{X_{l,k_p}} = C_{l,k_p} + \frac{N_{l,k_p}}{X_{l,k_p}}, \quad k_p \in SP \qquad (5.22)$$

With these samples, to get complete channel response, we can interpolate them in frequency direction. If the channel is time-variant, we need also interpolate the channel responses in time direction.
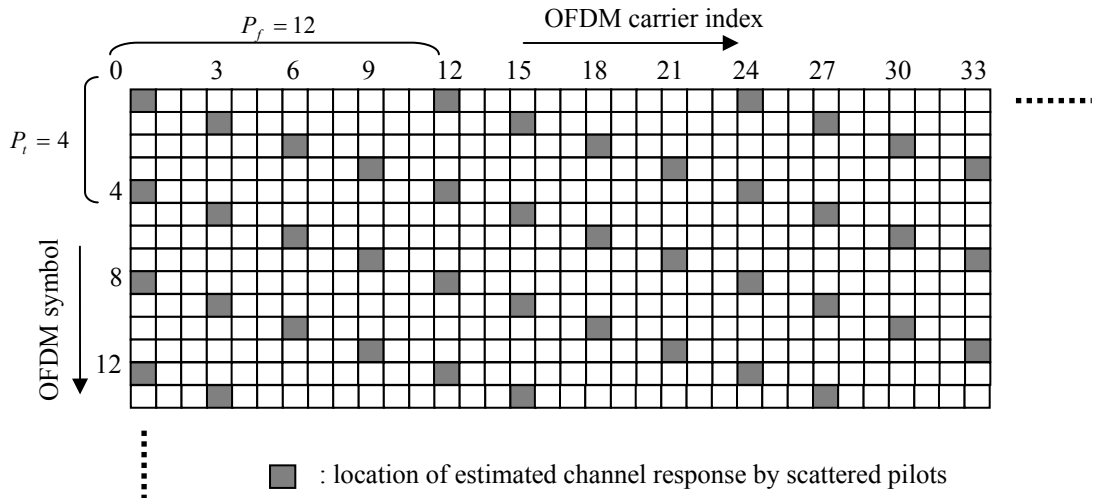
Figure 5-6 the location of available channel response by scattered pilots

5.3.1 Interpolation in Frequency Direction

After estimating the channel by scattered pilots, the estimated channel response is

$$\hat{C}_{l,k} = \begin{cases} C_{l,k}, & k = 12i + 3(l-1), \quad i = 0,1,2,... \\ 0, & otherwise \end{cases} \qquad (5.23)$$

which is equal to the effect that channel impulse response convolves with impulse trains as illustrated in Figure 5-7. To prevent aliasing phenomenon, the sampling period in frequency direction P_f should be chosen by Nyquist theory so that

$$\frac{1}{P_f \Delta f} > \tau_{max} \qquad (5.24)$$

where $\Delta f = 1/T_u$ is subcarrier spacing and τ_{max} is the maximum delay spread of the channel. Consider the worst case in DVB-T that τ_{max} is equal to the max CP duration, $T_u/4$, the sampling period in frequency direction must satisfy

$$P_f < \frac{1}{\tau_{max} \Delta f} = 4 \qquad (5.25)$$

For the original version of scattered pilots, P_f is equal to 12 so it gives rise to aliasing problem. However, if interpolation in time domain apply first, the resulting sampling period in frequency direction changes to $P_f' = 3$ as shown in Figure 5-8 and is able to satisfy equation (5.25).

Figure 5-7 effect in time domain for sampled channel response
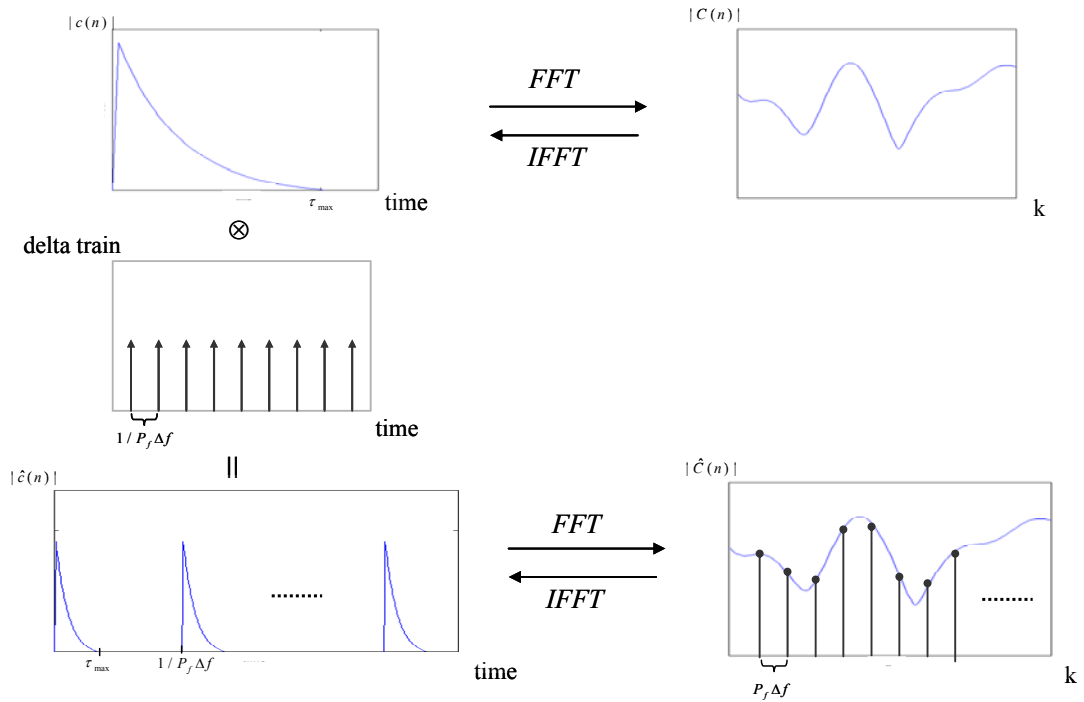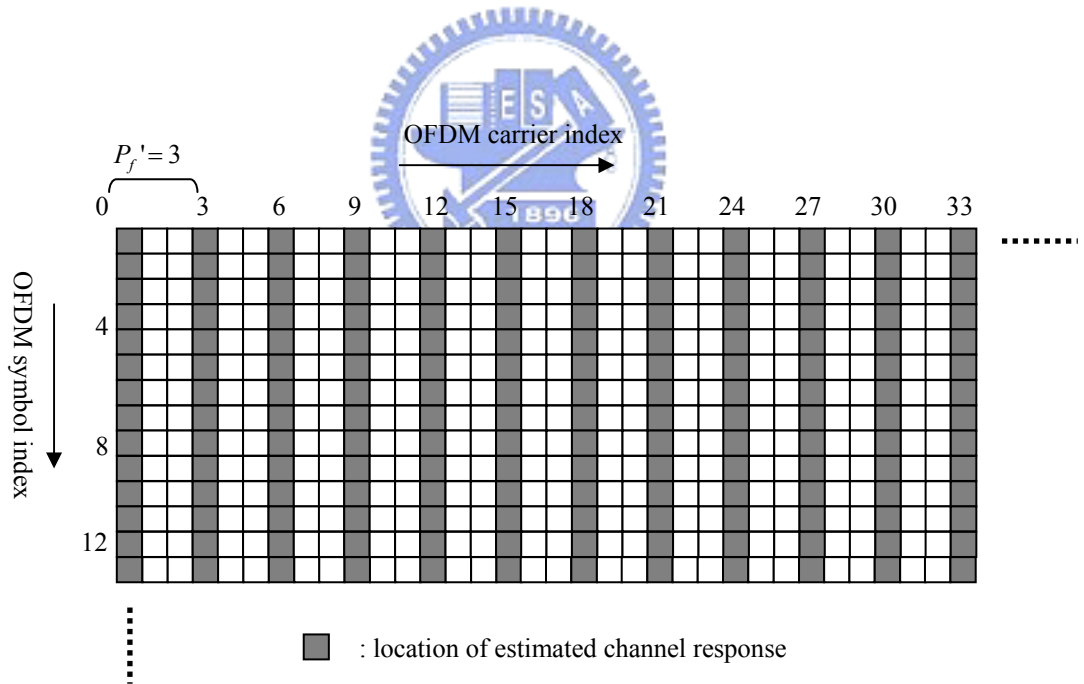

: location of estimated channel response

Figure 5-8 the location of available channel response by interpolation in time direction

5.3.2 Interpolation in Time Direction

Because of the non-ideal clock and carrier synchronization, there are residual clock and carrier offsets causing the effect of rotation in frequency domain. Accordingly, we need estimate the channel for an interval of T_N OFDM symbols. With a good synchronization, the residual offsets are very small so the interval T_N may be large. In a mobile system, the channel varies with time increasingly as the mobile velocity so the interval T_N depends on the mobile velocity. With a relative velocity of v, a receiver suffers from the effect of Doppler shift in frequency. Considering a maximum Doppler shift f_D, like interpolation in frequency direction, T_N must satisfy

$$\frac{1}{T_N T_{sym}} > 2f_D \qquad (5.26)$$

to prevent the aliasing phenomenon.

5.3.3   Interpolation Methods

As introduction above, after channel estimation at the locations of scattered pilots we must estimate other channel responses at the locations of data-carrying subcarriers in frequency direction. For a mobile system, we also need interpolation for channel responses in time direction. In addition, we state constrain for alias-free interpolation. In this section, we discuss two interpolation methods for channel estimation.

1. Linear interpolation

Linear interpolation [29] is the simplest way for interpolation but may have larger interpolated error. It may be suitable for interpolation in time direction as long as the Doppler shift is not serious. In this way, the unknown channel response can be

obtained by

$$\hat{C}_{l,k} \equiv (1 - \frac{k \bmod 3}{3})\hat{C}_{l,3[\frac{k}{3}]} + \frac{k \bmod 3}{3}\hat{C}_{l,3[\frac{k}{3}]+3} \qquad (5.27)$$

where [x] denotes the integer part of x.

2. DFT-based interpolation

The method [30] is to transform T known channel samples estimated by scattered pilots from frequency domain to time domain. Under the constrain in equation (5.25), this leads to the channel impulse response. Then, perform zeros-padding operation to add the number of samples to N and then the channel frequency response can be got by transforming the N samples back to frequency domain. Figure 5-9 models the structure of the DFT-based interpolation.
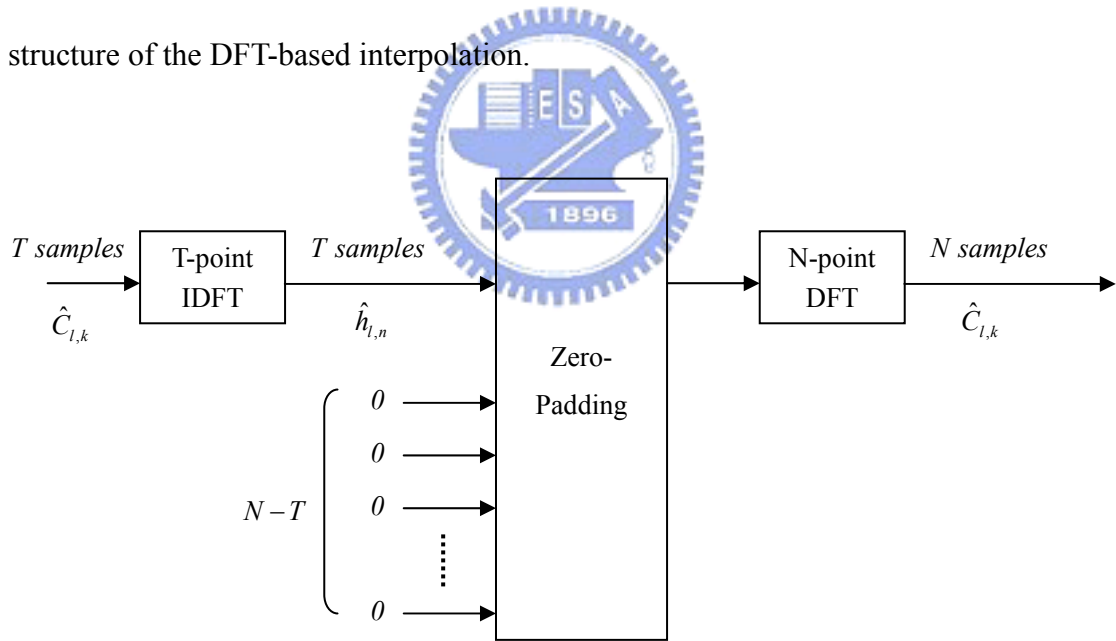
Figure 5-9 DFT-based channel interpolation model

103

Chapter 6

Processing Flow and Performance

Evaluation of Inner Receiver

In this chapter, we state the processing flow of inner receiver for received signal from reception to detection. We also explain the jobs in flow order of the inner receiver and why the order is. Next, we show the performance of the overall inner receiver by BER (bit error rate) after data detection versus SNR under the motionless and mobile conditions.

6.1 Processing Flow of Inner Receiver

Figure 6-1 shows the diagram of processing flow in inner receiver. In the following, we state the flow path and explain the functional blocks of a inner receiver as following:

Symbol synchronization and coarse carrier synchronization: after power turning on, the first job is to detect the symbol boundary and coarse fractional carrier offset if there is signal arrival. It is because that the estimations of carrier offset, clock offset, and channel may need post-FFT operation so that the symbol boundary must be

confirmed first. When estimating the symbol boundary with CP, the carrier offset is also detected and can be compensated before FFT which results in the reduction of ICI caused by the frequency shift. after that, the received symbols can be modulated with FFT.

Integer carrier synchronization: in the frequency domain, we first need to estimate the carrier frequency shift from the integer carrier offset; otherwise, symbols are all at unmatched subcarriers which lead to error of synchronization and detection.

Frame synchronization: with the symbol synchronization and coarse carrier synchronization, next tasks are clock synchronization and fine carrier synchronization which may need the help of scattered pilots. The scattered pilots are divided into four subsets and each subset is located at different carrier index. Therefore, before further synchronization, we need frame synchronization to find the corresponding subset of scattered pilots for each OFDM symbol. The method of frame synchronization use the property of duplication in location of scattered pilots for every four OFDM symbol, that is, correlate post-FFT symbols at the locations of each subset in lth OFDM symbol to those in (l-4)th OFDM symbol and the subset with max correlation is the correct one for lth OFDM symbol.

Clock and carrier synchronization: before tracking for carrier and clock offsets, coarse estimation of clock offset is performed by averaging the computing result of clock error found by the algorithm in chapter 5 to reduce the range of tracking. For carrier and clock tracking, we may select certain pilots with higher channel SNR so that the interference by channel noise is smaller and the tracking performance is better. Therefore, a coarse estimation for the magnitude of channel response may need.

Channel estimation and data detection: after completing the synchronization, we can accurately estimation the channel response, which contains actual channel and the terms caused by non-ideal synchronizations. By equalizing with single-tap FEQ

(Frequency-domain Equalizer), data can be detected out.
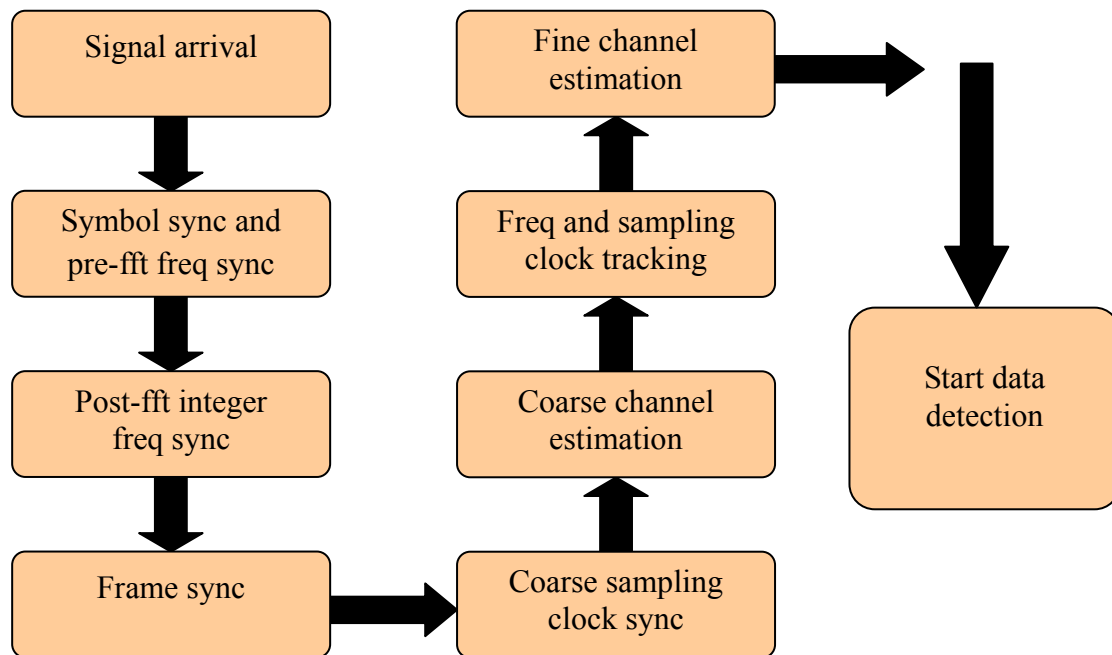
Figure 6-1 processing flow of inner receiver

6.2 Performance of Inner Receiver

● **Simulation parameters**

In this section, we display the results of our simulation for DVB-T inner receiver. The simulation settings of relative parameters are list in Table 6-1. For the parameters about clock and carrier synchronization, the settings are the same with those in chapter 4 and 5. We select double ADC sampling rate and show the results with two digital resampling schemes: cubic B-spline interpolator with 5-tap prefilter which has SER of 46 dB and 5th B-spline interpolator with 11-tap prefilter which has SER of 62 dB. In addition, a second order loop filter in our close loop for clock and carrier synchronization. Furthermore, we consider clock and carrier offsets simultaneously. With respect to the settings of channel estimation, because the variation in time

direction is usually slow, we select linear interpolation for time-direction channel interpolation. For freq-direction channel interpolation, we choose DFT-based interpolation for more accurate estimation.

system	DVB-T
transmission mode	2K
channel bandwidth	8MHz
CP mode	1/8
carrier frequency fc	500MHz
modulation	QPSK, 16QAM
channel model	HT channel model in COST207
mobile velocity	0, 100, 200, 300 km/hr
carrier frequency offset	100 ppm
sampling clock offset	100 ppm
A/D oversampling rate	2 (i.e. 18.28MHz)
digital resampler	cubic B-spline interpolator (5-tap prefilter) 5th B-spline interpolator (11-tap prefilter)
loop filter parameter $[K_0, K_1]$	[0.015,0.005], [0.004, 0.0016]
time-direction channel interpolation	linear interpolation
freq-direction channel interpolation	DFT-based interpolation

Table 6-1 simulation parameters for inner receiver

We show the performance of three schemes. The first is our proposed TD scheme which has clock and carrier tracking with the estimation in time domain (preceding FFT). Another is traditional FD scheme which synchronizes the clock and carrier frequency with the estimation in frequency domain (post FFT). The last is the ideal

scheme which assumes all synchronizations and channel estimation are done perfectly.

The three schemes are listed as following:

1. proposed TD : pre-FFT clock synchronization + pre-FFT carrier tracking

2. traditional FD : post-FFT clock synchronization + post-FFT carrier tracking

3. Ideal : perfect synchronization and channel estimation

The overall simulation model for inner receiver is shown in Figure 6-2.
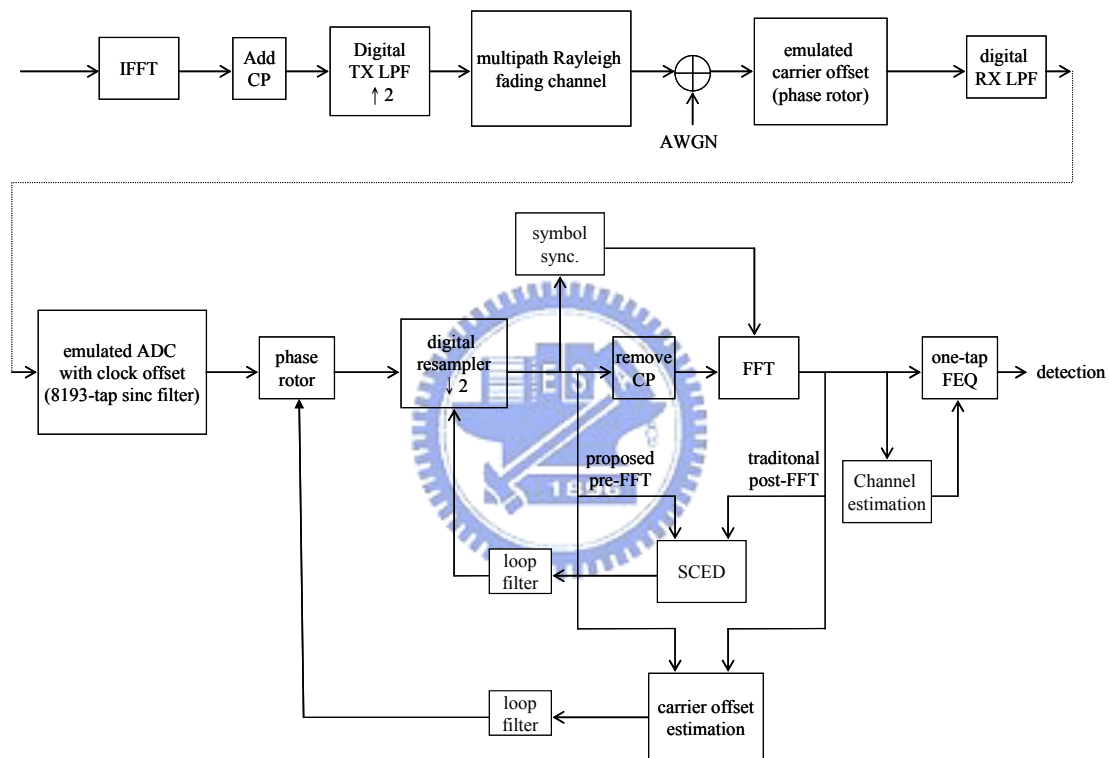
Figure 6-2 simulation model for inner receiver

● Simulation results

The simulation results with cubic B-spline interpolators are shown in Figure 6-3 for QPSK and 6-4 for 16 QAM. For the TD scheme, we have shown that the performance of synchronization for clock and carrier offsets is almost the same under conditions of various mobile velocities in chapter 4 and 5. The effect of different velocities is the variation rate of the channel. With larger mobile velocity, the channel

varies more rapidly which affects the accurate of channel estimation in time direction. For low SNR, the difference of BER at various mobile velocities is not apparent because the error of channel estimation is relatively small to channel noise. However, for high SNR, this effect will appear in BER as shown in Figure 6-3 (a) for QPSK and 6-4 (a) for 16 QAM.

For FD scheme, the performance is shown in Figure 6-3 (b) for QPSK and 6-4 (b) for 16 QAM. In addition to the effect of channel estimation, there is still the disturbance of residual clock and carrier offsets that are large at a large mobile velocity as shown in chapter 4 and 5. Therefore, the effect of mobile velocity is larger for FD scheme than TD scheme. From 6-3 (b) and 6-4 (b) we can see, the BER under motionless condition is very close to the ideal scheme. With a velocity of 100 km/hr, the decrease of performance is not unacceptable. Nevertheless, with velocities of 200 and 300 km/hr, the decrease of performance is significant due to the insufficient precision of carrier and clock synchronizations.

Figure 6-5 and 6-6 show the results with 5th order B-spline interpolators which has SER of 62 dB. From observation, the results are almost the same with those with cubic B-spline interpolators which has SER of 46 dB.
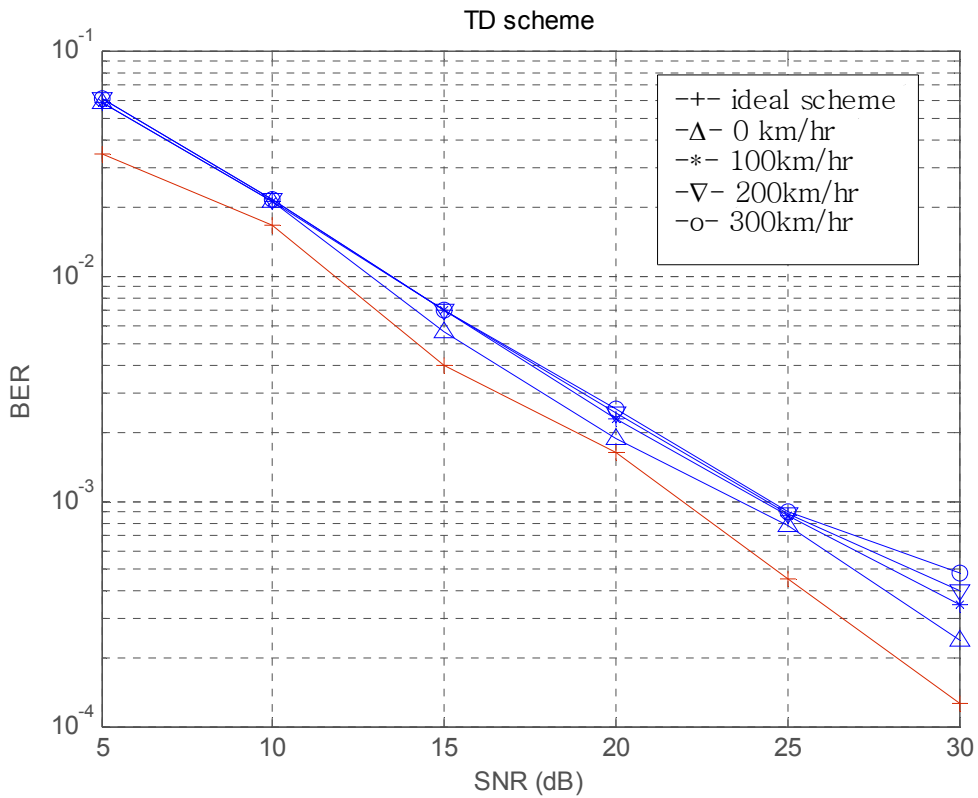
Figure 6-3 (a) BER of the TD-scheme inner receiver (cubic interpolator) for QPSK

Figure 6-3 (b) BER of the FD-scheme inner receiver (cubic interpolator) for QPSK

Figure 6-4 (a) BER of the TD-scheme inner receiver (cubic interpolator) for 16 QAM

Figure 6-4 (b) BER of the FD-scheme inner receiver (cubic interpolator) for 16QAM

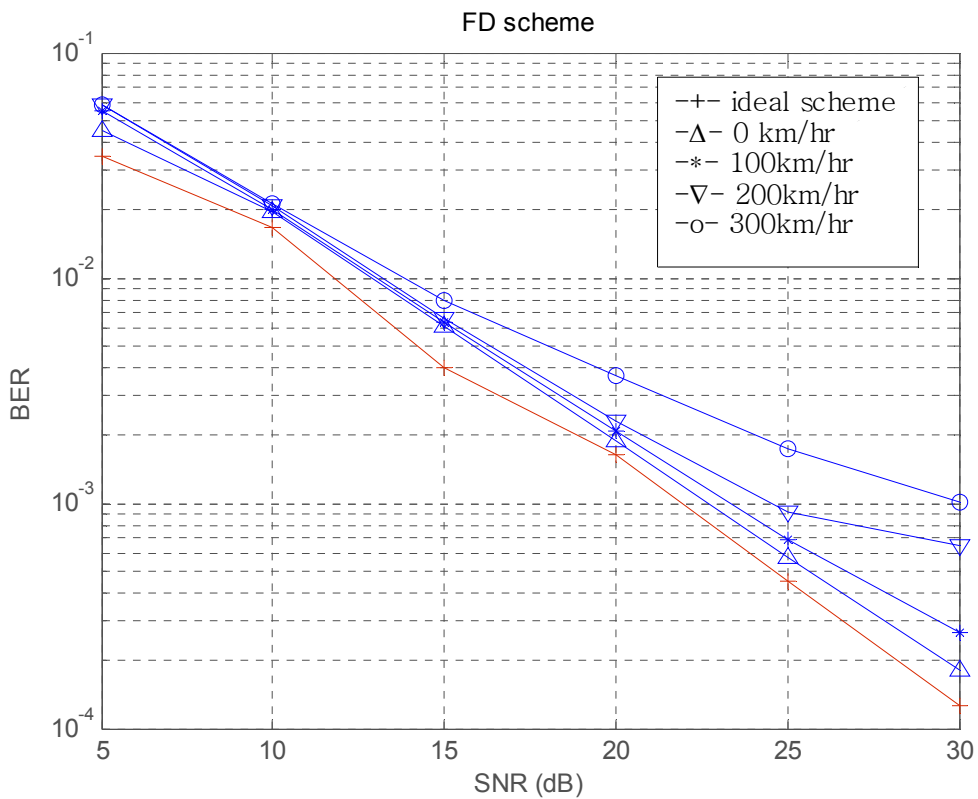Figure 6-5 (a) BER of the TD-scheme inner receiver (5th interpolator) for QPSK

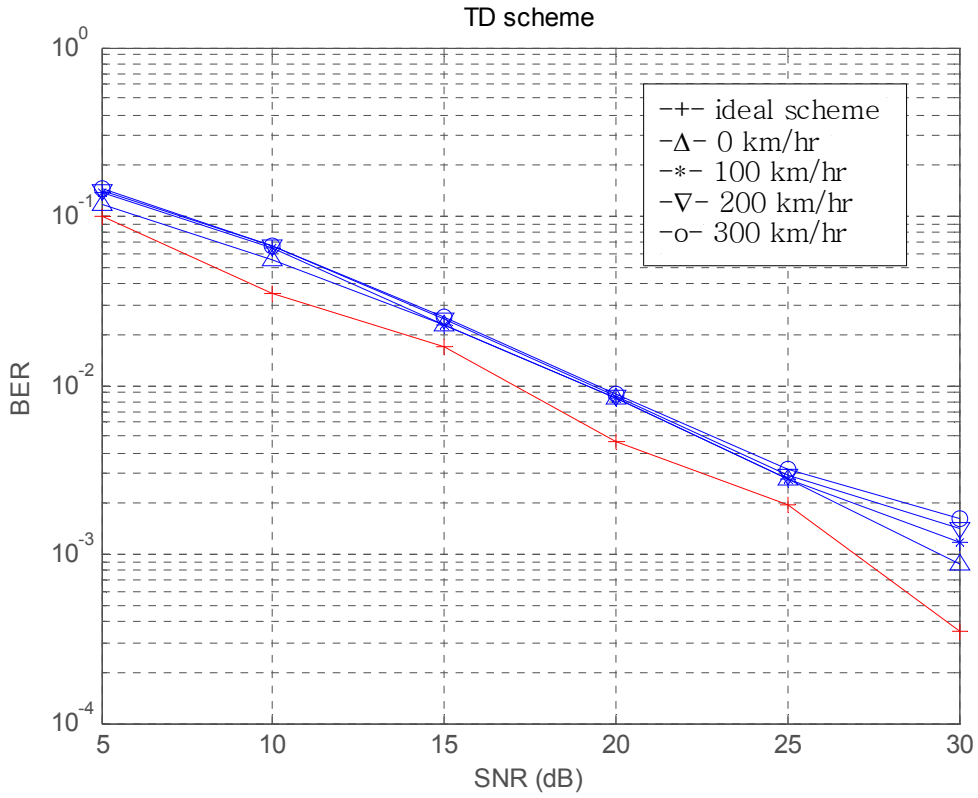Figure 6-5 (b) BER of the FD-scheme inner receiver (5th interpolator) for QPSK

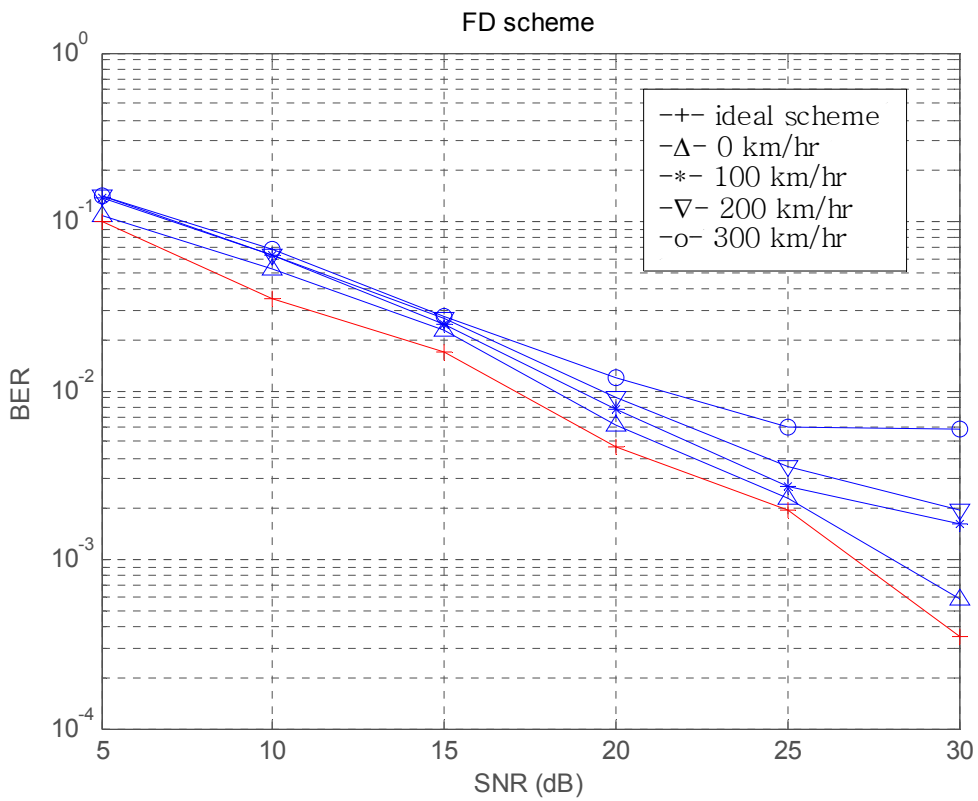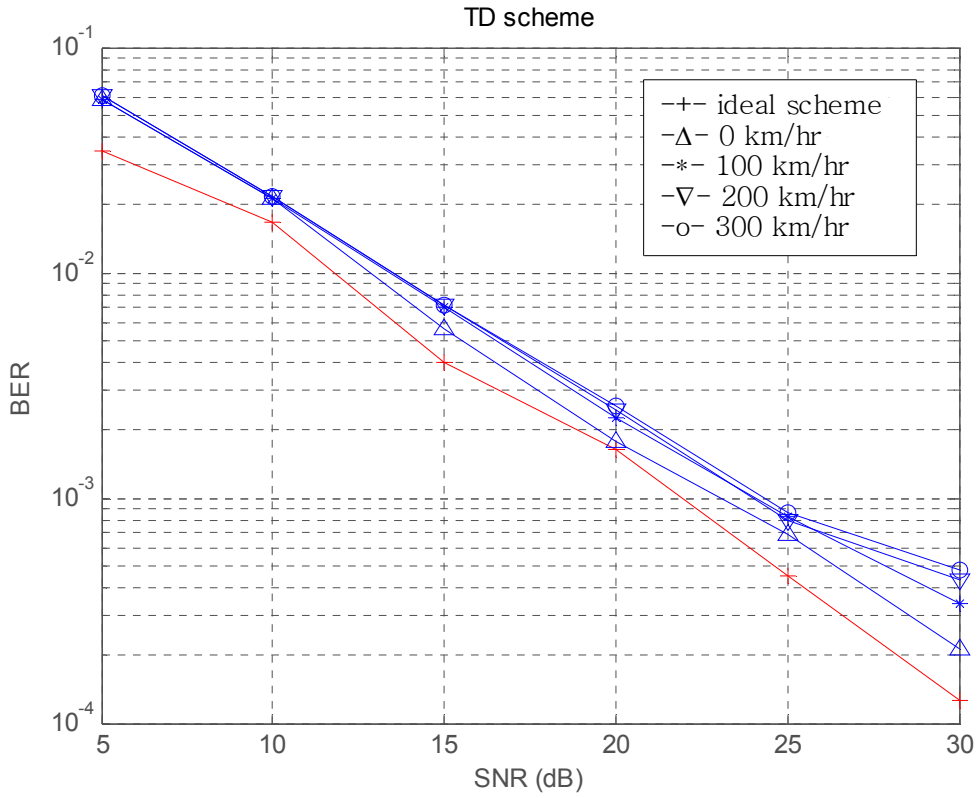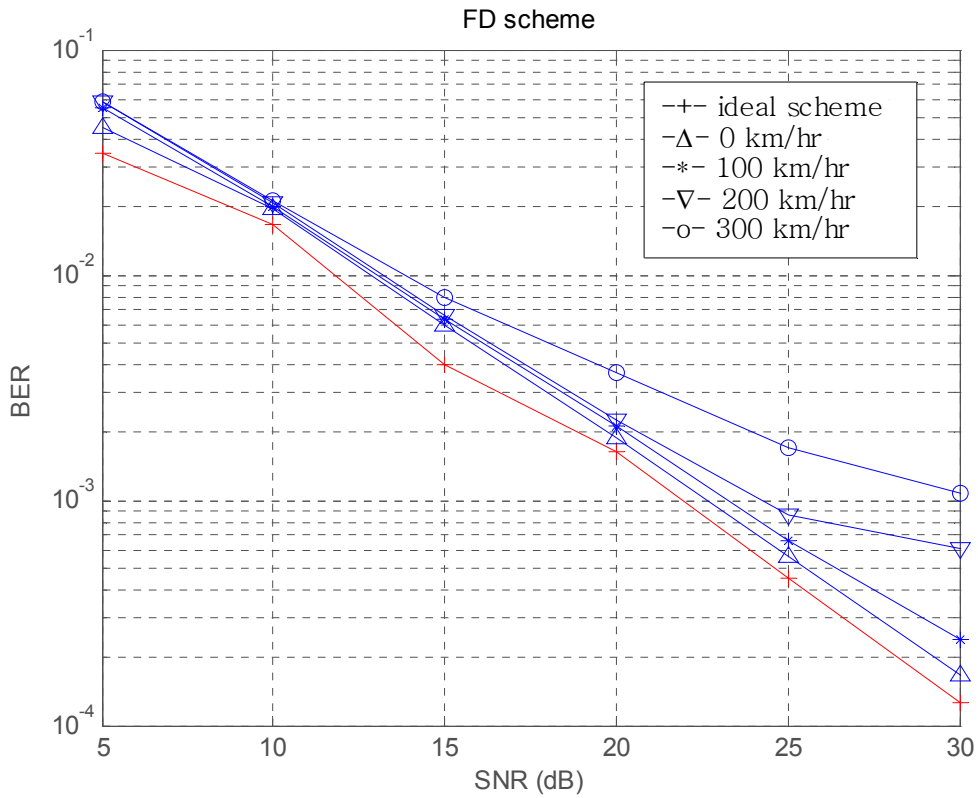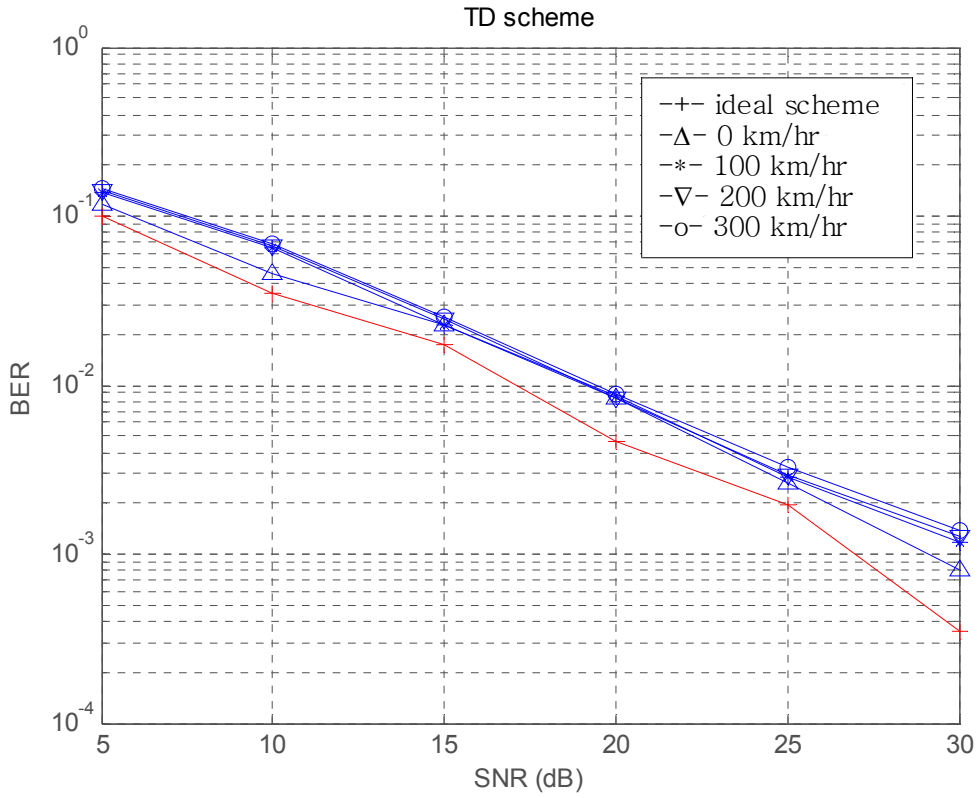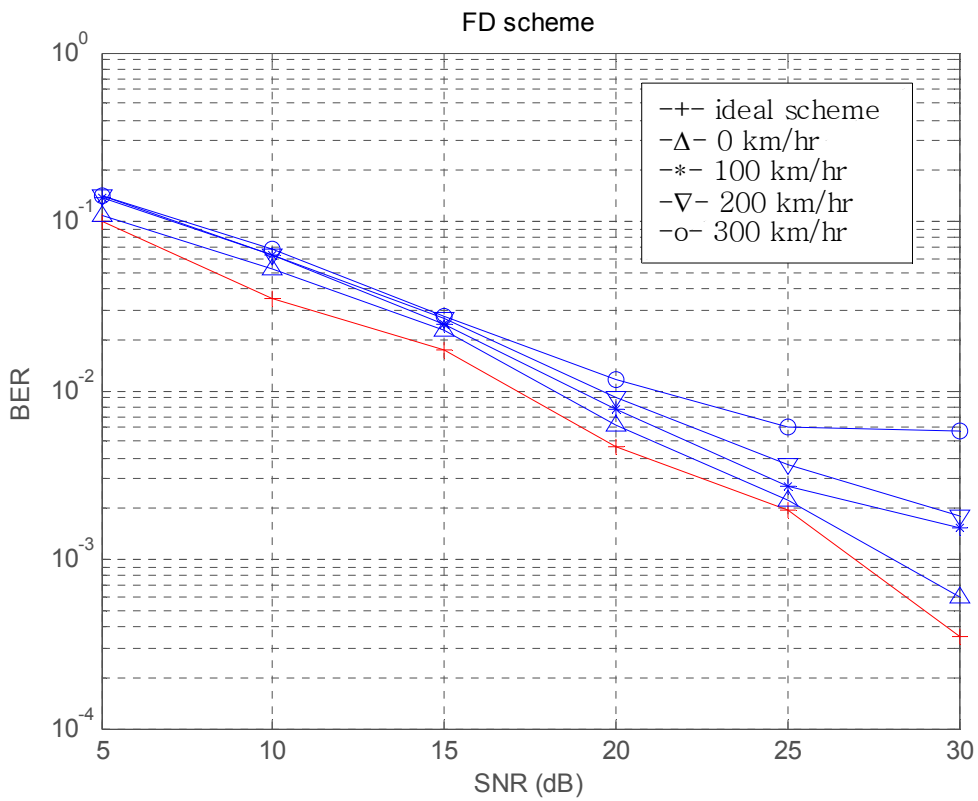Figure 6-6 (a) BER of the TD-scheme inner receiver (5th interpolator) for 16 QAM

Figure 6-6 (b) BER of the FD-scheme inner receiver (5th interpolator) for 16 QAM

Chapter 7
Conclusion and Future Work

DVB-T is the most countries adopting system for digital TV and is basically designed for terrestrial television which is supposed to be motionless. There are already many documents for a receiver in a static environment. However, with the increasing demand for mobile reception, a DVB-T receiver also needs to operate in a mobile environment. Thus, it is needed to design a receiver robust to the mobile effect.

In this thesis, we propose a receiver strategy that handles the synchronizations in time domain to prevent the interference by channel variation which cause system performance decrease significantly. With comparison between the traditional post-FFT and our proposed pre-FFT schemes for clock synchronizations, the simulation shows our proposed pre-FFT scheme has better performance in a mobile system. In addition, by using CP, it needs no additional reference data for our proposed pre-FFT clock synchronization. Finally, we state the processing flow of DVB-T inner receiver and we also show the BER versus SNR of the inner receiver. From simulation, we can see that the resulting performance of the proposed architecture in this thesis is more robust to the mobile channel.

In recent years, digital TV is more and more popular worldwide and many countries plan to substitute traditional TV with digital form overall in a few years,

such as Taiwan and North America in 2006, Japan in 2010, and China in 2015. Therefore, digital TV is very important to our future life. The contribution of this thesis is to propose an innovative synchronization algorithm that is robust to the mobile effect and need no additional reference data. Therefore, we can get a more efficient and better performance receiver for the demand of mobility in DVB-T system.

In this thesis, we present the architecture of a DVB-T inner receiver. For a digital receiver, the outer receiver is also considered. The outer receiver of DVB-T is composed of inner decoding (punctured convolutional code) and outer decoding (Reed-Solomon code). In future work, our goal is to complete the part of outer receiver and to combine it with inner one to make up the total architecture for a digital receiver of DVB-T.

Bibliography

[1] Salzberg, B. R., "Performance of an efficient parallel data transmission system," *IEEE Trans. Commun.*, Vol. COM-15, pp. 805-811, Dec. 1967.

[2] Weinstein, S. B., and P. M. Ebert, "Data Transmission by Frequency Division Multiplexing Using the Discrete Fourier Transform," *IEEE Trans. Commun.*, Vol. COM-19, pp. 628-634, Oct. 1971.

[3] A. Peled and A. Ruiz, "Frequency domain data transmission using reduced computational complexity algorithms," in *Proc. IEEE Int. Conf. Acoust., Speech, Signal Processing.*, pp. 964-967, Denver, CO, 1980.

[4] ETSI, "Radio broadcasting systems: Digital Audio Broadcasting to mobile, portable and fixed receivers," European Telecommunication Standard 300 401, 2nd ed., European Telecommunication Standard Institute, Valbonne, France, 1997.

[5] ETSI, "Digital Video Broadcasting: framing structure, channel coding, and modulation for digital terrestrial television," European Telecommunication Standard 300 744, European Telecommunication Standard Institute, August 1997.

[6] IEEE Std. 802.11a-1999, Part 11: Wireless LAN Medium Control (MAC) and Physical Layer (PHY) Specifications: High-speed Physical Layer in the 5GHz Band. LAN/MAN Standards Committee of the IEEE computer society, Sep. 16,

1999.

[7] IEEE Standard for Local and metropolitan area networks – Part 16: Air Interface for Fixed Broadband Wireless Access Systems – Amenament 2: Medium Access Control Modifications and Additional Physical Layer Specifications for 2-11 GHz, IEEE Std 802.16a-2003 (Amendment to IEEE Std 802.16-2001), pp. 0_1-292, 2003.

[8] P.H. Moose, "A technique for orthogonal frequency division multiplexing frequency offset correction," *IEEE Trans. Commun.*, vol. COM-42, pp. 2908-2914, October 1994.

[9] R. van Nee and R. Prasad, *OFDM for Wireless Multimedia Communications*, Artech House, 2000.

[10] T. S. Rappaport, *Wireless Communications Principles & Practice*, Prentice Hall, 1999.

[11] Jakes, C. Willian, *Microwave Mobile Communication*, New York: Willey, 1974.

[12] P. Dent, G. E. Bottomly, and T. Croft, "Jakes Fading Model Revisited," IEE, Electronics Letters, vol. 29, no. 13, pp.1162-1163, 23rd March 1993.

[13] AHMED, N., and RAO, K. R. : "Orthogonal transforms for digital signal processing" (Springer-Verlag, New York, 1975).

[14] COST 207 Management Committee, " COST 207 : Digital Land Mobile Radio Communications (Final Report), " Commission of the European Communities, 1989.

[15] T. Pollet, P. Spruyt, and M. Moeneclaey, "The BER Performance of OFDM Systems using Non-Synchronized Sampling, " *Proc. GLOBECOM'94*, San Francisco, CA, Dec. 27-29, 1994, pp. 253-57.

[16] Pollet Thierry, Peeters Miguel: Synchronization with DMT Modulation. IEEE Communication Magazine, April 1999, pp.80 - 86.

[17] M. Speth, S.A. Fechtel, G. Fock and H. Meyr, "Optimum Receiver Design for Wireless Broad-Band Systems Using OFDM — Part I," IEEE Trans. Comm., vol. 47, no. 11, pp. 1668-1677,Nov. 1999.

[18] M. Speth, S. Fechtel, G. Fock, and H. Meyr, "Optimum receiver design for OFDM-based broadband transmission-part II: A case study", IEEE Trans. Commun.Vol. 49, no. 4, pp. 571-578, Apr. 2001.

[19] Hou-Shin Chen and Yumin Lee, "Novel sampling clock offset estimation for DVB-T OFDM, " *IEEE VTC* ,2003 IEEE 58th, vol. 4, 6-9 Oct. 2003, pp. 2272 – 2276

[20] L. L. Scharf, *Statistical Signal Processing: Detection, Estimation, and Time Series Analysis*, Addison-Wesley, 1991.

[21] F.M. Gardner, "Interpolation in digital modems. I. Fundamentals", *IEEE Trans. on Comm.*, vol. 41 Issue 3, pp. 501 – 507, March 1993.

[22] H. Meyr, M. Moeneclaey, SA Fechtel, Digital Communication Receivers: Synchronization, Channel Estimation, and Signal Processing, John Wiley & Sons, 1998.

[23] C. W. Farrow, "A continuously variable digital delay element, " in *Proc. IEEE Int. Symp. Circuits & Syst., Espoo, Finland*, June 6-9, 1988, pp. 2641-2645.

[24] I. J. Schoenberg, "Contribution to the problem of approximation of equidistant data by analytic functions, " *Quart. Appl. Math.*, vol. 4, pp. 45-99, 112-141, 1946.

[25] I. J. Schoenberg, *Cardinal Spline Interpolation*. Philadelphia, PA: SIAM, 1973.

[26] M. Unser, A. Aldroubi and M. Eden, Fast B-Spline Transforms for Continuous Image Representation and Interpolation, IEEE Trans. PatternAnal. and Machine Intell., vol. 13, no. 3, pp. 277-285, 1991.

[27] M.Sandell, J.-J.van de Beek, and P. O.Bo¨rjesson, "Timing and frequency synchronization in OFDM systems using the cyclic prefix," *Proc. Int. Symp. Synchronization Essen*, Germany, pp. 16-19, Dec. 14–15, 1995.

[28] B. Yang, KB Letaief, RS Cheng & Z. Cao, Timing Recovery for OFDM Transmission, *IEEE Journal ON Selected. Araes in Communications*, vol.18, no.11, November 2000.

[29] F. Frescura, et al., "DSP based OFDM demodulator and equalizer for professional DVB-T receivers," *IEEE Trans. on Broadcasting*, vol. 45-3, pp. 323-332, Sep. 1999.

[30] M. Garcia, J. Paez-Borrallo, S. Zazo, "DFT-Based Channel Estimation in 2D-Pilot-Symbol-Aided OFDM Wireless Systems," *IEEE Vehicular Technology Conference*, 2001.

[31] M. Siala, G. Kawas Kaleh, "Equalization for orthogonal frequency division multiplexing system," *IEEE Vehicular Technology Conference*, 1993 IEEE 43rd, 18-20 May 1993 Page(s):649 - 652.

[32] B. Paillard, J. Soumagne, P. Mabilleau and S. Morisette, "Subband decomposition: An LMS-based algorithm to approximate the perfect reconstruction bank in the general case", IEEE Trans. Signal Process., Vol. 39, No. l, January 1991, pp. 233-238.